

A NEW APPROACH TO SHUTTERLESS OPERATION OF
MICROBOLOMETER BASED INFRARED CAMERAS

A THESIS SUBMITTED TO
THE GRADUATE SCHOOL OF NATURAL AND APPLIED SCIENCES
OF
MIDDLE EAST TECHNICAL UNIVERSITY

BY

SEMİH ÇAVDAR

IN PARTIAL FULFILLMENT OF THE REQUIREMENTS
FOR
THE DEGREE OF MASTER OF SCIENCE
IN
ELECTRICAL AND ELECTRONIC ENGINEERING

FEBRUARY 2021

Approval of the thesis:

**A NEW APPROACH TO SHUTTERLESS OPERATION OF
MICROBOLOMETER BASED INFRARED CAMERAS**

submitted by **SEMIH ÇAVDAR** in partial fulfillment of the requirements for the degree of **Master of Science in Electrical and Electronic Engineering, Middle East Technical University** by,

Prof. Dr. Halil Kalıpçılar
Dean, Graduate School of **Natural and Applied Sciences** _____

Prof. Dr. İlkay Ulusoy
Head of the Department, **Electrical and Electronics Eng.** _____

Prof. Dr. Tayfun Akın
Supervisor, **Electrical and Electronics Eng. Dept., METU** _____

Examining Committee Members:

Prof. Dr. Haluk Külah
Electrical and Electronics Eng. Dept., METU _____

Prof. Dr. Tayfun Akın
Electrical and Electronics Eng. Dept., METU _____

Prof. Dr. Gözde Bozdağı Akar
Electrical and Electronics Eng. Dept., METU _____

Assoc. Prof. Dr. Kıvanç Azgın
Mechanical Eng. Dept., METU _____

Assoc. Prof. Dr. Dinçer Gökcen
Electrical and Electronics Eng. Dept., Hacettepe University _____

Date: 03.02.2021

I hereby declare that all information in this document has been obtained and presented in accordance with academic rules and ethical conduct. I also declare that, as required by these rules and conduct, I have fully cited and referenced all material and results that are not original to this work.

Name, Last name : Semih Çavdar

Signature :

ABSTRACT

A NEW APPROACH TO SHUTTERLESS OPERATION OF MICROBOLOMETER BASED INFRARED CAMERAS

Çavdar, Semih

Master of Science, Electrical and Electronic Engineering

Supervisor: Prof. Dr. Tayfun Akın

February 2021, 127 pages

This thesis presents an algorithm for the shutterless operation of microbolometer based infrared imaging systems. The active material of the microbolometer used in the thesis is vanadium oxide and it is produced in METU MEMS Center. The array size of the microbolometer is 480x640 and pixel pitch is 17 μm . The microbolometer has a CTIA type readout circuit which consists of detector and reference resistance.

Voltage values are optimized at steady-state considering interactions between pixels in the focal plane array (FPA). An algorithm to find these interactions and optimum voltage values is proposed. Output distributions of the pixels obtained with the method are analyzed and residual nonuniformity (RNU) values are compared to standard methods which are sweep and binary search. These methods and the proposed algorithm are applied to five different samples. Improvement in the operability is observed and RNU values are decreased generally half of the value found with standard methods.

A method is proposed to find optimum voltages for each 1 $^{\circ}\text{C}$ by using at least two calibration points although TCR of vanadium oxide material has nonlinear

temperature characteristics. 2-point correction, which contains gain and offset coefficients, is used as the software-based correction to improve the uniformity. Gain and offset coefficients are modeled for temperature and a way to estimate these coefficients is presented. Temperature drift, which is used to explain alterations in pixel outputs against small temperature variations, is modeled for 1 °C interval and the temperature drift compensation method is also proposed.

The proposed shutterless algorithm is applied to three different microbolometers for the temperature range between 0 °C to 50 °C. RNU values are kept below 1% with the algorithm and decreased down to around 0.5% at low temperatures. The PSNR values calculated from infrared images are about 50 dB. Temperature drift compensation provides good stability at the pixel outputs and maximum shift at the output is observed around 6%. The proposed algorithm decreases the number of required calibration temperatures down to 12 from 51 which means a lower calibration time of around 76%. It requires lower memory space about 84% of the standard method by decreasing the array number from 102 to 16. The results show that the proposed algorithm can be used in the shutterless application for microbolometers.

Keywords: Nonuniformity Compensation, Voltage Optimization for Microbolometers, TECless Operation of Microbolometers, Shutterless Operation of Microbolometers

ÖZ

MİKROBOLOMETRE TABANLI KIZILÖTESİ KAMERALARIN ÖRTÜCUSÜZ ÇALIŞMASINA YENİ BİR YAKLAŞIM

Çavdar, Semih
Yüksek Lisans, Elektrik ve Elektronik Mühendisliği
Tez Yöneticisi: Prof. Dr. Tayfun Akın

Şubat 2021, 127 sayfa

Bu tezde mikrobolometre tabanlı kızılötesi görüntüleme sistemlerinin örtücsüz (*Ing. “Shutterless”*) operasyonu için algoritma sunulmaktadır. Bu tezde kullanılan mikrobolometrenin aktif malzemesi vanadyum oksittir ve ODTÜ MEMS Merkezi’nde üretilmiştir. Mikrobolometre matris büyütüğü 480x640 ve piksel büyütüğü 17 μm ’dir. Bu mikrobolometre detektör ve referans direncinde oluşan CTIA tipinde okuma devresine sahiptir.

Gerilim değerleri denge durumunda odak düzlem matrisindeki piksellerin birbirleriyle olan etkileşimleri düşünülerek optimize edilmiştir. Bu etkileşimler ve optimum gerilim değerlerini bulmak için bir algoritma önerilmiştir. Bu metotla elde edilen piksellerin çıktı dağılımları analiz edilmiştir ve düzensizlik (RNU) değerleri tarama ve ikili arama olan standart metotlar ile karşılaştırılmıştır. Bu metotlar ve önerilen algoritma 5 farklı örneğe uygulanmıştır. Çalışabilirlikte iyileşme gözlenir ve RNU değerleri genellikle standart yöntemlerle bulunan değerin yarısı kadar azaltılır.

Vanadyum oksit malzemenin TCR’si doğrusal olmayan sıcaklık özelliklerine sahip olmasına rağmen, en az iki kalibrasyon noktası kullanarak her 1 °C için optimum

gerilimleri bulmak amacıyla bir yöntem önerilmiştir. Kazanç ve ofset katsayılarını içeren 2 noktalı düzeltme tekdüzelik geliştirmek için yazılım tabanlı düzeltme olarak kullanılmıştır. Kazanç ve ofset katsayıları sıcaklığa göre modellenmiştir ve bu katsayıları tahmin etmenin bir yolu sunulmuştur. Küçük sıcaklık değişimlerine karşı piksel çıktılarındaki değişiklikleri açıklamak için kullanılan sıcaklık kayması $1\text{ }^{\circ}\text{C}$ aralık için modellenmiştir ve sıcaklık kayması telfisi yöntemi de önerilmiştir.

Önerilen örtücsüz algoritma $0\text{ }^{\circ}\text{C}$ ile $50\text{ }^{\circ}\text{C}$ arasındaki sıcaklık aralığı için üç farklı mikrobolometreye uygulanmıştır. Algoritma ile RNU değerleri $\%1$ 'in altında tutulmuştur ve düşük sıcaklıklarda yaklaşık $\%0,5$ 'e kadar düşürülmüştür. Kızılıtesi görüntülerden hesaplanan PSNR değerleri yaklaşık 50 dB 'dir. Sıcaklık kayması telfisi piksel çıkışlarında iyi stabilité sağlamıştır ve çıkışta maksimum kayma $\%6$ civarında gözlemlenmiştir. Önerilen algoritma gereklî kalibrasyon sıcaklıklarının sayısını 51 'den 12 'e düşürür, bu da $\%76$ civarında daha düşük kalibrasyon süresi anlamına gelir. Matris sayısını 102 'den 16 'ya düşürerek standart yöntemin yaklaşık $\%84$ 'ü kadar daha düşük bellek alanı gerektirir. Sonuçlar, önerilen algoritmanın mikrobolometreler için örtücsüz uygulamada kullanılabileceğini göstermektedir.

Anahtar Kelimeler: Düzensizlik Telfisi, Mikrobolometreler için Voltaj Optimizasyonu, Mikrobolometrelerin TEC'siz Çalışması, Mikrobolometrelerin Örtücsüz Çalışması

To my family

ACKNOWLEDGEMENTS

I would like to express my gratitude to my supervisor Prof. Dr. Tayfun Akın for his guidance, advice, criticism, encouragement, and insight throughout the research.

I also would like to thank Dr. Selçuk Özer for sharing his extensive knowledge and experience at every stage of the thesis work.

I would like to express my appreciation to my colleagues, Kübra Ceren Hancı and Utku Çekmez for motivating me throughout the work and technical supports during the experiments performed in the thesis.

I would like to thank Çiğdem Doğru, Hakan Sürel, and Baran Utku Tekin for the process of the microbolometers used in the thesis. Additionally, I would like to present my thanks to Bahar Atik for sharing knowledge about the characteristics of the active material used in the microbolometers.

Last but not least, I would like to give my special thanks to my family for their support and encouragement throughout the thesis work.

TABLE OF CONTENTS

ABSTRACT	v
ÖZ	vii
ACKNOWLEDGEMENTS	x
TABLE OF CONTENTS.....	xi
LIST OF TABLES	xiii
LIST OF FIGURES	xiv
CHAPTERS	
1 INTRODUCTION	1
1.1 Microbolometer.....	2
1.1.1 Resistive Type Microbolometers	3
1.2 Main Performance Parameters of Microbolometers	4
1.2.1 Noise.....	5
1.2.2 Responsivity	7
1.2.3 Noise Equivalent Temperature Difference (NETD)	9
1.3 Readout Architectures for Microbolometers.....	10
1.3.1 Preamplifier Circuit Types for Microbolometers.....	10
1.3.2 Readout Operation of Pixel Outputs	15
1.4 Control Parameters for CTIA Type ROICs	18
1.5 Resistance Nonuniformity	20
1.6 Effect of Temperature on Calibration Parameters of Microbolometers	27
1.7 Research Objectives and Thesis Organization.....	33
2 UNIFORMITY OPTIMIZATION AT STEADY STATE CASE	35

2.1	Standard Optimization Algorithms for Bias DACs	38
2.1.1	Sweep Method	40
2.1.2	Binary Search Method	42
2.2	Pixel Interactions	44
2.2.1	Inside Row Interaction.....	46
2.2.2	Row-to-Row Interaction	49
2.3	Interacted NUC Voltage Algorithm	52
2.4	Software-Based Correction	62
3	COMPENSATION OF TEMPERATURE EFFECTS	65
3.1	Bias Voltage Estimation	67
3.2	Software-Based Correction Parameters Estimation	78
3.2.1	Gain Estimation	79
3.2.2	Offset Estimation	80
3.2.3	Temperature Drift Compensation	85
3.3	Results and Discussion	89
4	CONCLUSION AND FUTURE WORK.....	109
	REFERENCES	113
	APPENDICES	
A.	Thermal Images for Sample 6	121
B.	Thermal Images for Sample 7	122
C.	Thermal Images for Sample 8	125

LIST OF TABLES

TABLES

Table 2-1: Comparison of the sweep and binary search methods for the microbolometer in terms of RNU and saturated pixel ratio.....	44
Table 2-2: RNU values of the microbolometer for the number of the proposed algorithm repeated.	59
Table 2-3: Comparison of RNU values and saturated pixel ratios for five different microbolometers which are calibrated with the conventional methods and the proposed algorithm when the temperature of the microbolometer is 20 °C.	61
Table 3-1: Microbolometer temperature points when the data are collected.....	95
Table 3-2: RNU values for <i>Sample 6</i> , <i>Sample 7</i> , and <i>Sample 8</i> obtained with the proposed algorithm.	98
Table 3-3: PSNR value comparison of different algorithms.	106

LIST OF FIGURES

FIGURES

Figure 1-1: Simple demonstration of microbolometers.....	3
Figure 1-2: Simple demonstration of resistive type microbolometer pixel structure.	3
Figure 1-3: Thermal circuit representation of the microbolometer structure. [12] ...	7
Figure 1-4: Simple schematic of bolometer current direct injection type of preamplifier circuit.	11
Figure 1-5: Simple schematic of Wheatstone bridge differential amplifier type of preamplifier circuit.	12
Figure 1-6: Simple schematic of the capacitive trans-impedance amplifier type preamplifier circuit.	14
Figure 1-7: Demonstration of the top-level block diagram for microbolometer ROIC.....	15
Figure 1-8: Schematic demonstration of integrator circuit used in microbolometer ROICs.....	17
Figure 1-9: Effect of integration time on noise equivalent difference of temperature (NEDT) [27].	18
Figure 1-10: Effect of pixel bias on noise equivalent temperature difference (NETD) [29].	20
Figure 1-11: Detector resistance distribution of vanadium oxide microbolometer array (640x480) produced in METU MEMS Center. The pixel pitch is 17 μm	21
Figure 1-12: Reference resistance temperature change to the number of reference resistance used during imaging. The reference resistances have almost the same thermal conductance which is 20×10^{-7} nW/K [30].....	22
Figure 1-13: (a) Output of different pixels for infrared power, (b) output curves after 1-point correction is applied, and (c) output curves after 2-point correction is applied [39].....	26
Figure 1-14: Groups of compensation methods for output change due to temperature variations.	28

Figure 2-1: Pixel readout circuit of the microbolometer which is used in the thesis.	35
Figure 2-2: Measurement setup for microbolometers configurated in METU MEMS Center	36
Figure 2-3: Effect of the integration time on output nonuniformity and NETD.....	37
Figure 2-4: Detector and reference resistance distributions of the microbolometer at 20 °C produced in METU MEMS Center.....	38
Figure 2-5: Output histogram of the microbolometer at 20 °C produced in METU MEMS Center before calibration of the second stage of DACs for detector resistances	39
Figure 2-6: The algorithm of sweep method for a pixel in the FPA when n bit DAC is used to calibration.	40
Figure 2-7: Selected pixel outputs for the microbolometer during calibration of the second stage of DACs for detector resistances with the sweep method.	41
Figure 2-8: Output histogram of the microbolometer at 20 °C when the bias values are found with the sweep method.	41
Figure 2-9: The algorithm of the binary method for a pixel in the FPA when n bit DAC is used for calibration.	42
Figure 2-10: Selected pixel outputs for the microbolometer during calibration of the second stage of DACs for detector resistances with the binary search method.....	43
Figure 2-11: Output histogram of the microbolometer at 20 °C when the bias values are found with the binary search method.	43
Figure 2-12: Outputs of selected pixels obtained with sweep method and the case when all pixels are biased with calculated value for the pixel by using the sweep method for the microbolometer.	44
Figure 2-13: (a) Grayscale image for the differences between two different cavity blackbody temperatures and (b) detailed 3D demonstration for the region of interest.....	45
Figure 2-14: Pixel output differences of the selected row for original sweep method and manipulated case.	47

Figure 2-15: Pixel output differences of the selected row for the original case and manipulated cases which have a different number of manipulated pixels.	48
Figure 2-16: Output differences of the pixels which have constant DAC value for the number of manipulated pixels in the row.	48
Figure 2-17: Colored image map of output differences between the manipulated and original case in terms of ADU.	49
Figure 2-18: Mean values of output change for the next rows of the manipulated row in terms of ADU.	50
Figure 2-19: Change in the pixel outputs of row 240 when the pixels from row 241 to row 480 are saturated intentionally.	51
Figure 2-20: Linear regression for inside row interactions of the microbolometer.	52
Figure 2-21: Exponential fit for row-to-row interactions of the microbolometer.	53
Figure 2-22: Linear fit for output of a pixel for the input of the DAC during sweep method for the microbolometer.	54
Figure 2-23: Flowchart of the proposed algorithm for NUC voltages of the microbolometer.....	55
Figure 2-24: Output histogram comparison for the microbolometer obtained with conventional methods and the proposed algorithm.	58
Figure 2-25: Output histogram of the microbolometer for the number of the proposed algorithm repeated.	59
Figure 2-26: Mean of the output distribution for the microbolometer against the temperature of the blackbody.	62
Figure 2-27: Output nonuniformity of the microbolometer in selected scene dynamic range (between 10 °C and 70 °C) after 2-point correction is applied by using different two calibration points.....	63
Figure 3-1: TCR characteristics of the vanadium oxide type microbolometer between the temperatures from 20 °C to 30 °C.....	70
Figure 3-2: Assumed and real TCR characteristics of the vanadium oxide type microbolometer between the temperatures from 20 °C to 30 °C.	70

Figure 3-3: NUC values of a pixel from vanadium oxide type microbolometer for temperature.	72
Figure 3-4: Fitted and measured mean NUC values for the vanadium oxide type microbolometer for temperature.	73
Figure 3-5: Temperature coefficients of NUC voltages for the vanadium oxide type microbolometer for each 10 °C interval from 10 °C to 48 °C.	74
Figure 3-6: Fitted and measured mean NUC values by including global reference bias manipulations for the vanadium oxide type microbolometer for temperature.	76
Figure 3-7: Temperature coefficients of NUC voltages for the vanadium oxide type microbolometer from 10 °C to 48 °C when the GRB is kept constant and adjusted for each temperature orderly.	77
Figure 3-8: RMS errors of the estimation of NUC voltages of the vanadium oxide type microbolometer for the best and worst case.	77
Figure 3-9: Measurement setup for microbolometers to collect uniform infrared images from the blackbody configurated in METU MEMS Center.	78
Figure 3-10: Linear regression of gain values for some pixels of the vanadium oxide type microbolometer. Each color indicates the different pixels in the FPA.	80
Figure 3-11: Offset values for some pixels of the vanadium oxide type microbolometer for temperature.	81
Figure 3-12: Error histograms in offset estimation to show the effect of rounding error compensation (REC) for the vanadium oxide type microbolometer.	82
Figure 3-13: Pixel offset observation against temperature when the rounding error is 0 for the pixel.	83
Figure 3-14: Error histograms in offset estimation to show the effect of rounding error compensation and linear regression for the vanadium oxide type microbolometer.	84
Figure 3-15: Real and estimated offset values for some pixels of the vanadium oxide type microbolometer for temperature.	84
Figure 3-16: Gain coefficients of some pixels in the vanadium oxide type microbolometer for 1 °C temperature interval.	85

Figure 3-17: Gain coefficients of some pixels in the vanadium oxide type microbolometer for 1 °C temperature interval.	87
Figure 3-18: Measured and fitted temperature drift slopes for the microbolometer.	89
Figure 3-19: Output histograms for <i>Sample 6</i> , <i>Sample 7</i> , and <i>Sample 8</i> after NUC voltages are found with sweep and interacted algorithms, respectively.	90
Figure 3-20: RNU values of output distribution at each temperature point after NUC voltages are found with the sweep method, interacted method, and NUC voltages estimation for <i>Sample 6</i>	90
Figure 3-21: RNU values of output distribution at each temperature point after NUC voltages are found with the sweep method, interacted method, and NUC voltages estimation for <i>Sample 7</i>	91
Figure 3-22: RNU values of output distribution at each temperature point after NUC voltages are found with the sweep method, interacted method, and NUC voltages estimation for <i>Sample 8</i>	91
Figure 3-23: Mean values of output distributions for <i>Sample 6</i> , <i>Sample 7</i> , and <i>Sample 8</i> when NUC voltages are found with the proposed estimation method. ...	92
Figure 3-24: Saturated pixel ratios at each temperature point after NUC voltages are found with the sweep method, interacted method, and NUC voltages estimation method for <i>Sample 6</i>	93
Figure 3-25: Saturated pixel ratios at each temperature point after NUC voltages are found with the sweep method, interacted method, and NUC voltages estimation method for <i>Sample 7</i>	93
Figure 3-26: Saturated pixel ratios at each temperature point after NUC voltages are found with the sweep method, interacted method, and NUC voltages estimation method for <i>Sample 8</i>	94
Figure 3-27: RNU values for temperature when 3 and 6 temperature points are used to linear regression for <i>Sample 6</i>	95
Figure 3-28: RNU values for temperature when 6 temperature points are used to linear regression for <i>Sample 6</i>	96

Figure 3-29: RNU values for temperature when 6 temperature points are used to linear regression for <i>Sample 7</i>	97
Figure 3-30: RNU values for temperature when 6 temperature points are used to linear regression for <i>Sample 8</i>	97
Figure 3-31: Thermal images obtained from <i>Sample 6</i> , <i>Sample 7</i> , and <i>Sample 8</i> with real and estimated 2-point correction at 5 °C.	99
Figure 3-32: (a) Mean (ADU) and (b) RNU (%) values of <i>Sample 6</i> after 2-point correction parameters are found with the temperature drift compensation algorithm.	100
Figure 3-33: (a) Mean (ADU) and (b) RNU (%) values of <i>Sample 7</i> after 2-point correction parameters are found with the temperature drift compensation algorithm.	101
Figure 3-34: (a) Mean (ADU) and (b) RNU (%) values of <i>Sample 8</i> after 2-point correction parameters are found with the temperature drift compensation algorithm.	102
Figure 3-35: Thermal images obtained from <i>Sample 8</i> at 15.0 °C, 15.3 °C, 15.6 °C, and 15.9 °C with real and estimated 2-point correction parameters.	104
Figure 3-36: Comparison of proposed algorithms in the study [49] and the thesis.	105
Figure 3-37: PSNR values of <i>Sample 7</i> and <i>Sample 8</i> for temperature.	106

CHAPTER 1

INTRODUCTION

Infrared imaging depends on the observation of the electromagnetic waves, between 0.7 μm and 1000 μm, emitted from the object that has a temperature above 0 K where the human eye cannot detect. The data taken from the objects enable the detection of them, in other words, infrared imaging systems convert the infrared radiation into observable changes. Thermal imaging systems are demanded from several areas for both military [1] and civilian [2] applications.

Infrared detectors can be divided into two categories: photon detectors and thermal detectors. Photon detectors use the principle of interaction between infrared radiation and the electron inside the material. The interaction provides the construction of electron-hole pairs and an applied electric field into the system collects these pairs. Electronic circuits are used to integrate the produced current over the detector by these pairs. The working principle of the thermal detectors is different than the photon detectors. For the thermal detectors, infrared radiation increases the temperature of the material and this causes a change in the properties of the active material. The change is converted into meaningful signals with the help of electronic circuits. Thermal detectors can work properly at room temperature and therefore they are also called uncooled infrared detectors.

There are different types of thermal detectors such as pyroelectric detectors, thermocouples, and microbolometers. However, microbolometers are the most preferred ones since they have important advantages like higher responsivity. Moreover, infrared modulation is not required as pyroelectric detectors and they can be fabricated in small size, unlike thermocouples. A rise in demand for high-quality microbolometers requires producing large array size microbolometers with smaller

pixel size [3] and higher responsivity while keeping them low cost compared to photon detectors. The requirements increase the importance of the capability of the readout integrated circuits (ROIC) and optimization of ROIC control parameters. Furthermore, an increase in the array size of the microbolometers causes higher nonuniformity between the pixels in the focal plane array (FPA) and the calibration procedure of the microbolometers in the operational temperature range becomes a challenging issue.

The main goal of the thesis is to develop a shutterless algorithm for the high performance of microbolometers. The rest of the chapter gives detailed information about microbolometers. Section 1.1 explains the structure and operation principle of the microbolometers. Section 1.2 introduces the electronic circuits used for microbolometers. Section 1.3 gives information about the performance parameters of microbolometers. Section 1.4 explains the control parameters related to ROIC. Section 1.5 gives further information about nonuniformity between resistances of the pixels. Section 1.6 summarized the effect of temperature on microbolometers. Finally, Section 1.7 gives the research objectives and thesis organization.

1.1 Microbolometer

Microbolometers are one type of thermal detectors and they are used widely in different applications such as medicine, military, and security. They can be produced with the micro-fabrication process. Moreover, they are also compatible with CMOS technology.

Microbolometers operate with the principle which is the conversion of incoming infrared radiation into the temperature change in the active material as shown in Figure 1-1. Increase in the temperature causes changes in the property of active material and this enables to observe infrared radiation.

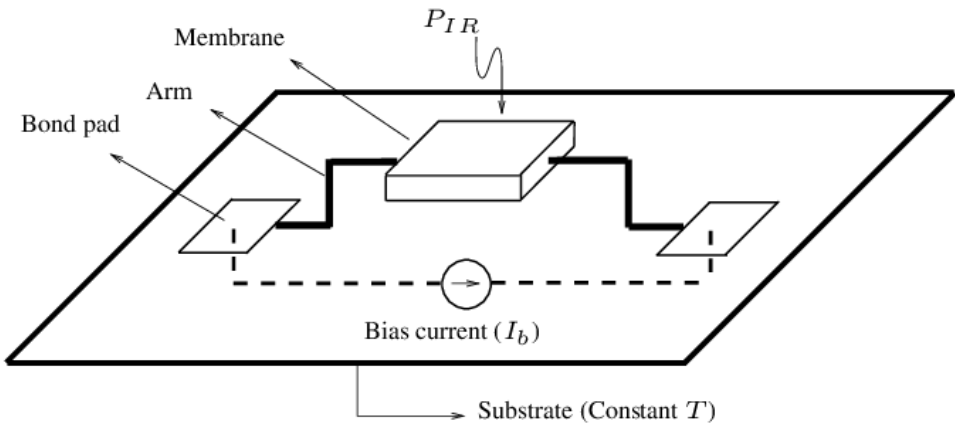


Figure 1-1: Simple demonstration of microbolometers.

Microbolometers can be divided into two categories: diode type and resistive type microbolometers. In the diode type microbolometers, the diode current alters with the temperature of the active material. Resistive type microbolometers use resistance to change in the active material due to temperature rise.

1.1.1 Resistive Type Microbolometers

Resistive microbolometers convert infrared radiation into an electrical signal with the help of a change in the resistance of active material concerning temperature. They have suspended bridges produced by micro-fabrication as seen in Figure 1-2.

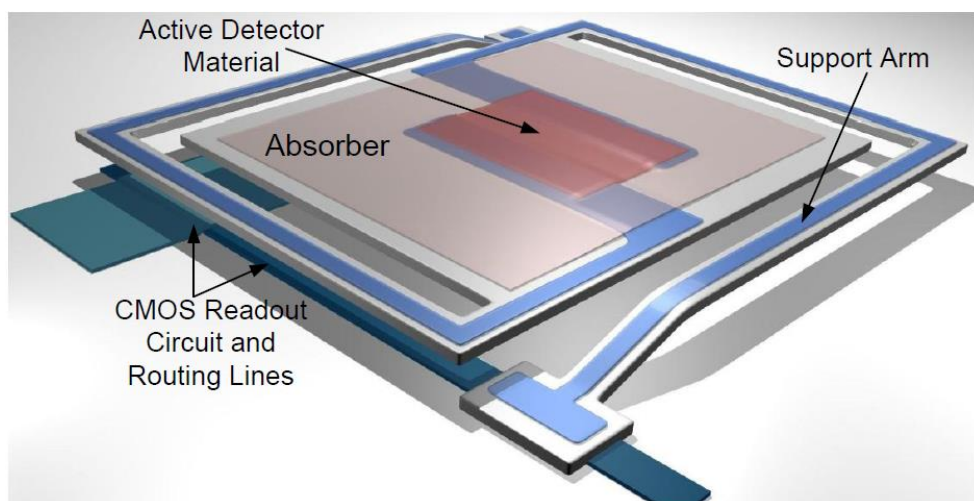


Figure 1-2: Simple demonstration of resistive type microbolometer pixel structure.

It is beneficial to increase the temperature rise in the resistance so that change in the resistance increases. For this reason, active detector material is deposited on top of the bridge. The material is highly sensitive to infrared radiation such as vanadium oxide (VO_x) [4], amorphous silicon a-Si [5], and silicon germanium oxide (Si-Ge-O) [6]. Since the incoming power is determined with the infrared radiation, the heat flown to the readout circuit causes loss in the resistance change of the active material. For this reason, the microbolometer structure should prevent the heat flow and it requires the suspended structure. Moreover, the support arms should have low thermal conductance to minimize heat loss. Another point is to absorb incoming infrared energy as much as possible. Therefore, the reflector layer is used in the microbolometer structure to increase the ratio of absorbed energy to incoming infrared energy. It is needed to convert resistance change to electrical signals with the help of the ROIC. This requires the electrical lines on the support arms to connect ROIC to the resistance of the active material.

1.2 Main Performance Parameters of Microbolometers

Performance of the microbolometers depends on the quality of the process, optical and geometrical structure of the microbolometer, and working conditions such as detector bias. The microbolometers are processed in different array sizes like 160x120, 384x288, 640x480, 1024x768, and their derivatives. Large array sizes of microbolometers cause complex structures; therefore, they have several performance parameters at the material level which depends on only the process of the microbolometers or system level. Main performance parameters that are used widely to compare performances of microbolometers are divided into three groups: noise, responsivity, and NETD.

1.2.1 Noise

Resistive type microbolometer structures composed of resistances processed by MEMS technology and circuits constructed by the silicon CMOS production. Both of these parts in the structure contribute to the noise level of the microbolometers. The noise in the microbolometers causes deviations in the infrared images and errors in the temperature of the target. For this reason, noise is one of the performance parameters for microbolometers.

Noise due to electronic circuit decreases with developments in the silicon CMOS technology. The noise level of the ROIC structures is the order of $\mu\text{V}/\sqrt{\text{Hz}}$ for large size microbolometers arrays like 384x288 and 640x480 [7] [8] [9] [10] [11].

Noise contribution of the detectors to the microbolometer structure can be investigated in four groups:

- Thermal (Johnson) Noise
- Flicker (1/f) Noise
- Temperature Fluctuation Noise
- Background Fluctuation Noise

The thermal motion of charge carriers in the materials creates thermal noise. This can be expressed in current or voltage form and can be found as:

$$ri_{n,johnson} = \sqrt{\frac{4kT\Delta f}{R}} \text{ or } V_{n,johnson} = \sqrt{4kTR\Delta f} \quad (1.1)$$

where T is the temperature in terms of Kelvin, R indicates the resistance value of the material, Δf is the bandwidth, and k is the Boltzmann constant. The noise is almost constant in the entire bandwidth, in other words, it does not change with the frequency in the given bandwidth.

Flicker noise occurs because of several reasons related to the material properties. It is dominant at low frequencies due to the relationship between the frequency and flicker noise. It can be expressed as:

$$V_{n,1/f} = \sqrt{\int_{f_1}^{f_2} \frac{v_d^2 n}{f} df} \quad (1.2)$$

where f_1 and f_2 are lower and upper frequencies of the bandwidth, n is the flicker noise parameter, and f is the frequency. The flicker noise parameter is material dependent; therefore, it is possible to say that the flicker noise is determined by the active material used in the microbolometer structure. It only occurs when the microbolometer is under bias.

Temperature fluctuation noise occurs due to random variations in the temperature of the detector. When the detector is in interaction with the environment; conduction and radiation cause variations in the detector temperature, yielding to temperature fluctuation noise. It can be expressed as:

$$V_{n,tf} = \mathcal{R}_V \sqrt{\frac{4kTG_{th}}{\eta}} \quad (1.3)$$

where \mathcal{R}_V is the responsivity of the detector, k is Boltzmann constant, T is the temperature, G_{th} is the thermal conductance of the material, and η is the absorption coefficient.

Background fluctuation noise occurs due to fluctuations in the incoming infrared radiation from the environment. It can be expressed as:

$$V_{n,bf} = \mathcal{R}_V \sqrt{8A_D \eta \sigma k (T_D^5 + T_B^5)} \quad (1.4)$$

where \mathcal{R}_V is the responsivity of the detector, k is Boltzmann constant, T_D is the detector temperature, T_B is the background temperature, η is the absorption coefficient, A_D is the detector area, and σ is Stefan's constant.

The noise sources mainly construct the noise of the microbolometer. Total noise can be obtained by combining all of these noise sources as:

$$V_n = \sqrt{V_{n,johnson}^2 + V_{n,1/f}^2 + V_{n,tf}^2 + V_{n,bf}^2} \quad (1.5)$$

When all of the noise sources are compared to each other, it is seen that thermal noise and flicker noise dominate the total noise. However, it should be stated that the development of high-performance microbolometers increases the effect of thermal fluctuation noise and background fluctuation noise due to direct relation with the responsivity.

1.2.2 Responsivity

Responsivity is the ratio of conversion of output voltage or current change to incoming infrared radiation in microbolometers. ROIC structure determines the unit of the responsivity as Volts/Watts (V/W) or Amperes/Watts (A/W). In some practical applications, the unit of responsivity can be given as Volts/Kelvin or Amperes/Kelvin.

Microbolometers can be thought of as thermal circuits as shown in Figure 1-3. G_{th} is the thermal conductance and C_{th} is the thermal capacitance of the microbolometer. Power of the circuit is provided by absorbed infrared power ($\eta P_0(w)$) where η is the absorption coefficient, w is the modulation frequency, and P_0 is the incident infrared power.

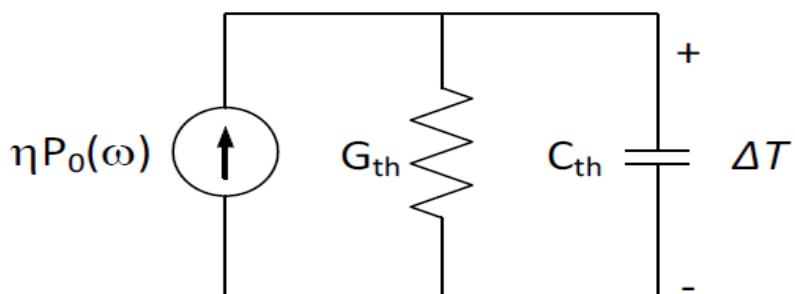


Figure 1-3: Thermal circuit representation of the microbolometer structure. [12]

Absorbed infrared power increases the temperature of the microbolometer (ΔT). The temperature difference can be estimated by analyzing the circuit as:

$$\Delta T = \frac{\eta P_0}{G_{th}\sqrt{1 + (w\tau)^2}} \quad (1.6)$$

where η is the absorption coefficient, w is the modulation frequency, G_{th} is the thermal conductance, P_0 is the incident infrared power, and τ is the thermal time constant. The time constant can be found:

$$\tau = \frac{C_{th}}{G_{th}} \quad (1.7)$$

where G_{th} is the thermal conductance and C_{th} is the thermal capacitance.

A rise in the temperature of the microbolometers (ΔT) changes the current drawn by the microbolometer yielding voltage change for current biased systems and it can be expressed as:

$$\Delta V = I_{bias} \alpha R_d \Delta T \quad (1.8)$$

where ΔV is the output voltage change, I_{bias} is the detector bias current, R_d is the detector resistance, ΔT is the temperature, and α is the temperature coefficient of resistance (TCR). By definition, voltage responsivity and current responsivity with the same idea can be found as:

$$\mathcal{R}_V = \frac{\Delta V}{P_0} = \frac{I_{bias} \alpha R_d \eta}{G_{th}\sqrt{1 + (w\tau)^2}} \quad (1.9)$$

$$\mathcal{R}_I = \frac{\Delta I}{P_0} = \frac{V_{bias} \alpha \eta}{R_d G_{th}\sqrt{1 + (w\tau)^2}} \quad (1.10)$$

Responsivity contains several parameters as seen in Equation (1.9) or Equation (1.10) related to the material properties, micromachining quality, bias voltage, or current value. For high response microbolometer, TCR and absorption coefficient should be maximized and thermal conductance value should be lowered. Moreover, the bias value and duration should be increased.

1.2.3 Noise Equivalent Temperature Difference (NETD)

NETD implies the minimum detectable temperature difference by the microbolometers. In other words, it shows the temperature difference which causes output change equal to the noise of the microbolometer. It can be thought of as one of the most important figures of merits for microbolometers and it contains almost all other performance parameters of the microbolometers. Moreover, some parameters related to the optics are included in the calculation of NETD and it can be found as:

$$NETD = \frac{4(\frac{f}{D})^2 + 1)V_n}{\tau_0 A_D \mathcal{R}_V (\Delta P / \Delta T)_{\lambda_1 - \lambda_2}} \quad (1.11)$$

where f is the focal length of the detector, D is the diameter of the optic, V_n is the total noise of the system, τ_0 is the transmission of the optic, A_D is the detector area, \mathcal{R}_V is the responsivity of the detector, $(\Delta P / \Delta T)_{\lambda_1 - \lambda_2}$ is the radiation power change of the blackbody per unit area at the temperature T .

Microbolometer optics is generally F/1 optics which means focal length is equal to the diameter of the optic. Therefore, the term of $4(\frac{f}{D})^2 + 1$ can be taken as 5. Moreover, microbolometers operate under long-wave infrared illumination which is between $8 \mu\text{m}$ and $14 \mu\text{m}$. The term of $(\Delta P / \Delta T)_{\lambda_1 - \lambda_2}$ in the spectral band is equal to the $2.62 \times 10^{-4} \text{ W/cm}^2\text{K}$ when the blackbody temperature is 295 K. For the sake of simplicity, the NETD equation can be written as:

$$NETD = \frac{5V_n}{\tau_0 A_D \mathcal{R}_V (2.62 \times 10^{-4})} \quad (1.12)$$

The NETD value shows the sensible temperature difference and it should be lowered. For this purpose, the noise of the microbolometers should be decreased and the responsivity of the microbolometers should be increased. However, there are some trade-offs between noise and responsivity values. For example, when the bias voltage

is increased, both noise and responsivity value increases. Therefore, to obtain low NETD, optimization of control parameters for microbolometers is also required.

1.3 Readout Architectures for Microbolometers

Readout integrated circuit (ROIC) is a significant part of the microbolometers making resistance change in the detector meaningful and measurable output for all pixels in the FPA. With the increasing array sizes and decreasing pixel pitches in the microbolometers, high-resolution ROICs becomes a requirement. They can be investigated in two parts: preamplifier circuits for microbolometers and readout mechanisms of pixel outputs.

1.3.1 Preamplifier Circuit Types for Microbolometers

Preamplifier circuits are one of the most important parts of the ROIC since they are responsible for analyzing resistance change in each pixel separately. Three main types of preamplifier circuits are explained in this part of the section.

1.3.1.1 Bolometer Current Direct Injection (BCDI)

BCDI type preamplifier circuits use NPN transistor to control current on the detector resistance. Moreover, for compensation of the infrared irrelevant current, reference resistance is used and it is controlled by PNP transistor as seen in Figure 1-4 [12].

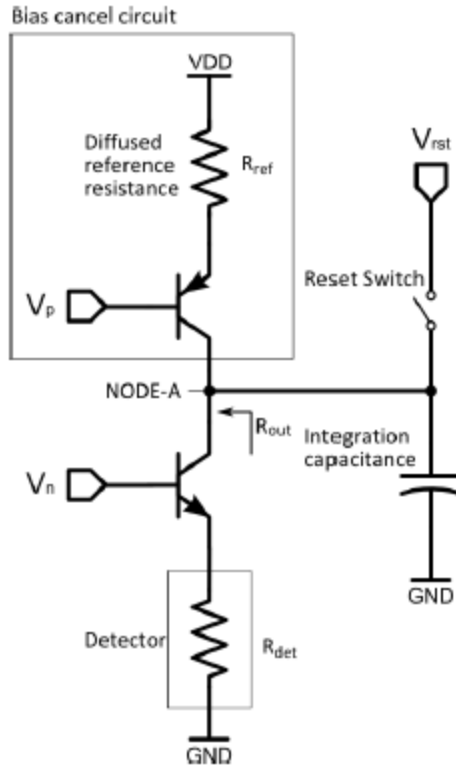


Figure 1-4: Simple schematic of bolometer current direct injection type of preamplifier circuit.

Reference resistance is theoretically the same as the detector resistance except for the property of infrared blind. However, in practical applications, resistance values of detector and reference resistances are different due to process variations. Therefore, base voltages of NPN and PNP transistors should be arranged for detector and reference resistance values, respectively. Under no infrared illumination, theoretically, the integration current is zero. When the infrared illumination changes the resistance of the detector, the output current is collected onto the integration capacitance.

BCDI type preamplifier circuit offers low noise since the noise of the BJTs is generally lower than the CMOS transistors and the resistance seen by the output of the circuit is large enough to decrease noise contribution of next stages [12]. However, the voltage on the integration capacitance can affect the detector and reference bias voltages and this creates stability problems in the structure.

1.3.1.2 Wheatstone Bridge Differential Amplifier (WBDA)

Wheatstone bridge differential amplifier is composed of four resistances: two heat sunk resistances, one reference resistance, and one detector resistance. Voltage difference on the detector and reference resistance is amplified with the differential amplifier and the signal is collected in the output via a signal generator.

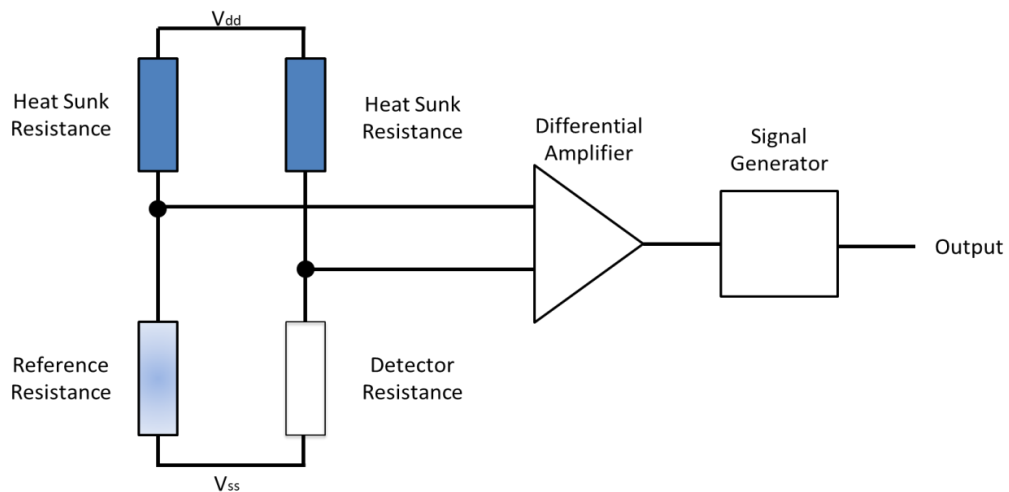


Figure 1-5: Simple schematic of Wheatstone bridge differential amplifier type of preamplifier circuit.

Heat sunk resistances in the WBDI preamplifier circuit are used to determine the voltage levels on the detector and reference resistances. The bias heating effect does not influence them since they are not suspended structures. In other words, they are thermally shorted to the substrate of the ROIC. The resistance values of heat sunk resistances are close to reference and detector resistances.

Reference resistances are infrared blind resistances; therefore, they are not affected by incident infrared radiation. However, they have suspended structures and affected by the bias heating effect. This enables to compensate bias heating effect of detector resistance.

The WBDI preamplifier circuits have a high common-mode rejection ratio resulting in low common mode noise [13]. Moreover, they are very effective in the elimination

of the detector bias offset [14]. However, detector bias voltage changes during the operation of the pixel. When the infrared illumination causes a change in the detector resistance, the ratio between heat sunk resistance and detector resistance alters. This creates non-linearity in the system. In addition to this, the deviations in the heat sunk resistances due to process variation directly affect the voltage values on the reference and detector resistances. Since there is no extra control mechanism on the voltages of the resistances, this cannot be compensated and it is amplified with the differential amplifier. The high gain of the differential amplifier is necessary to increase the response of the bolometer; however, the high gain property makes a small voltage difference, due to resistance mismatch, a considerable problem.

1.3.1.3 Capacitive Trans-Impedance Amplifier (CTIA)

A capacitive trans-impedance amplifier (CTIA) is composed of two CMOS transistors, one reference resistance, one detector resistance, and a switched capacitor integrated circuit as seen in Figure 1-6. Detector bias is responsible for the control of the current drawn by the detector resistances. The same principle is true for the reference resistance with the help of the reference bias. Reference resistance is used to compensate bias heating effect of the detector resistance like in the BCDI and WBDA type preamplifiers. Ideally, currents drawn by the detector and reference resistances are equal to each other, and the integration current can be obtained as zero. Under infrared illumination, detector resistance decreases due to negative TCR of active material in the bolometer, and detector current increases. The extra current is integrated by the switched capacitor integrated circuit, yielding output voltage.

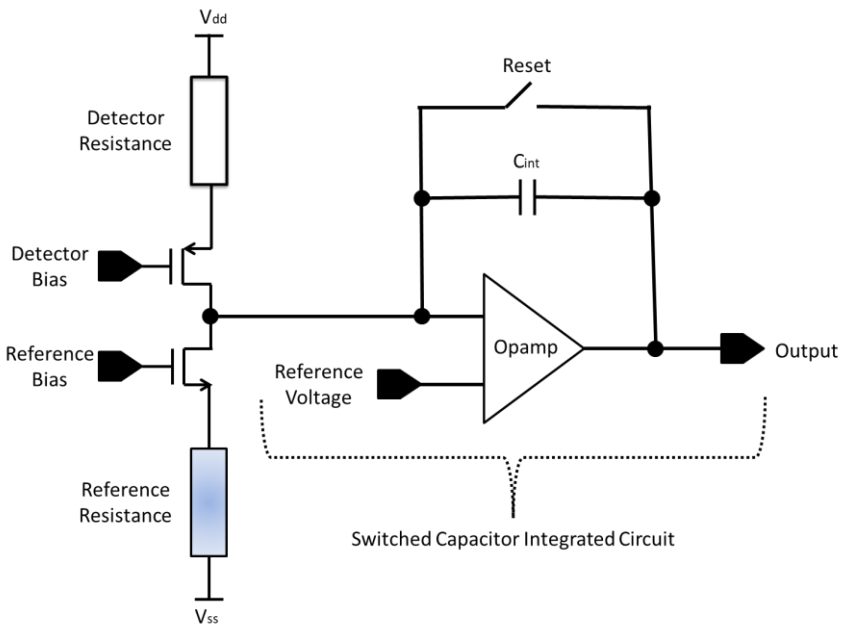


Figure 1-6: Simple schematic of the capacitive trans-impedance amplifier type preamplifier circuit.

CTIA is the most preferred preamplifier circuit due to several advantages compared to other preamplifier circuit types [15] [16] [17]. It has high sensitivity and suppresses line parasitic capacitor effects especially in large format arrays. Moreover, it provides stability in the voltage of the detector resistance as opposed to the BCDI type preamplifier circuit. The detector current is proportional to both the source-to-gate voltage of the PMOS transistor and the difference between the supply voltage and the source voltage of the PMOS. For this reason, when the detector resistance is decreased by the infrared illumination, the detector current is increased yielding to an increase in the source-to-gate voltage. However, since the gate voltage of the PMOS is constant and given by the externally, higher current increases the source voltage of the PMOS. This increase, therefore, decreases the voltage on the detector due to constant supply voltage. As a result, the current value is pushed to be decreased. This situation lowers the variation in the detector current due to infrared illumination and provides stability in the detector voltage. However, it reduces the responsivity of the detector.

1.3.2 Readout Operation of Pixel Outputs

ROICs for microbolometers are developed continuously to make the performance of the microbolometer based infrared cameras detector limited [18] [19] [20] [21] [22]. Moreover, large format sizes and small pixel pitches make the ROIC design for microbolometers a challenging issue. Therefore, the microbolometer readout structure can be changed concerning the design of the ROIC; however, there are some main parts in each microbolometer ROIC as seen in Figure 1-7.

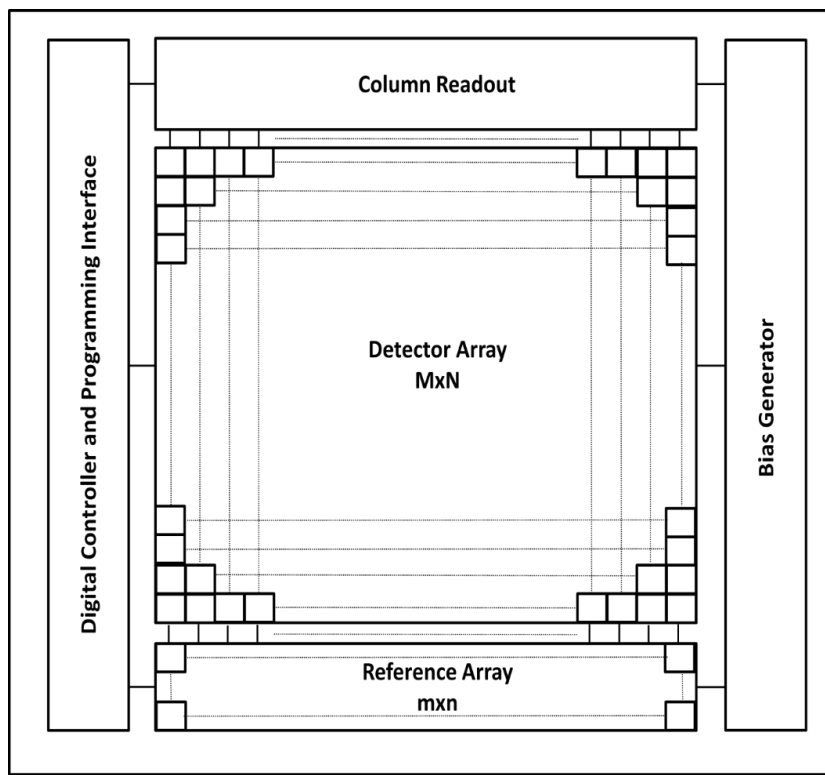


Figure 1-7: Demonstration of the top-level block diagram for microbolometer ROIC.

The digital controller circuit in the ROIC is responsible for the construction of necessary digital signals such as integration time, row selection, etc. It is not possible to read all pixel outputs at the same time. Therefore, the read operation is done consecutively and the digital controller circuit arranges this, which is also true for the bias mechanism of the pixels. Moreover, determination of bias time, bias voltage value, column readout gain, and timings such as line time and sampling times is done

by the digital controller circuit. For these reasons, the digital controller circuit is connected to all blocks in the microbolometer ROIC to adjust the required timing and values. These adjustments should be done to work the ROIC properly and optimize the performance of the microbolometer to data externally. The data is generally sent from an FPGA board and this situation requires a programming interface in the ROIC. Therefore, the digital controller circuit works in collaboration with the programming interface. The programming interface is a generally serial peripheral interface (SPI) [20] [23] or LVDS interface [19].

The detector array is composed of detector resistance processed by MEMS technologies. ‘M’ and ‘N’ indicate the row and column numbers, respectively. The size of the detector array can change a lot for design and application.

Reference array is another block in the ROIC design and electrical characteristics of reference resistances are very similar to the detector resistances. The difference is the thermal and infrared characteristics to eliminate the bias heating effect. Reference resistances are shared by detector resistances, in other words, it is not produced a reference resistance for each detector resistance due to limitations in the layout area. ‘m’ and ‘n’ show the array size of reference resistances in terms of row and column, respectively. The array size is much lower than the one for the detector array. The main drawback of the structure is that the anomalies in the reference resistances due to the process variations are shown in many pixel outputs because of the sharing mechanism. Moreover, thermal time constants of the reference resistances should be arranged to prevent them from overheating or burned during the imaging. Therefore, the array size of the reference resistance plays a crucial role to obtain high-performance microbolometers, and optimization is needed to use enough layout area without degrading the performance of the microbolometer in the case of process anomalies. In some enhanced ROIC structures [12], reference selection is possible to decrease the dead pixel ratio in the FPA. These structures enable to use of only functional reference resistances during operation.

The bias generator produces required currents and voltages for other blocks in the ROIC. The number of the external bias source is minimized in the ROICs to decrease the noise level and variation between bias values. The challenge in the design of the bias generator is to make it supply and temperature independent. It is divided into two sub-blocks: voltage DACs and current DACs [24]. In some ROICs [12], these blocks are also divided concerning target blocks such as low noise voltage DAC.

The column readout is responsible for the conversion and transmission of differentially integrated output current into the output voltage. It is shared in all pixels for each column in the FPA. It is composed of three main parts: an integrator circuit, a sample-hold circuit, and an output buffer. The integrator circuit collects the differential current which is coming from the preamplifier circuit during the integration time at the output stage of the op-amp as seen in Figure 1-8.

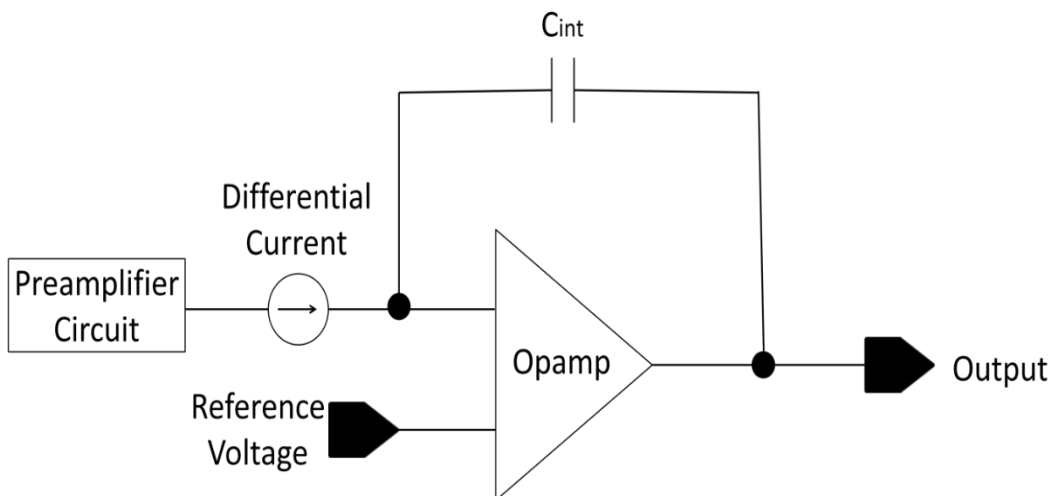


Figure 1-8: Schematic demonstration of integrator circuit used in microbolometer ROICs.

The output of the integrator circuit is connected to a sample-hold circuit to keep the integrated current on the capacitor. The voltage is sent to the output stage of the ROIC via the output buffer system only when the column is selected by the digital controller circuit where the columns are selected consecutively. An output buffer system is used to prevent charge sharing effects. The analog outputs are generally converted into digital data by the external ADC or ASIC in the imaging systems.

However, in some ROIC designs [25], ADC is implemented into the ROIC to noise optimization and reduce the complexity of the imaging system.

1.4 Control Parameters for CTIA Type ROICs

Conventional CTIA type ROICs collect the current difference between detector and reference branch at the output after integrating it. During the procedure, modifications in the structure can increase the performance of the microbolometer camera. For this reason, some control parameters are implemented into these types of ROICs. The parameters can be analyzed as two groups: the integration time and bias on the active detector resistance.

Integration time indicates the duration of the voltage on the active detector resistances for each frame. When the integration time increases, the collected current difference at the output increases and this causes higher noise and response. However, an increase in the response is dominant to one for noise [26]. At this point, it can be seen as reasonable to make integration time as high as possible to obtain high-performance microbolometers as shown in Figure 1-9.

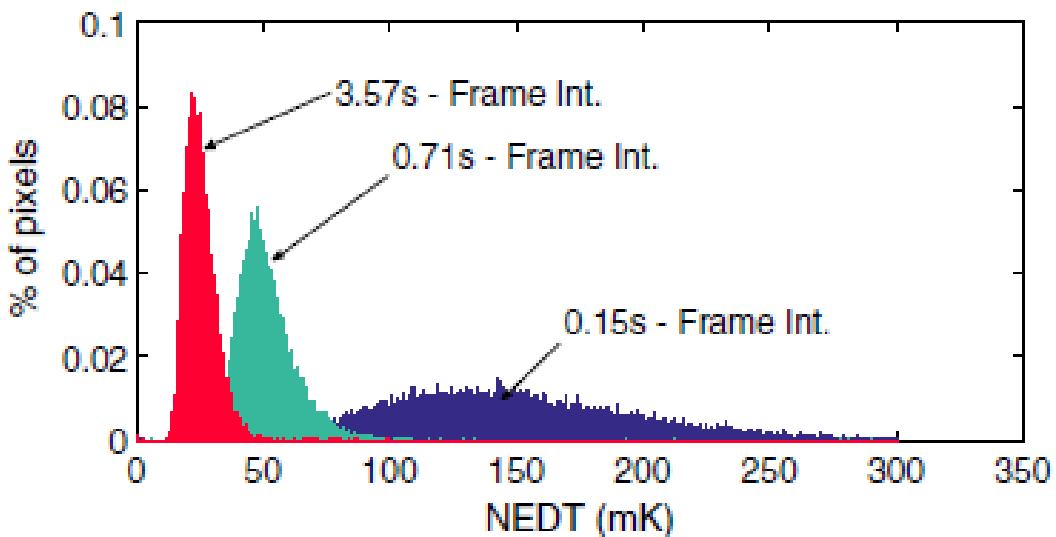


Figure 1-9: Effect of integration time on noise equivalent difference of temperature (NEDT) [27].

Integration time is limited by frame time and array size of the microbolometer FPAs although it should be increased for higher performances. During the operation of microbolometer cameras, biasing and reading operations of all pixels in the FPA should be performed for each frame. Generally, the frame time of the microbolometer cameras is 30 but some studies are performed to obtain high-speed cameras that work with 60 FPS [28]. Moreover, the frame time is also limited by the thermal time constant and the balance between these parameters should be arranged to increase microbolometer performance.

Bias on the detector resistance is another important control parameter of the ROIC which affects the microbolometer performance. Since active materials of the microbolometers have negative TCR, current bias is preferred to stabilize the system. In the CTIA type ROICs, the current bias is controlled via transistors as explained in Capacitive Trans-Impedance Amplifier (CTIA). The current drawn by the reference resistance does not affect the performance and it is used only bias heating compensation. Indeed, the current drawn by the reference resistance can affect the total noise of the microbolometer but it can be negligible. The reference current is set to almost the same as the detector current, which has a great impact on the performance. Like the integration time, the performance of the microbolometer increases with the bias as seen in Figure 1-10.

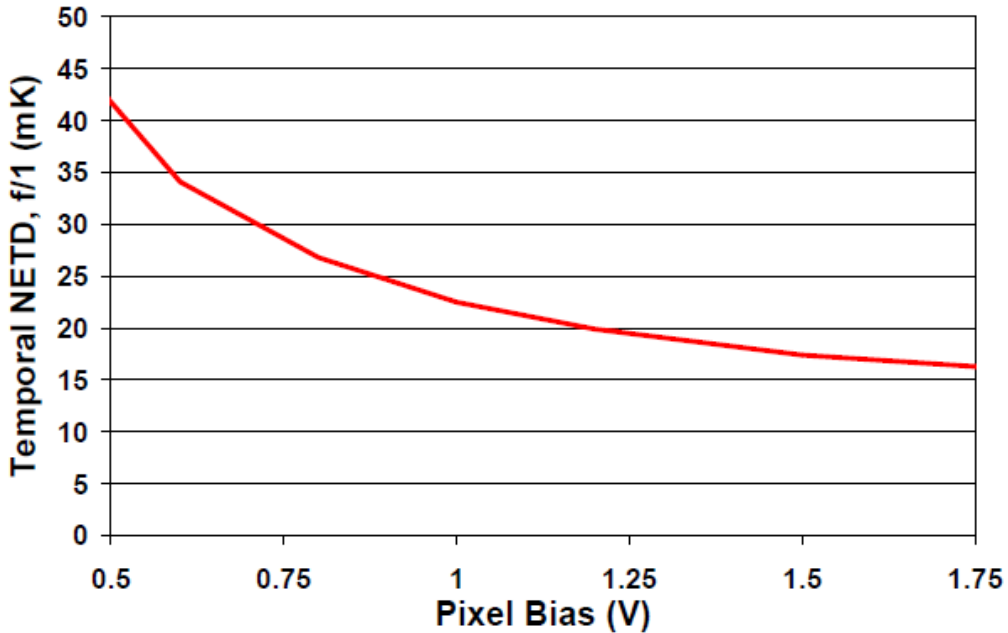


Figure 1-10: Effect of pixel bias on noise equivalent temperature difference (NETD) [29].

Detector resistance bias is limited with the ROIC features and active pixel structures. The current on the detector resistance should be maximized without burning the active pixel structure in the range of ROIC capabilities. Moreover, some extra factors restrict bias such as variations in resistances over FPA. They will be explained in the following section.

1.5 Resistance Nonuniformity

Resistance values in the FPA are optimized in the process of microbolometers to obtain higher performance. In theoretically, optimum detector resistance is determined and reference resistance is designed concerning the detector resistance [30]. However, resistance values alter due to inevitable nonuniformities in the process as seen in Figure 1-11. Therefore, producing uniform resistances via FPA is a challenging issue as much as optimizing the microbolometer pixel process.

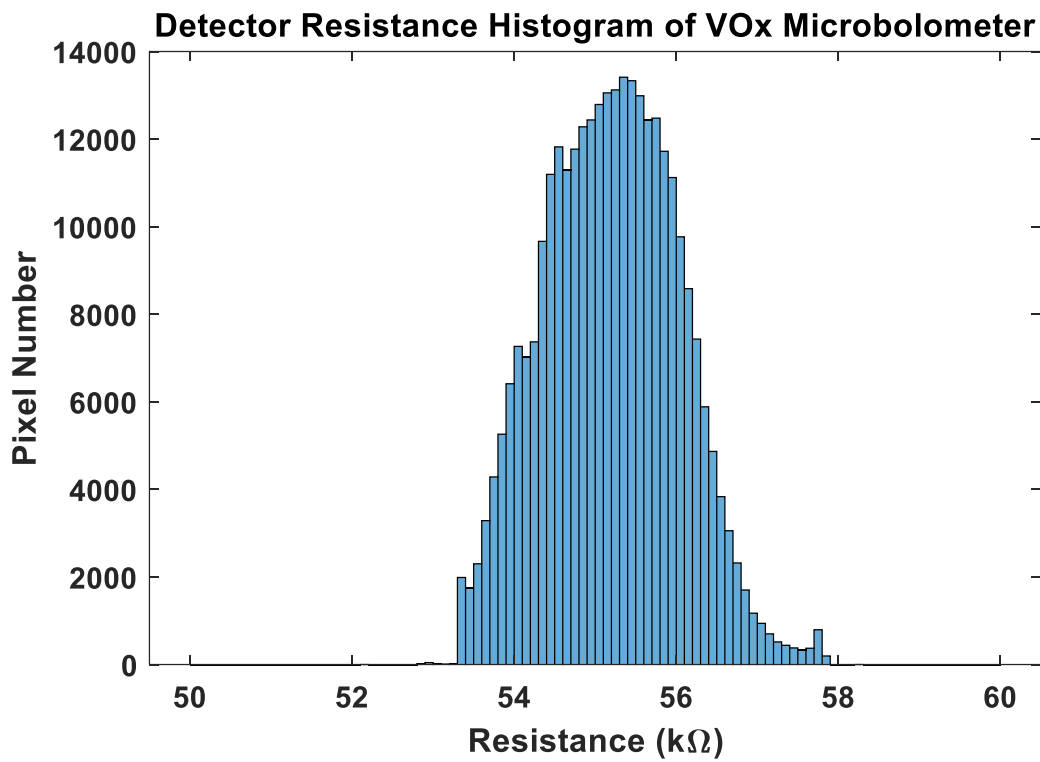


Figure 1-11: Detector resistance distribution of vanadium oxide microbolometer array (640x480) produced in METU MEMS Center. The pixel pitch is 17 μm .

The value of reference resistance should be the same as the detector resistance values but they should be infrared blind. However, there is nonuniformity between reference resistances like detector resistances. A reference resistance is needed for each detector resistance in the CTIA type ROICs. However, the number of reference resistances is much smaller than detector resistances in microbolometer FPAs due to size constraints and they are shared during imaging application. This situation increases the importance of uniformity in reference resistances.

The number of reference resistances can change with the design of the ROIC. One reference resistance for each column can be used consecutively [31] or the number may be more than one for each column [30]. Since shared reference resistances are biased much more times from detector resistances in a frame, the heating mechanism should be optimized concerning the number of used reference resistance. In the study completed in METU MEMS Center [30] in 2008, the effect of the reference

resistance number is analyzed in terms of the heating mechanism as seen in Figure 1-12. It is seen that heating behaviors of the reference resistances vary even if their thermal conductance values are almost the same. A higher number of reference resistances improve thermal stability yielding better uniformity. However, reference resistance variations increase with the number of reference resistances and this affects the uniformity negatively. Therefore, it is reasonable to produce a higher number of reference resistances than the required number and make selections from them.

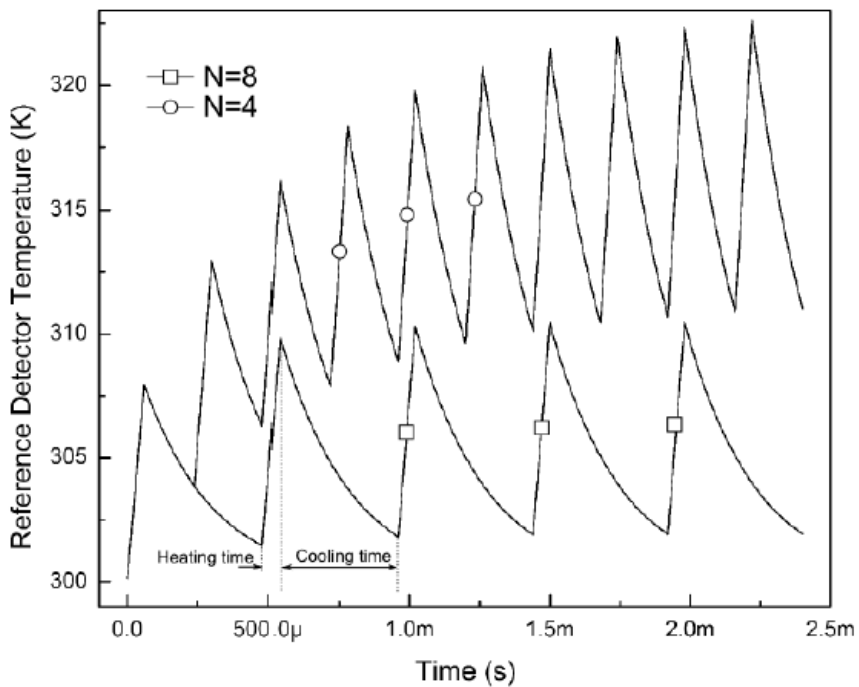


Figure 1-12: Reference resistance temperature change to the number of reference resistance used during imaging. The reference resistances have almost the same thermal conductance which is 20×10^{-7} nW/K [30].

Nonuniformities due to resistance variation in detector and reference resistances should be compensated before imaging. The compensation method aims to make all output pixel currents equal when there is no infrared illumination. There are several methods of compensation such as bias heating [32] and voltage regulation for each pixel. The purpose of the bias heating compensation method is to make all resistance values equal with the help of external CMOS resistances and heating the resistances.

In the study developed in METU MEMS Center [32], it is reported that the bias heating compensation method is equal to 13-bit DAC. On the other hand, voltage regulation methods aim to set each pixel bias concerning its resistance value. In the scope of the thesis, voltage regulation methods are investigated.

Voltage arrangements are controlled with the help of DACs [12] [24] [33] [34] for voltage regulation methods. For each pixel, the voltage which controls the current drawn by detector resistance is set to the optimum value. A memory that stores these optimum values can be implemented into the ROIC for small format arrays such as 160x120. Moreover, the calibration can be done automatically for these ROICs with the modification in the digital controller [35] [36]. The working principle depends on observing a uniform scene and save these images. Pixel bias values are updated by using these images and the procedure is repeated until the nonuniformity of the output distribution reaches the desired value. However, in large format arrays such as 640x480, external memory is required due to size constraints. The calibration data is saved into the external memory with the help of the interface of the ROIC.

Performance of the compensation depends on the resolution of DACs responsible for bias voltages. To obtain high performance, it is beneficial to design DACs which have a small step size. However, the higher resolution of the DACs causes a larger layout size and higher power consumption. In addition to this, the noise contribution of the DACs increases with the resolution and this increases the minimum obtainable NETD of the microbolometer. To solve the problem, two-stage DACs are developed [12]. The first stage of the DAC determines the minimum and maximum voltages of the second stage of the DAC. These DACs are controlled consecutively to find optimum points for each pixel. However, finding optimum points for large format array microbolometers is another challenging issue. There are two conventional methods to find these optimum values which are the sweep method and binary search method [37]. These methods and the proposed method will be explained and analyzed in CHAPTER 2.

Two-stage DACs provide fine-tuning for the pixel bias values; however, all of the pixel outputs cannot be at the desired value. Since it is not possible to give exactly the required bias values for pixels due to the nature of DACs, which is called quantization error. Additionally, there may be wrong calculations in the process of finding the optimum bias values. Therefore, after estimating optimum bias values for the pixels, software-based corrections are applied to obtain higher uniformity before imaging. Residual nonuniformity (RNU) is mostly preferred as a performance criterion for uniformity. To calculate RNU value, the mean of the pixel output histogram should be calculated firstly and it can be expressed as:

$$Out_{mean} = \frac{\sum_{i=1}^m \sum_{j=1}^n Y_{i,j}}{m * n} \quad (1.13)$$

where m and n are row and column numbers in the FPA respectively, $Y_{i,j}$ indicates the pixel output at the column j and row i , and Out_{mean} shows the mean of the output histogram. After this, the standard deviation of the pixel output histogram should be found and it can be shown as:

$$S = \sqrt{\frac{\sum_{i=1}^m \sum_{j=1}^n (Y_{i,j} - Out_{mean})^2}{m * n}} \quad (1.14)$$

where S is the standard deviation of the histogram. Finally, RNU can be found as:

$$RNU = \frac{S}{Out_{mean}} \quad (1.15)$$

PSNR is another performance criterion for uniformity and it can be calculated as:

$$PSNR = 10 * log_{10}\left(\frac{(2^k)^2}{\frac{1}{m * n} \sum_{i=1}^m \sum_{j=1}^n (Z_{i,j} - Z'_{i,j})^2}\right) \quad (1.16)$$

where k is the number of bits at the output, $Z_{i,j}$ is the reference image, and $Z'_{i,j}$ is the estimated image. It is used to analyze the performance of the algorithm by using real infrared images.

Conventional software-based corrections can be divided into two categories: 1-point correction and 2-point correction [38]. It is important to state that software-based

corrections improve only image quality and there is no effect on the performance parameters of the microbolometer.

1-Point correction, also known as offset correction, brings all pixel outputs to the same point by adding or subtracting values from pixel outputs. The target value is generally the mean value of the output distribution but it can be set at any point for the application. For calculation of the offset values, the microbolometer is exposed to uniform infrared illumination via blackbody or closing the lid of the camera lens. Many frames are saved at this condition and the average of them is saved, which is called a dark image. The purpose is to prevent high errors in the calculation due to the noise of the pixel outputs. The dark image can be expressed as:

$$D_{i,j} = \frac{\sum_1^n R_{i,j}}{n} \quad (1.17)$$

where D and R indicate the dark and raw images respectively, i and j are row and column numbers of the pixel, and n is the number of frames taken. After the dark image is obtained, the pixel output values are subtracted from the target value which the pixel outputs are desired to be collected at, and therefore offset values are calculated. The expression for 1-point correction can be shown as:

$$O_{i,j} = T - D_{i,j} \quad (1.18)$$

where T indicates the target value which is the same for all pixels and $O_{i,j}$ indicates the offset value for the pixel.

1-Point correction assumes that response values of the pixels in the FPA are constant. Therefore, the quality of the correction strongly depends on the response distribution of the FPA. To handle this issue, a 2-point correction method is used and it consists of gain and offset correction. Two calibration points which are uniform infrared illumination at different temperatures are needed for 2-point correction as seen in Figure 1-13.

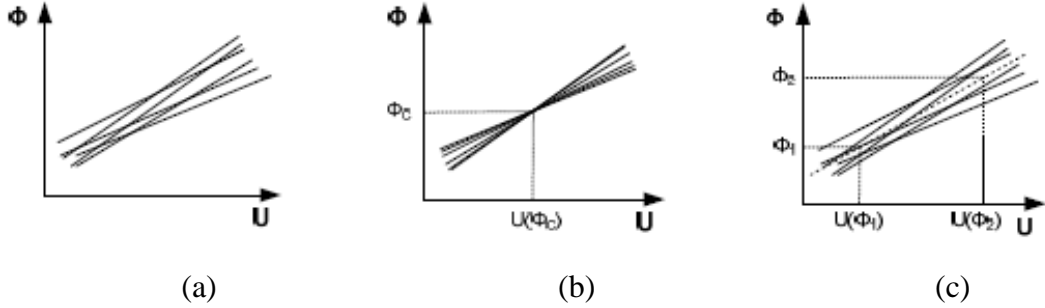


Figure 1-13: (a) Output of different pixels for infrared power, (b) output curves after 1-point correction is applied, and (c) output curves after 2-point correction is applied [39].

Dark images are saved for 2-point correction in the same way as the 1-point correction. After this, frames against uniform infrared illumination higher than dark case are saved additionally and the average of them is calculated, which is called a flat image. Firstly, gain coefficients of pixels are calculated by using the difference between dark and flat images. It can be shown as:

$$G_{i,j} = \frac{\frac{1}{m * n} \sum_{i=1}^m \sum_{j=1}^n (F_{i,j} - D_{i,j})}{F_{i,j} - D_{i,j}} \quad (1.19)$$

where D and F indicate the dark and flat images respectively, m and n are the number of rows and columns in the FPA; i and j are row and column numbers of the pixel, and G shows gain of the pixel. After the gain array is calculated, the offset array is calculated using a dark or flat image, and the expression is written as:

$$O_{i,j} = T - G_{i,j} * D_{i,j} \quad (1.20)$$

where T indicates the target and $O_{i,j}$ indicates the offset value for the pixel. During imaging, raw pixel outputs are modified as:

$$Y = G * R + O \quad (1.21)$$

2-point correction provides high uniformity because of response difference compensation. The quality of the correction degrades when the difference between calibration scene temperatures and observed scene temperature is increased due to the nonlinear response characteristic of microbolometer arrays and therefore some

improved 2-point calibration methods are developed [40]. However, in the scope of the thesis, the 2-point calibration method is used as the software-based correction.

1.6 Effect of Temperature on Calibration Parameters of Microbolometers

Microbolometer structures are designed as highly sensitive to temperature so that response of the microbolometer becomes high and active materials are optimized to obtain high TCR values. Although these optimizations improve microbolometer performance, the effect of microbolometer temperature change on the pixel outputs increases. For CTIA type ROICs, pixel output depends on the current difference between the detector and reference resistances. It can be expressed as:

$$I_{out} = I_{det} - I_{ref} = \frac{V_{det}}{R_{det}} - \frac{V_{ref}}{R_{ref}} \quad (1.22)$$

where I_{out} is the output current before integration procedure, I_{det} and V_{det} are the detector resistance current and voltage respectively, and I_{ref} and V_{ref} are the reference resistance current and voltage respectively. When the temperature of the microbolometer is changed, the new output current can be shown as:

$$I'_{out} = I'_{det} - I'_{ref} = \frac{V_{det}}{R_{det}(1 + \alpha_{det})^{\Delta T}} - \frac{V_{ref}}{R_{ref}(1 + \alpha_{ref})^{\Delta T}} \quad (1.23)$$

where I'_{out} is the output current at the new microbolometer temperature, α_{det} and α_{ref} are TCR values of detector and reference resistances respectively, R_{det} and R_{ref} are resistance values of detector and reference, and ΔT is the temperature change for the microbolometer. Although the active material of detector and reference resistances is the same, differences in TCR values of them are observed due to process variations. Moreover, variations in the process cause resistance differences between the detector and reference resistances. Therefore, pixel outputs are affected strongly by the microbolometer temperature.

Thermoelectric coolers (TECs) are used to stabilize microbolometer temperature, however, TECs increase size, cost, and especially power consumption of microbolometer camera. Due to these disadvantages, TECless microbolometer cameras are developed. This requires the compensation of output change because of the microbolometer temperature change. These algorithms contain many parameters since the output change of pixels to the temperature depends on both resistances and their TCR values.

Compensation methods have been studied a lot in recent years and different approaches are proposed. These methods can be grouped as seen in Figure 1-14.

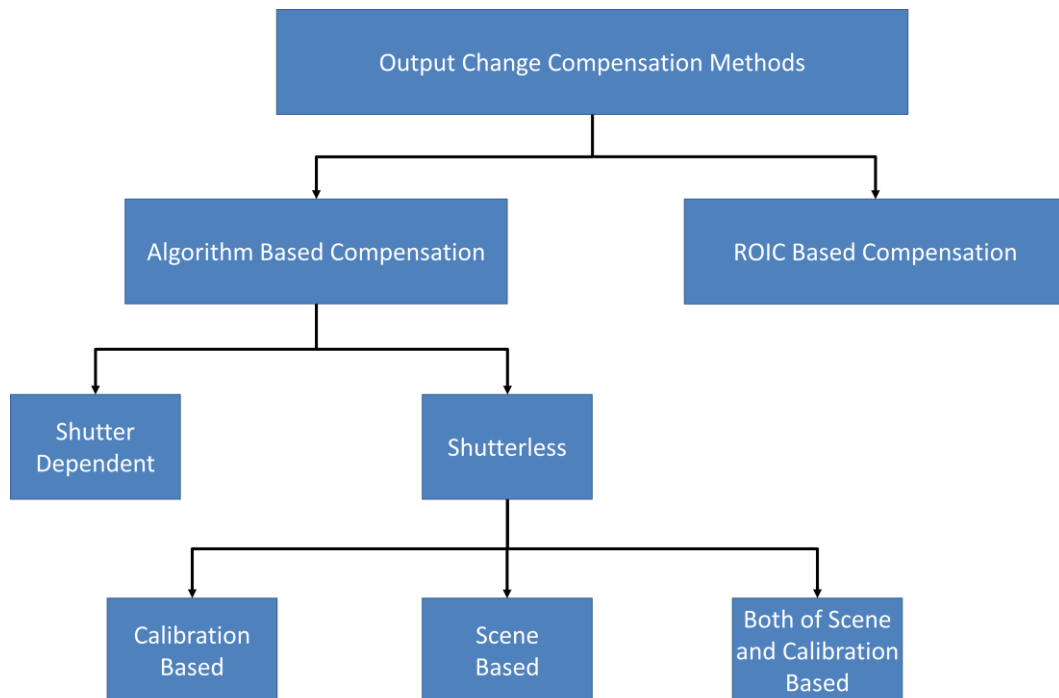


Figure 1-14: Groups of compensation methods for output change due to temperature variations.

ROIC based compensation methods depend on the feedback mechanism from the extra feedback loop and extra resistances in the readout architecture [41] [42]. The main drawback of these algorithms is an inevitable increase in the noise of the ROIC due to implemented extra features that limits the minimum obtainable NETD.

Moreover, these extra features increase the complexity and size of the ROIC. For this reason, algorithm-based compensation methods are more preferable.

Algorithm-based compensation methods can be divided into two categories as seen in Figure 1-14 which are shutter dependent and shutterless. For shutter dependent algorithms, pixel bias values are calculated at initial conditions. Additionally, gain coefficients can be calculated and kept constant for all temperature ranges. After this, an opaque shutter is used to calculate offset coefficients. When the shutter is closed, several frames are saved, and the average of them is calculated. The average is multiplied with the gain initially and subtracted from the desired output. After this, the shutter is opened and the thermal camera starts imaging. The procedure is repeated periodically to update offset coefficients [43]. It is important to calibrate the use of the shutter since dark conditions cannot be obtained exactly with the shutter. Therefore, some studies are performed such as using multiple temperature sensors on the optical path between the detector and the shutter [44]. It provides high uniformity thanks to periodic calibration; however, frames are lost when the shutter is closed. Moreover, a decrease in the number of shutter use results in worse uniformity. The use of a translucent shutter is proposed instead of an opaque shutter to prevent frame loss due to calibration [45]. However, in the study, the performance of the compensation is lower than compared with the ones which use an opaque shutter. In addition to this, the complexity of the compensation algorithm is increased considerably due to the contribution of external infrared illumination during calibration. In other words, to improve the efficiency of the algorithm, the scene of the camera should be stationary while the calibration phase. In addition to these drawbacks, the use of a shutter increases power consumption and the size of the camera significantly. Therefore, shutterless algorithms are developed to prevent frame loss and reduce power consumption and the size of the camera. Nevertheless, shutter-dependent TECless cameras are used in many applications where frame loss is not much important thanks to high performance.

Frame lost cannot be acceptable in some application fields such as security, military, etc. For this reason, shutterless thermal cameras are developed. Moreover, they are

more suitable for the systems in which small size or power consumption of the camera is more important than the performance of uniformity. They estimate software-based correction parameters concerning the temperature of the microbolometer to enable continuous imaging without frame loss by degrading the uniformity as small as possible when compared to the shutter dependent TECless cameras. They can be grouped as calibration-based, scene-based, and both calibration and scene-based as shown in Figure 1-14.

Calibration based algorithms use correction parameters which are found at different temperatures of the microbolometer with the experiments. The simplest method is to save these correction parameters into the memory and use them concerning the temperature of the microbolometer. There is an inverse relationship between the number of correction data in the memory and output nonuniformity. This situation results in the requirement of large memory in the microbolometer camera core. Moreover, experiment time is increased considerably when the number of correction data is increased. For these reasons, improved calibration-based algorithms depend on the idea of modeling correction parameters with acceptable error rate after the minimum number of experimentally measured correction data.

Modeling of correction parameters strongly depends on the active material characteristics of the microbolometer. Vanadium oxide (VO_x) and amorphous silicon (a-Si) are used as an active material for the microbolometers [46]. Vanadium oxide provides high TCR yielding to high responsivity however temperature dependency of the TCR is complex due to temperature-dependent activation energy. On the other hand, amorphous silicon is more suitable for shutterless applications although its TCR is lower than vanadium oxide. Since amorphous silicon has almost constant activation energy, the TCR of the material can easily be fitted into the Arrhenius equation [47]. When the TCR information is fitted with a small error, it is easy to estimate resistance values at different temperatures and therefore optimization process for bias values and software-based corrections becomes straightforward. However, in the thesis, software-based correction parameters are optimized for vanadium oxide type microbolometer cameras due to their high performance.

Calibration based algorithms have been developed with different perspectives over the years. In 2009, offset parameters are estimated by fitting the measured offset values at certain points into second-order polynomial function in the temperature range from 23 °C to 35 °C for the microbolometer [48]. The residual nonuniformity (RNU), which is the ratio of standard deviation into the mean of the output histogram, is kept below 1%. However, in the work, when the temperature range is raised (between 10 °C and 45 °C), the fit equation gives a high error although the polynomial function is changed into the third order. In 2015, microbolometer response is modeled as a second-order polynomial function, and offset estimation is done by fitting the coefficient for the first order of the function into the linear function to temperature [49]. The linear regression is not applied to all pixels, in other words, it is done globally. Obtained uniformity results are compared with the one which is found by using shutter dependent algorithm and it is seen that RNU value is increased up to almost twice of the value with shutter when the blackbody is 25 °C. Moreover, the RNU is getting worse when the scene temperature changes. In addition to this, column-based nonuniformities are observed due to mismatches of the reference resistances. This shows that the performance of global linear regression for the fit depends on the reference resistance uniformity. Nevertheless, the algorithm is easy to implement into microbolometer cameras and suitable for real-time application due to its simplicity in the fitting. In 2016 [50], offset coefficients are fitted into the third-order polynomial functions for improved thermal camera compared to the camera in the study performed in 2009. In addition to this, three temperature sensors are placed into the camera housing at different locations. The coefficients of polynomial functions are also modeled to data collected from temperature sensors. Although significant improvement in the uniformity is observed when the number of coefficients for each pixel is increased, a huge number of coefficient arrays requires huge memory and an extremely long calibration time. Offset and gain coefficients are fitted into the linear equations from -10 °C to 50 °C for microbolometer temperature in the study in 2017 [51]. No performance parameter for the uniformity is given and obtained images with the improved algorithm are

compared with the standard case which does not contain any temperature change compensation method. The images indicate that the algorithm improves the uniformity; however, the stability of the algorithm with a wide temperature range is not given. Moreover, there is no information given about the active material of the camera whereas TCR characteristics of the active materials play an important role in the error in the fit equation. In the other study done in 2017 [52], the piecewise interpolation method is used to estimate offset coefficients. Experimentally calculated offset arrays for each 5 °C are stored in the memory for the temperature range between -40 °C and 60 °C. Results show that RNU values can be kept below 1% ignoring some points for the given temperature range. However, the images from which RNU values are calculated are taken in dark conditions and there is no information is given when the scene temperature dependency of the algorithm. In addition to this, there is no information about bias optimization and the active material of the microbolometer. In summary, calibration-based compensation methods have been improved continuously to obtain closer uniformity performance to the shutter dependent compensation methods although analysis for these methods are time-consuming and require measurement systems such as blackbody and temperature chamber.

Scene based algorithms depend on the calculation of correction parameters continuously according to change in the scene. In other words, the working principle can be explained that scene movements are analyzed statistically to determine offset correction continuously. Temperature drift can be compensated immediately thanks to continuous recalibration process; however, they are sophisticated compared to calibration-based algorithms and suffer from stripe noise and ghosting artifacts which is can be explained as a shade of the objects remains in the image whereas the object moves in the scene. Special operations are needed in the algorithm in order to decrease these artifacts [53] [54] [55] [56] [57]. Although the operations reduce the degradation of these artifacts in the uniformity, they make the algorithms more complex.

There are some studies about a combination of calibration based and scene-based algorithms. Firstly, correction parameters are estimated with the number of calibration data and after this, scene-based algorithms are applied to reduce error in the estimation of the parameters [58] [59] [60]. However, real-time estimation of parameters with additional scene-based algorithms makes the algorithms complex and hard to implement for imaging systems.

A calibration-based shutterless algorithm is preferred in the thesis due to suitable for real-time application and independence from the scene. Details of the proposed algorithm will be explained in CHAPTER 3.

1.7 Research Objectives and Thesis Organization

Throughout this section, operating principles of microbolometer imaging systems and performance criteria related to these systems have been discussed. An increase in the array size makes compensation of nonuniformity between pixel outputs more difficult and significant. Moreover, small size and low power requirements for microbolometer cameras result in the necessity of improved TECless and shutterless systems. Purpose of the thesis work is to provide shutterless algorithm without degradation of performance significantly for the microbolometer which has 17 μm pixel pitch and 640x480 array size. For this reason, the proposed algorithm should contain:

- An algorithm to find optimum digital input values for DACs which are responsible for the biasing to decrease output nonuniformity as much as possible.
- Software-based corrections to keep output nonuniformity as low as possible in the operational temperature range of the microbolometer.
- Update in optimum digital input values for the DACs and software-based correction parameters with respect to temperature of the microbolometer to compensate for the effect of temperature change.

Organization of the thesis can be explained as:

CHAPTER 2 mentioned about optimization of the microbolometer for uniformity at the steady-state case, in other words, when the temperature is stabilized. The optimization contains an algorithm to find optimum digital inputs of the DACs and software-based correction. These algorithms are written and developed in Matlab. In addition to this, the section includes improvement in the uniformity with the proposed algorithm for different microbolometers.

CHAPTER 3 shows the effect of temperature on the uniformity and explains the algorithm to estimate digital input values for the DACs and software-based correction parameters to lower the output nonuniformity. Moreover, results obtained from different microbolometers related to the output uniformity when the proposed algorithm is applied are compared in the section. Matlab is used to apply the algorithms and calculate performance parameters of the uniformity.

CHAPTER 4 gives a summary of the thesis works and mentions what should be done to improve uniformity in the future.

CHAPTER 2

UNIFORMITY OPTIMIZATION AT STEADY STATE CASE

The microbolometer camera in the thesis uses a CTIA type readout circuit as seen in Figure 2-1. Array size of the microbolometer is 640x480, which means there are 640 columns and 480 rows in the FPA and the pixel pitch is 17 μm . Integration time can be controlled and increased up to 50.3 μs and reference voltage for the op-amp is controlled with DAC. Moreover, the circuit has two-stages DACs to control bias voltages for detector and reference resistances, and the output voltage is converted into digital values via 14-bit external ADC.

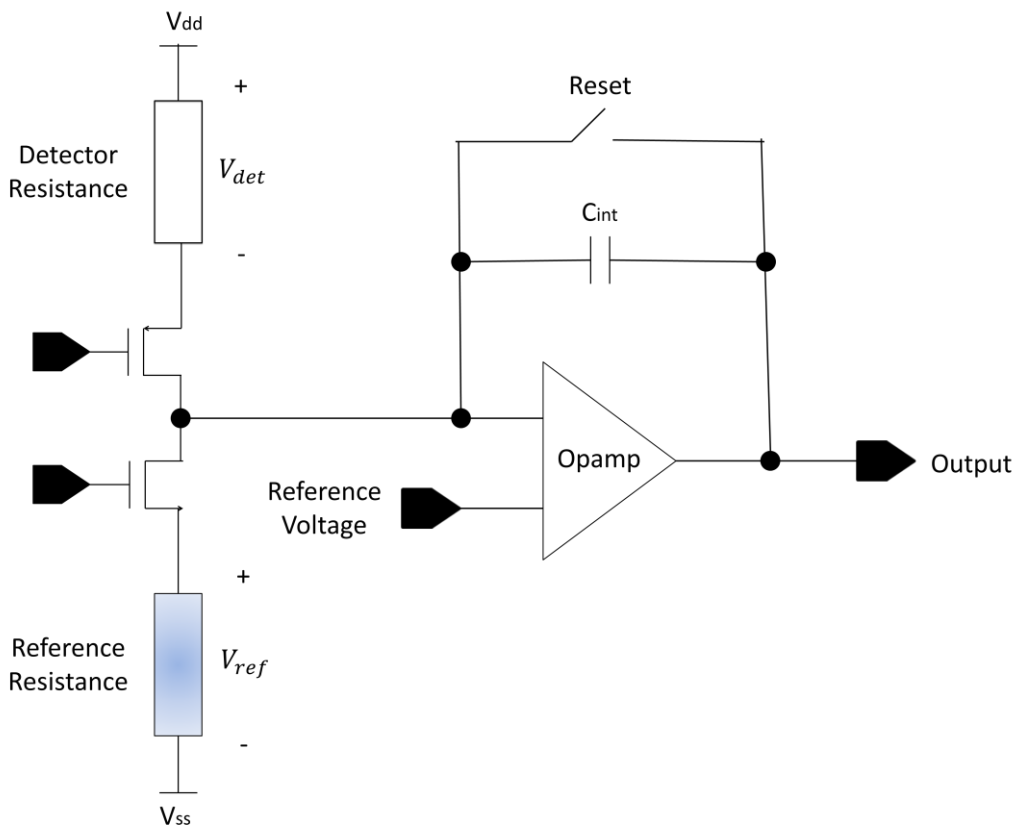


Figure 2-1: Pixel readout circuit of the microbolometer which is used in the thesis.

All measurements in the chapter are done with the setup as shown in Figure 2-2. The microbolometer is placed into the PCB which is designed for microbolometer measurements and located inside of the Dewar. Frame grabber cable is used to provide communication between the microbolometer and computer with the help of the FPGA board which is also configurated for the microbolometers. The power supply gives the required voltages to work components properly. The vacuum pump is used to create a vacuum environment for the microbolometer due to its suspended structure. TEC controller enables to set the temperature of the microbolometer into the desired temperature between 0 °C and 50 °C. The microbolometer is controlled via software developed by Mikro-Tasarim.

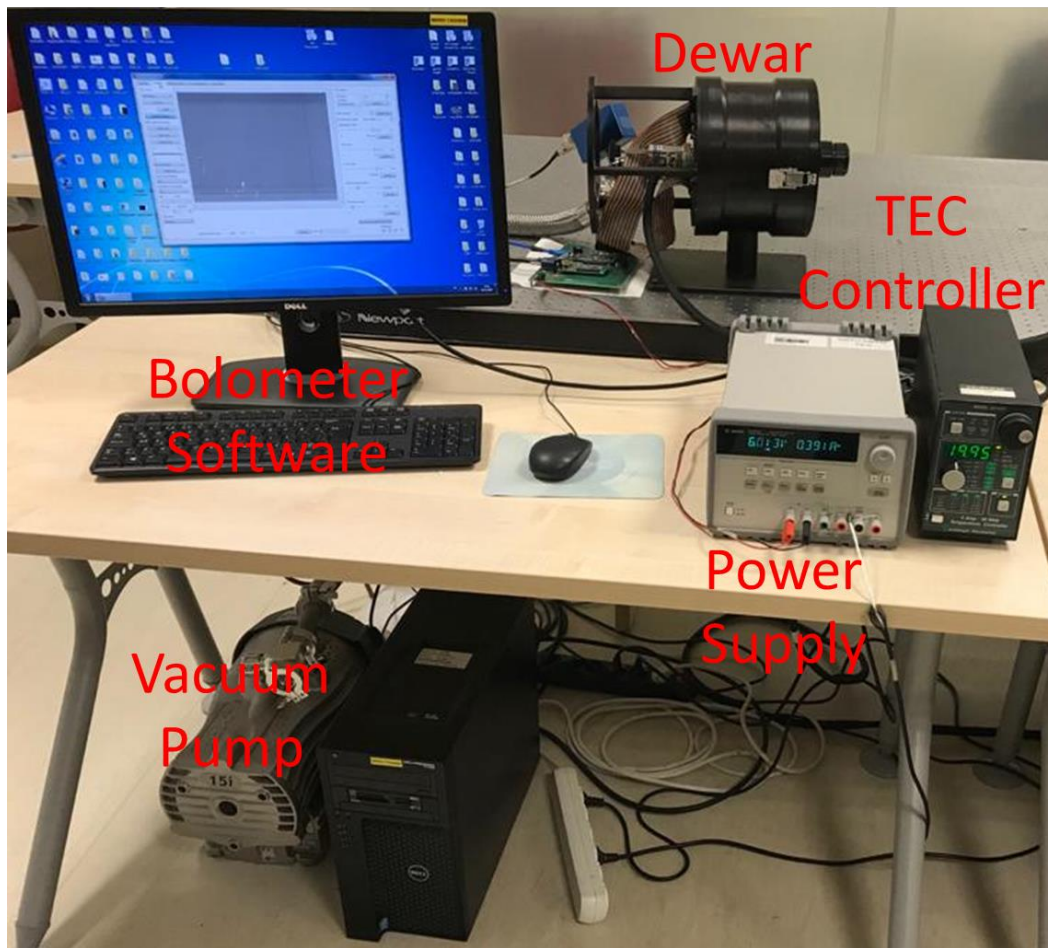


Figure 2-2: Measurement setup for microbolometers configurated in METU MEMS Center.

Integration time indicates the duration of pixel bias and the effect of resistance nonuniformities between pixels increases with the integration time. In other words, there is an inverse relationship between the output uniformity and the integration time. However, it is known that an increase in the integration time improves the NETD performance of the microbolometer as seen in Figure 2-3. Therefore, all measurements shown in the thesis are performed when the integration time is maximized whereas it makes nonuniformity compensation harder.

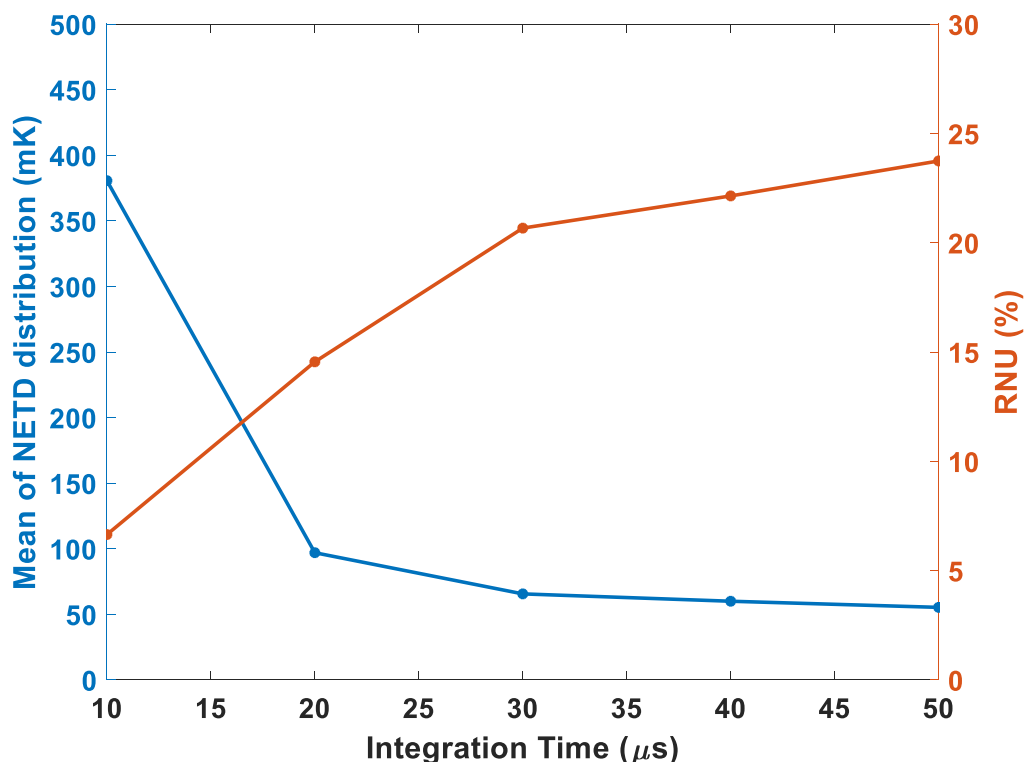


Figure 2-3: Effect of the integration time on output nonuniformity and NETD.

Detector and reference resistances vary because of process variations as seen in Figure 2-4. Since the integration time is maximized, even small resistance differences create significant output differences. To compensate the nonuniformity, two-stages DACs are implemented in the ROIC. The DAC responsible for reference resistances are applied to all FPA, in other words, one two-stage DAC is implemented to control the bias on reference resistances. The DAC which is

implemented for detector resistances has a different mechanism as the first stage of the DAC is applied to all detector resistances in the FPA and the second stage of the DAC enables the application of different biases for each pixel to compensate pixel to pixel resistance nonuniformity. In addition to these two-stages DACs, the ROIC is capable of reference selection. There are 640×12 reference resistances are produced in the process of the microbolometers and this provides 12 reference resistances for each column of the FPA. At least 4 reference resistances should be used for each column to protect the resistances from overheating. The selection can be arranged to improve the uniformity and performance of the microbolometer.

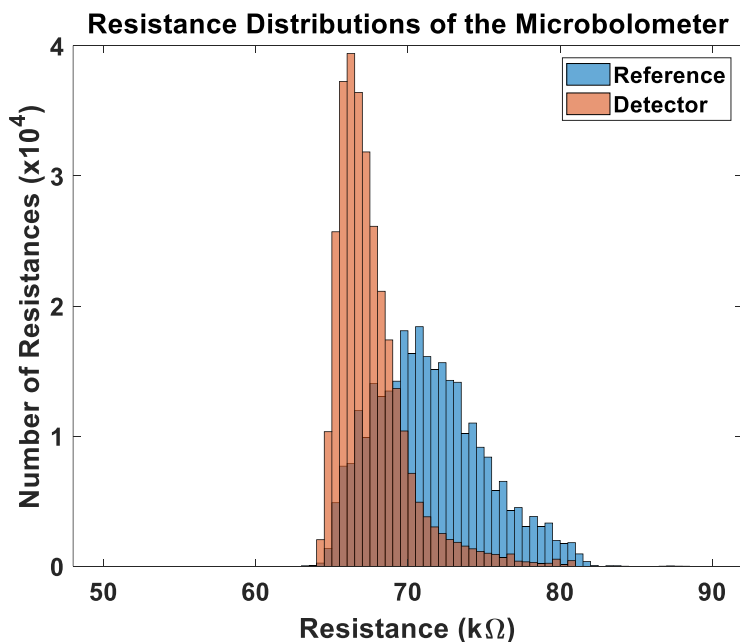


Figure 2-4: Detector and reference resistance distributions of the microbolometer at 20°C produced in METU MEMS Center.

2.1 Standard Optimization Algorithms for Bias DACs

The calibration procedure of bias voltages (NUC voltages) consists of several steps. The first step is to determine the first stage of the DAC for detector resistances regarding the detector resistance distribution and the relation between the bias and NETD. Bias should be maximized to obtain higher NETD however the resistance

differences cause a decrease in the mean of the bias values. Therefore, the first stage of the DAC should be arranged to keep detector bias as high as possible while ensuring that all pixels can be biased well in the determined bias range. After this, the second stage of the DAC for detector resistances are set to half of its maximum value for all pixels, and stages of the DAC for reference resistances should be determined to get the mean of the output histogram into the desired point which is determined as 9000 analog-to-digital unit (ADU). This step aims to make the mean value of the second stage of the DAC for detector resistances half of its maximum value and the reason for this depends on the effects of temperature change which will be explained deeply in CHAPTER 3. At this point, the obtained output distribution can be shown in Figure 2-5.

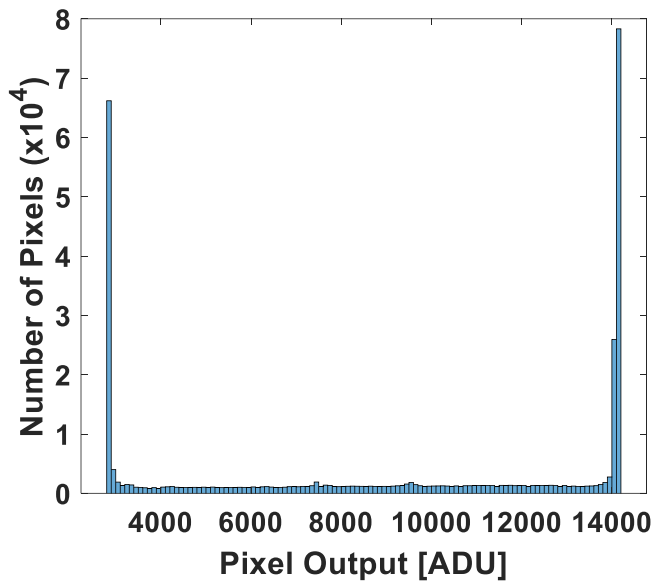


Figure 2-5: Output histogram of the microbolometer at 20 °C produced in METU MEMS Center before calibration of the second stage of DACs for detector resistances.

The microbolometer used in the work has an 8-bit DAC for the second stage of the DAC for detector resistances. The calibration procedure of the stage requires finding the optimum value for each pixel. Since it is not possible to find these points by hand, an algorithm is needed. Two conventional methods are used to find them: the sweep method and the binary search method [37].

2.1.1 Sweep Method

The sweep method depends on the idea that giving of bias values into all pixels consecutively and finding optimum values. The algorithm of the sweep method can be shown in Figure 2-6.

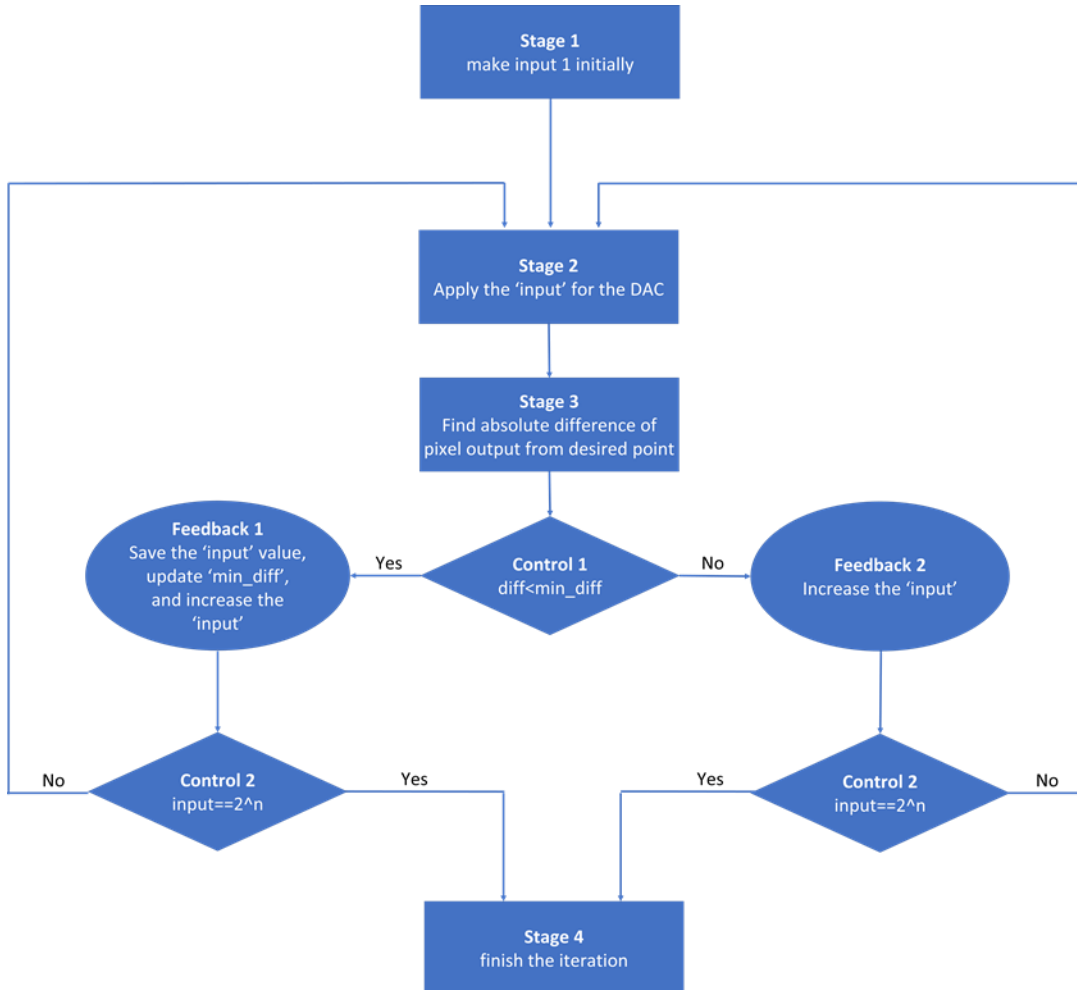


Figure 2-6: The algorithm of sweep method for a pixel in the FPA when n bit DAC is used to calibration.

All pixels are biased with the minimum DAC value initially and the bias is increased step by step until its final value [37]. During the progress, pixel outputs are observed and DAC values for each pixel where the output is closest to the desired point are saved as shown in Figure 2-7.

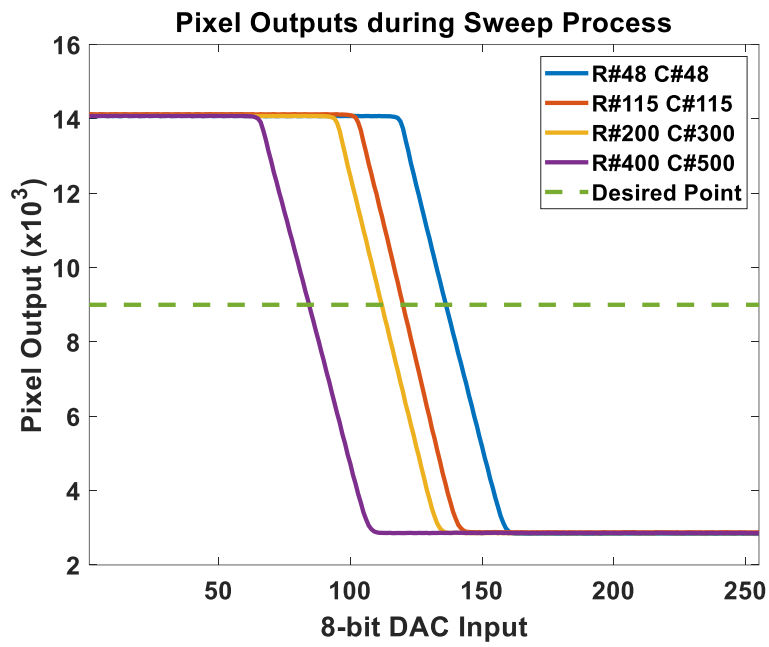


Figure 2-7: Selected pixel outputs for the microbolometer during calibration of the second stage of DACs for detector resistances with the sweep method.

The optimum points found with the sweep method are saved into the memory. After this, bias values in the memory for the pixels are applied, and new output distribution is shown in Figure 2-8.

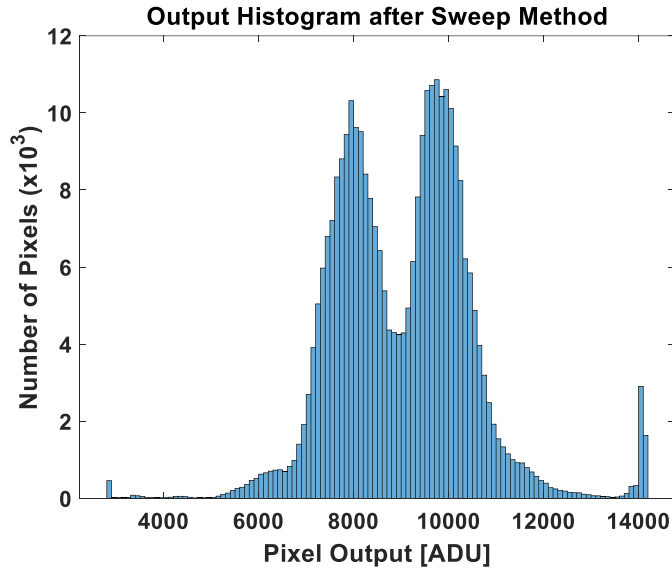


Figure 2-8: Output histogram of the microbolometer at 20 °C when the bias values are found with the sweep method.

2.1.2 Binary Search Method

The binary search methods work differently from the sweep method and it requires the ability to apply bias voltages for pixels differently at the same time. If these voltages can only be given with the help of the memory, this results in saving data into the memory for each step and this increases calibration time significantly. However, if the ROIC has capable of this, it provides lower calibration time. The algorithm of the binary search method can be shown in Figure 2-9.

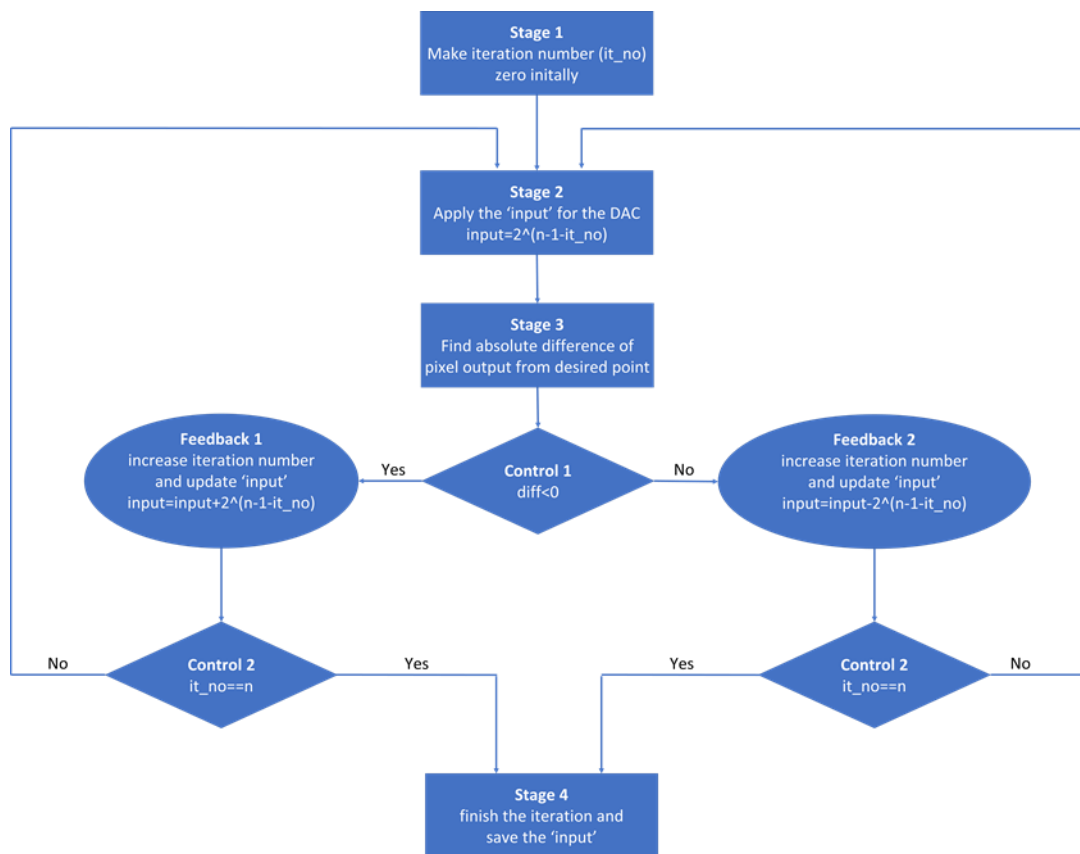


Figure 2-9: The algorithm of the binary method for a pixel in the FPA when n bit DAC is used for calibration.

All pixels are biased with half of the maximum DAC value initially. After this, output for each pixel is compared with the desired point and the DAC value for the pixel is increased or decreased as the amount of quarter of the maximum DAC value. The procedure is repeated until the last step is equal to 1 and optimum values for each

pixel are found [37]. For the microbolometer, selected pixel outputs during the calibration are shown in Figure 2-10. Moreover, output distribution is shown in Figure 2-11.

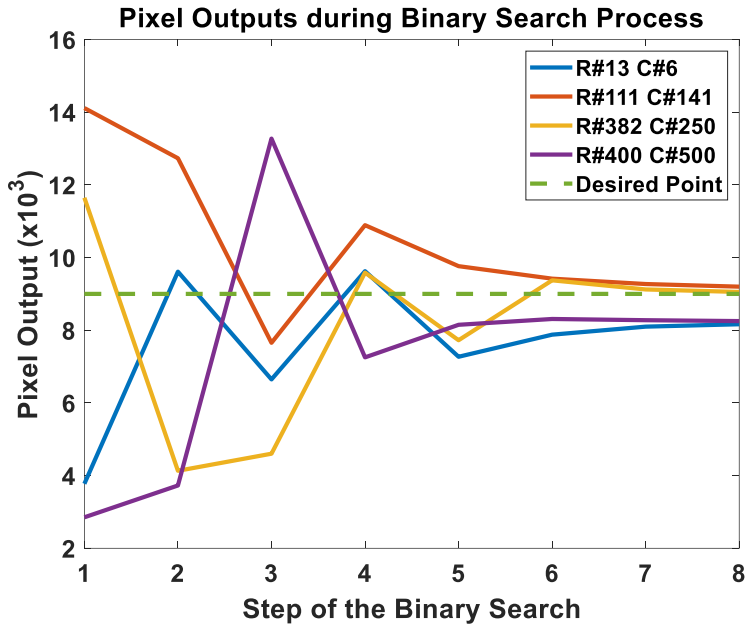


Figure 2-10: Selected pixel outputs for the microbolometer during calibration of the second stage of DACs for detector resistances with the binary search method.

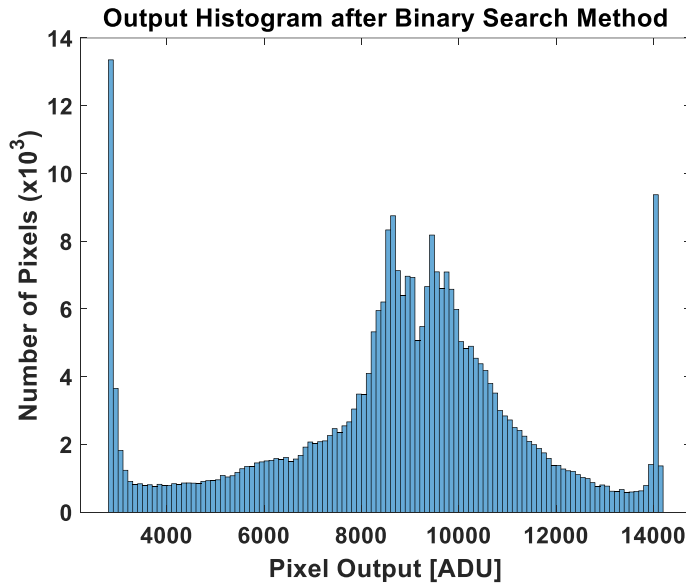


Figure 2-11: Output histogram of the microbolometer at 20 °C when the bias values are found with the binary search method.

2.2 Pixel Interactions

The sweep and binary search methods do not give the same output histogram due to differences in these algorithms. RNU values and saturated pixel ratios are used to compare the quality of these methods as seen in Table 2-1. Although the binary search method requires lower calibration time, the sweep method generally provides a smaller number of saturated pixels.

Table 2-1: Comparison of the sweep and binary search methods for the microbolometer in terms of RNU and saturated pixel ratio.

Microbolometer ID	RNU (%)		Saturated Pixel (%)	
	Sweep	Binary	Sweep	Binary
Sample 1	12.50	19.01	2.44	15.81

There are some pixels for which optimum bias value could not be found properly regardless of the used algorithm. To understand the reason for this, four of these pixels are selected and outputs of them obtained with sweep method are compared to one when all pixels are biased with calculated value for the pixel by using sweep method as seen in Figure 2-12.

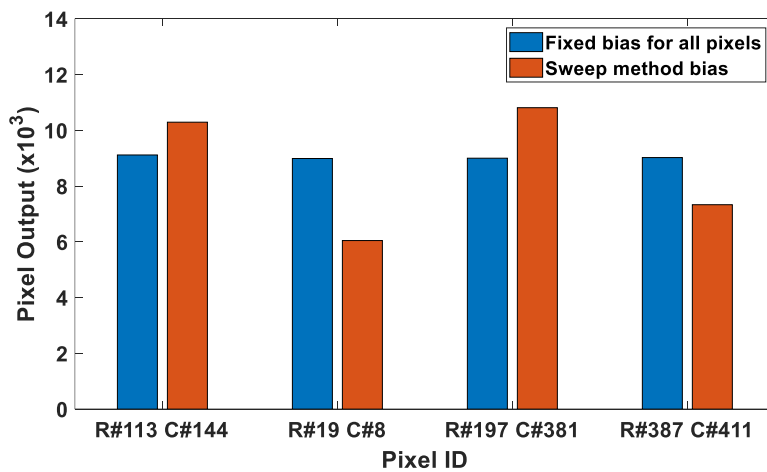


Figure 2-12: Outputs of selected pixels obtained with sweep method and the case when all pixels are biased with calculated value for the pixel by using the sweep method for the microbolometer.

The output of a pixel becomes different when the bias values of other pixels are changed although the bias value of the pixel is the same. There can be two reasons for this: the interaction between outputs or inputs. To understand this, an experiment is performed: Cavity blackbody is placed in front of the Dewar and its temperature is set two different values when inputs of the pixels are the same. Obtained frames for these cases are analyzed and differences between these frames are found as seen in Figure 2-13.

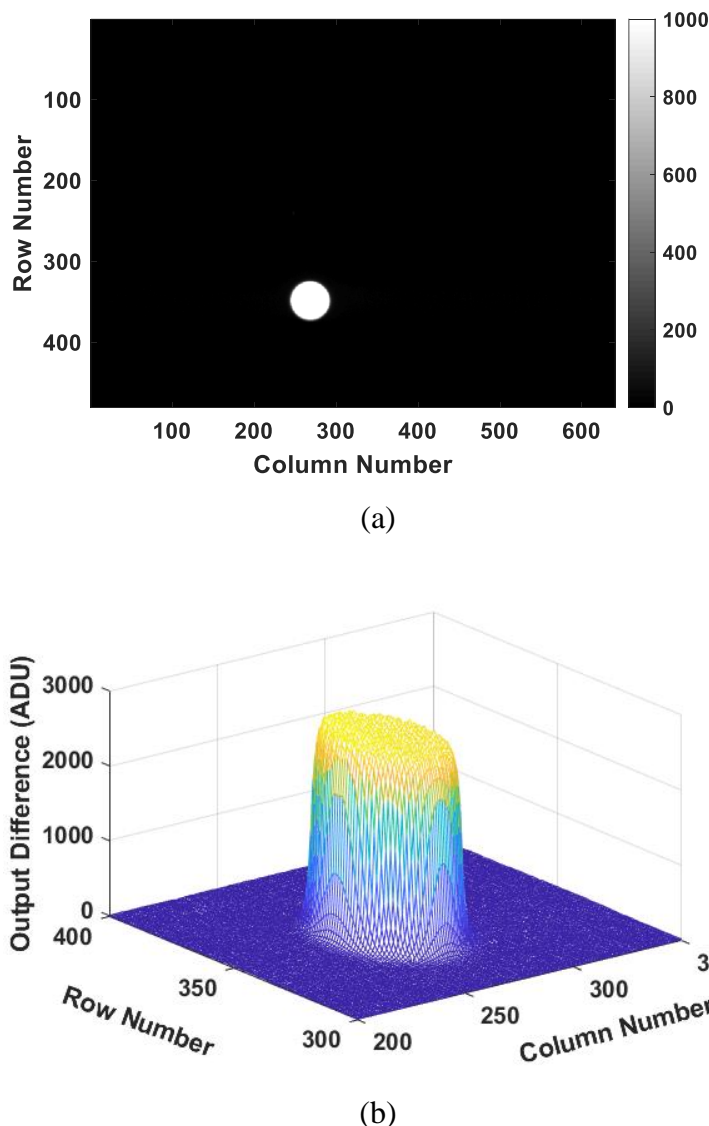


Figure 2-13: (a) Grayscale image for the differences between two different cavity blackbody temperatures and (b) detailed 3D demonstration for the region of interest.

The increase in the cavity blackbody temperature is only shown in pixels that are exposed to the illumination and there are no shadow or ghosting effects in the remaining pixels. This indicates that there are interactions only between bias values of the pixels. They can be investigated into two categories: inside row interaction and row-to-row interaction.

2.2.1 Inside Row Interaction

Pixels in a row are biased at the same time; however, the bias values for these pixels are determined by data in the memory thanks to the DACs. They are designed to share resistance string for efficiency in the layout which is one of the critical issues for large format microbolometers. For this reason, these DACs can face many problems such as the parallel resistor effect and wire resistance effect [61]. An experiment is done to understand whether there is an interaction between pixels in a row. In the experiment, initially, bias values are found with sweep method, labeled as original sweep method case, and the calculated values for the 160 pixels of the selected row, which are located at the middle of the row, are increased as the same amount, labeled as manipulated sweep method case. After this, these two arrays which contain input data for the DAC are used to obtain dark images at the same conditions. Differences between the pixels of the selected for these two cases are analyzed as seen in Figure 2-14.

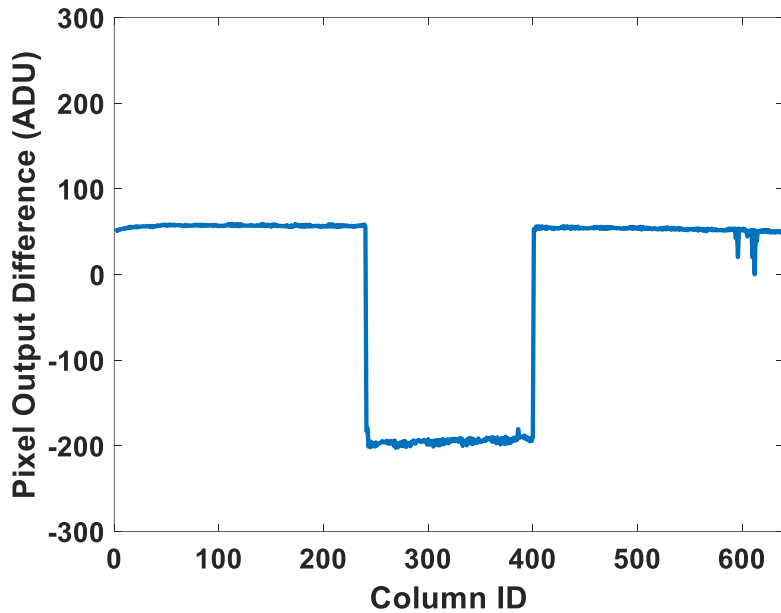


Figure 2-14: Pixel output differences of the selected row for original sweep method and manipulated case.

Outputs of the middle 160 pixels changes due to manipulation in the DAC data; however, output differences are seen for other pixels in the row whereas DAC data for these pixels are the same. The results indicate the interaction between pixels in a row. To model the interaction, a different number of pixels (10, 160, 320, 640) for which the DAC data in the memory is manipulated is used. Manipulated pixels in the row can be listed as:

- 10 Pixels → from column 316 to column 325
- 160 Pixels → from column 241 to column 400
- 320 Pixels → from column 161 to column 480
- 640 Pixels → entire row

Outputs of the pixels for each of these cases are subtracted from the original case (the sweep method) as seen in Figure 2-15.

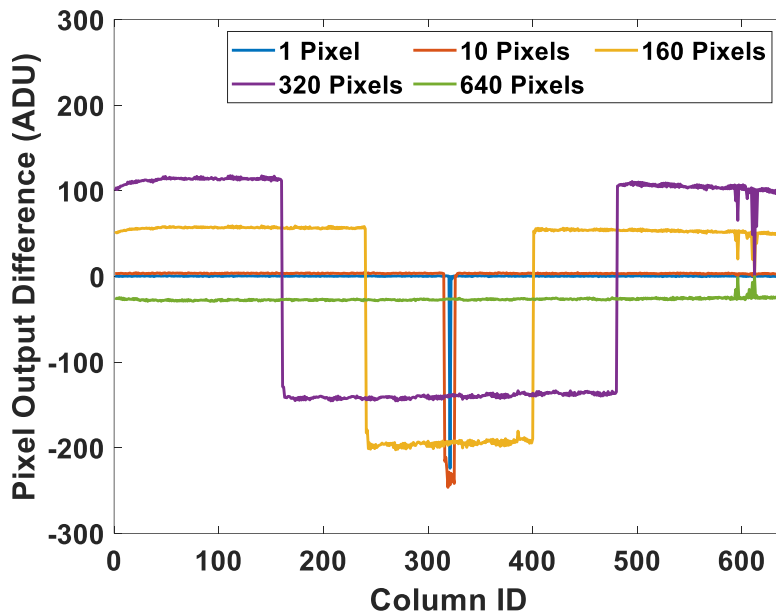


Figure 2-15: Pixel output differences of the selected row for the original case and manipulated cases which have a different number of manipulated pixels.

It is seen that a higher number of manipulated pixels in a row result in higher output changes for the pixels which protect the DAC value in all cases and the relation can be seen easily in Figure 2-16.

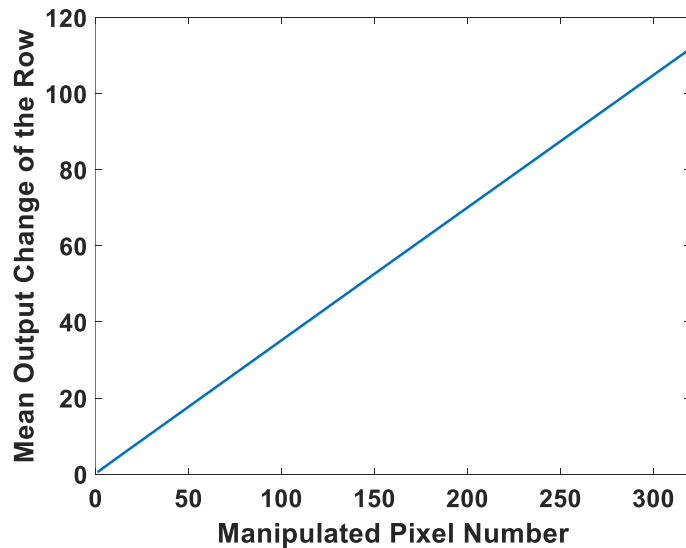


Figure 2-16: Output differences of the pixels which have constant DAC value for the number of manipulated pixels in the row.

There is a linear relationship between the number of manipulated pixels in a row and output changes of the protected pixels. When the bias value for a pixel is increased, the load resistances of the DAC alters. Since all of the fine DACs are identical, it is expected that the interaction is linear with the number of manipulated pixels.

2.2.2 Row-to-Row Interaction

The readout system of the ROIC works in rolling line type, which means that all pixels in a row are integrated at the same time during integration time and the next row is biased and integrated [12] [62]. The procedure is continued until the pixels in the last row in the FPA are integrated. This structure is used since it provides larger charge storage although it decreases the integration duration. During the consecutive procedure, pixels may affect each other.

An experiment is performed to observe the effects of pixels in a different row. DAC values for a row are increased intentionally and obtained outputs are subtracted from the one which is obtained by using the sweep method. The difference can be seen easily by using a colored image map as shown in Figure 2-17.

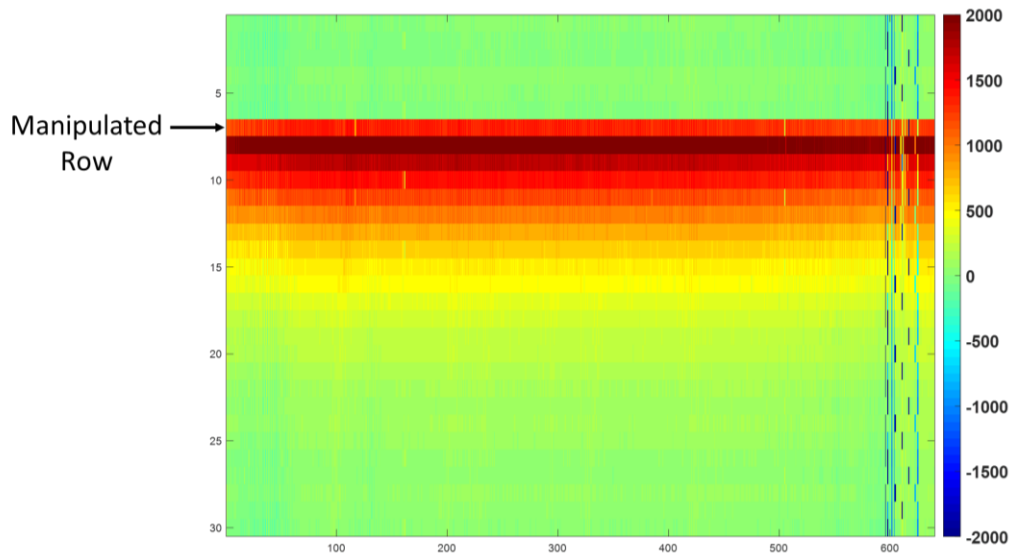


Figure 2-17: Colored image map of output differences between the manipulated and original case in terms of ADU.

Pixels in the next rows of the manipulated row are affected strongly whereas the DAC values for them are the same for these cases. Moreover, the effect decreases with the distance from the manipulated row. Mean values of output histograms for these next rows are plotted to see the decrease in the effect as shown in Figure 2-18.

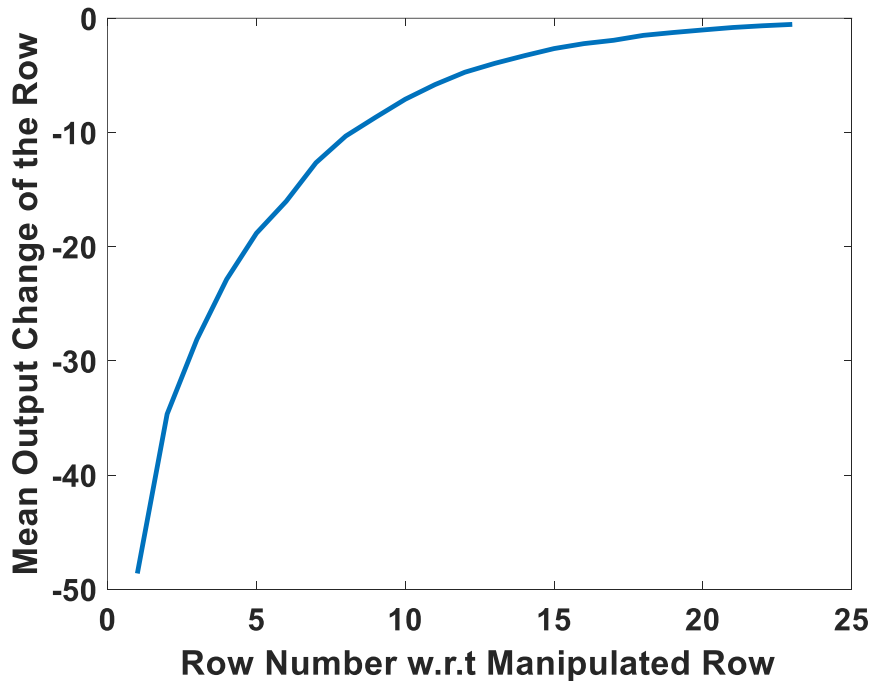


Figure 2-18: Mean values of output change for the next rows of the manipulated row in terms of ADU.

It is seen that there is no effect of manipulation in a row on the previous rows. To ensure this, an extreme condition is created: all pixels in the half of the FPA (from row 241 to row 480) are saturated and pixel outputs in row 240 are observed as shown in Figure 2-19.

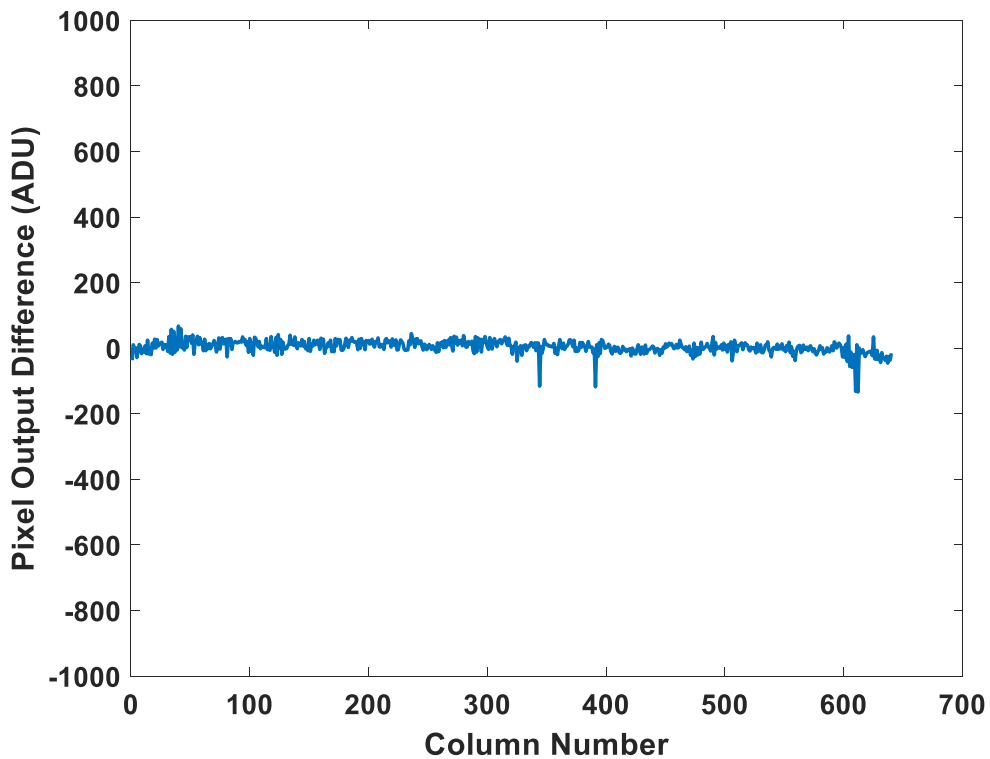


Figure 2-19: Change in the pixel outputs of row 240 when the pixels from row 241 to row 480 are saturated intentionally.

Rows are affected by only the previous rows as expected due to the rolling type system. The effect decreases exponentially and this shows that the reason for the interaction depends on the capacitive transient characteristics of the biases. When the bias value for a pixel is changed, the output of the DAC exhibits capacitive transient behavior due to capacitances in the switches and the buffers. The system passes to the next row although the input of the DAC is not settled down and this causes the interaction between the rows. To solve the problem, number of fine DACs in the system can be increased and lower input capacitances can be obtained. However, this causes increase in the layout area although the main advantage of the two-stage DACs is smaller layout area. For this reason, high number of fine DACs is not desirable in order to protect the advantage of two-stage DACs.

2.3 Interacted NUC Voltage Algorithm

Conventional methods to find NUC voltages do not consider interactions between pixels in the ROIC. However, these interactions become significant when the array size of microbolometers are increased and high-speed imaging systems are developed. For these reasons, a method that includes the interactions is proposed. The proposed method requires modeling of the inside row interactions and row-to-row interactions. Moreover, output change against one step of the DAC for all pixels, which can be defined as the output step, should be found.

Inside row interactions, explained in section 2.2.1, are modeled as linear. The data is fitted into the linear equation and coefficients for the equations are found as seen in Figure 2-20.

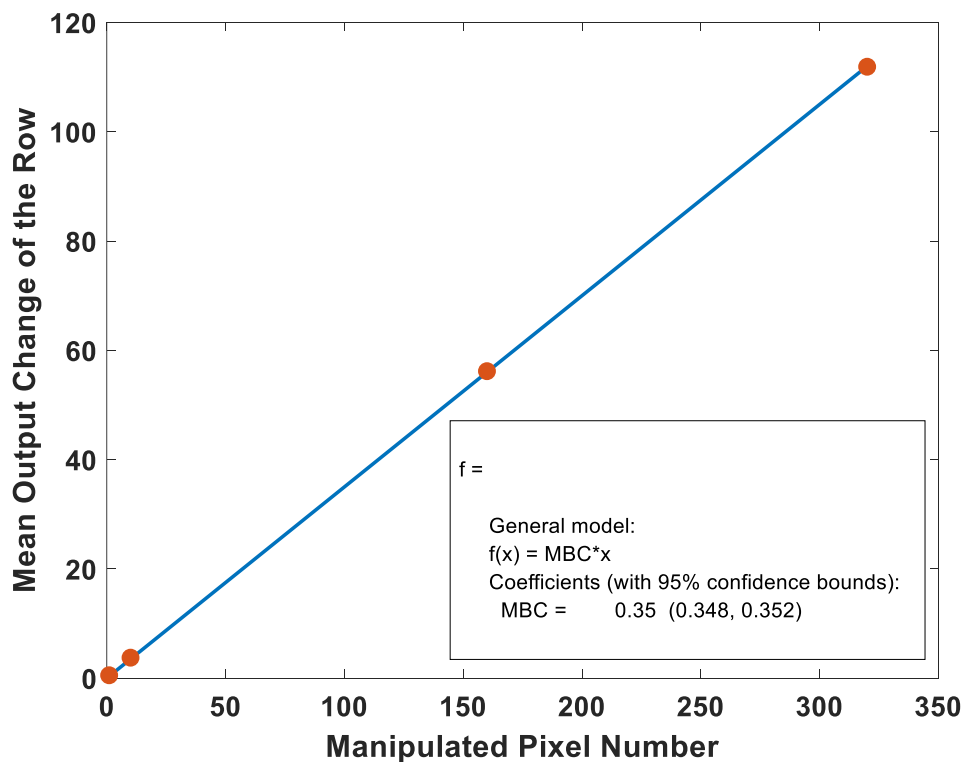


Figure 2-20: Linear regression for inside row interactions of the microbolometer.

Row-to-row interactions can be fitted into the exponential equation due to capacitive behavior, explained in section 2.2.2. The coefficients for the fit are found and can be labeled as a mean-based row-to-row coefficient (MBC_{rtr}), and capacitive coefficient (CC) as demonstrated in Figure 2-21.

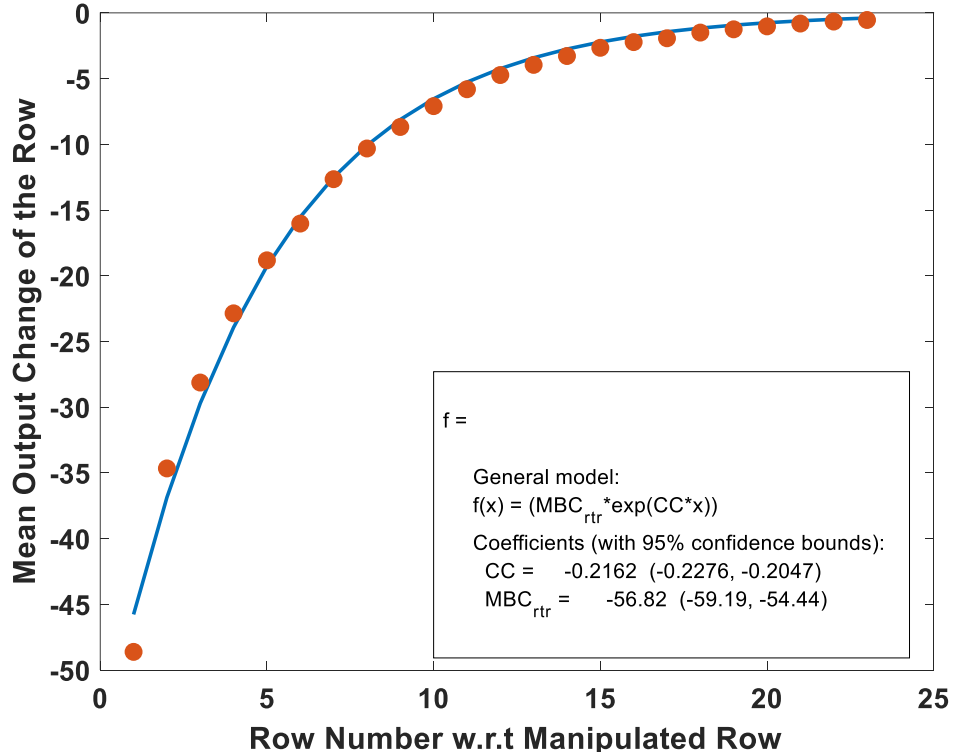


Figure 2-21: Exponential fit for row-to-row interactions of the microbolometer.

The output step can be calculated by using the sweep method. For this reason, in the proposed method, the sweep method is applied and outputs for each pixel are fitted into the linear equation after filtering the data in the saturated region as seen in Figure 2-22. The slope of the linear equation provides the output step for the pixel.

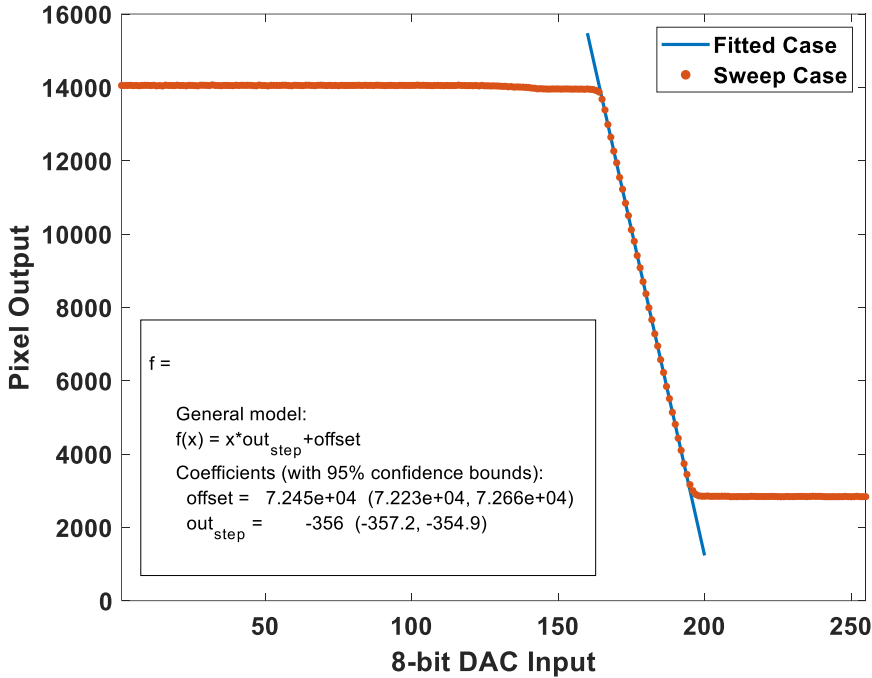


Figure 2-22: Linear fit for output of a pixel for the input of the DAC during sweep method for the microbolometer.

The output step depends on the detector resistance value of the pixel. Therefore, pixel coefficients, shortly PC, are found by normalizing the output step values of the pixels as seen below to estimate pixel output changes when the interactions are included in the calculations:

$$PC_{i,j} = \left(\frac{out_step_{i,j}}{\frac{1}{m * n} \sum_{i=1}^m \sum_{j=1}^n out_step_{i,j}} \right) \quad (2.1)$$

where m and n are the number of rows and columns respectively, $out_step_{i,j}$ shows the output step for the pixel, and $PC_{i,j}$ is the pixel coefficient.

The proposed method depends on the update of NUC voltages calculated with the sweep method by considering inside row and row-to-row interactions. Due to the effects of the rolling line system, NUC voltages are updated row by row sequentially and the general working mechanism of the proposed algorithm can be demonstrated as shown in Figure 2-23.

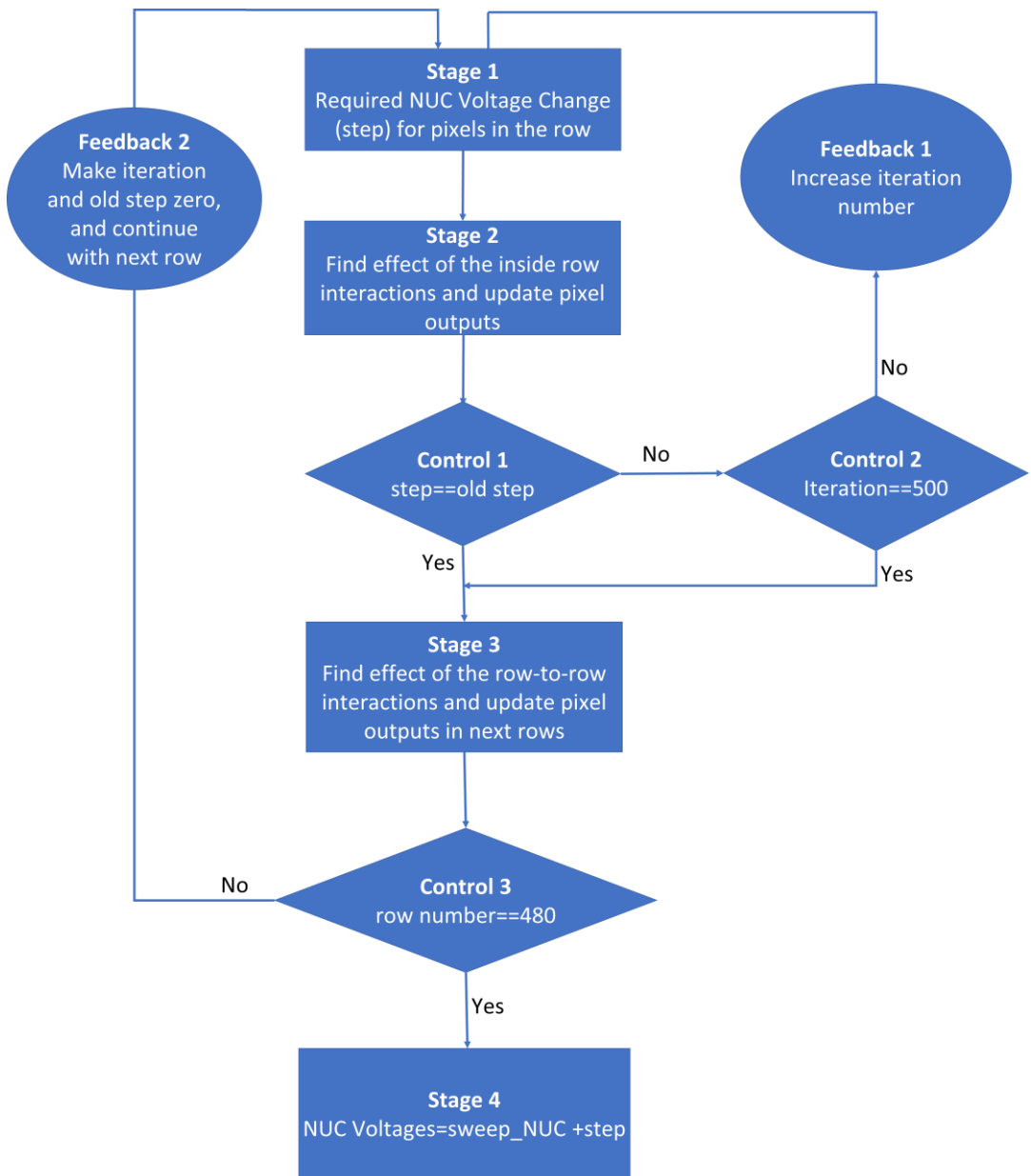


Figure 2-23: Flowchart of the proposed algorithm for NUC voltages of the microbolometer.

The proposed algorithm consists of several steps and it can be explained as:

- Stage 1: Required NUC voltage change (step) to get the output into the desired point is calculated for each pixel in the row by using output steps calculated from the data obtained with the sweep method, which is *out_step*.

After this, calculated values are rounded and the step vector for the row is found. It can be expressed as:

$$dummy_step_{i,j} = round\left(\frac{Y_{desired} - Y'_{i,j}}{out_step_{i,j}}\right) \quad (2.2)$$

$$step_{i,j} = step_{i,j} + dummy_step_{i,j} \quad (2.3)$$

where i and j are row and column number, $out_step_{i,j}$ shows the output step for the pixel, $Y'_{i,j}$ indicates the output of the pixel, $Y_{desired}$ is desired pixel output, $dummy_step_{i,j}$ is the step for the iteration, and $step_{i,j}$ is the total step for all iterations of the row. It is important to state that $step_{i,j}$ is equal to zero and $Y'_{i,j}$ is equal to pixel output after the sweep method initially which is updated for each iteration of the algorithm as seen below:

$$Y'_{i,j} = Y'_{i,j} + dummy_step_{i,j} * out_step_{i,j} \quad (2.4)$$

- Stage 2: Effects of inside row interactions are estimated by using the data obtained from the fit equation seen in Figure 2-20. The slope of the linear fit is defined as “mean based change”, shortly MBC , and used to estimate changes in pixel outputs:

$$Y'_{i,j} = Y'_{i,j} + MBC * step_{i,j} * PC_{i,j} \quad (2.5)$$

where $PC_{i,j}$ is the pixel coefficient for the pixel. These calculations are done for each pixel in the row.

- Control 1: The control mechanism aims to understand whether the optimum values for pixels in the row are found. If the $dummy_step$ is equal to 0 for all pixels in the row, this means that there is no need to continue the calculations for the row.

- Control 2: It controls whether the iteration number for the row reaches 500. Changes in the NUC voltages of some pixels cause output variation for other pixels in the row which has a dummy step value as 0 for the iteration. After this iteration, dummy steps of these pixels can be different from 0 and this affects the pixels in which there is a change in dummy step values. The situation can cause an infinite loop in the algorithm; therefore, calculations for the row is stopped when the iteration number reaches 500.
- Feedback 1: If the number of iterations is lower than 500 and dummy steps of all pixels in the row are not 0, the iteration number is increased and the calculation continues.
- Stage 3: Effects of row-to-row interactions are found with the help of the data in Figure 2-21. The effect appears through 23 rows and then it becomes negligible. Pixel outputs in these rows are updated by estimating changes in the outputs with the exponential fit equation as seen below:

$$Y'_{i+k,j} = Y'_{i+k,j} + MBC_{rtr} * e^{-CC} * step_{i,j} * PC_{i,j} \quad (2.6)$$

where $Y'_{i+k,j}$ is the pixel output at the $(i + k)^{th}$ row and $(j)^{th}$ column, MBC_{rtr} indicates mean based row-to-row coefficient, and CC is the capacitive coefficient. The value of k changes from 1 to 23 to determine the affected row number and calculate the effect of row-to-row interactions. These calculations are performed for each pixel in the row.

- Control 3: It is used to understand whether NUC voltages of all pixels in the FPA are calculated.
- Feedback 2: If there are still pixels for which NUC voltages should be calculated, it increases the row number and gets some parameters such as iteration number and dummy step into the initial conditions.
- Stage 4: It is the final stage and the calculated step array shows the values that should be added to the NUC voltages calculated with the sweep method (NUC_{sweep}) as seen below:

$$NUC_{interacted} = NUC_{sweep} + step \quad (2.7)$$

where $NUC_{interacted}$ is the final NUC voltages obtained with the proposed method, *interacted NUC voltage algorithm*.

Inputs of the DACs are set to values found with the proposed algorithm and after this, output distribution for the microbolometer is compared with the conventional methods as seen in Figure 2-24.

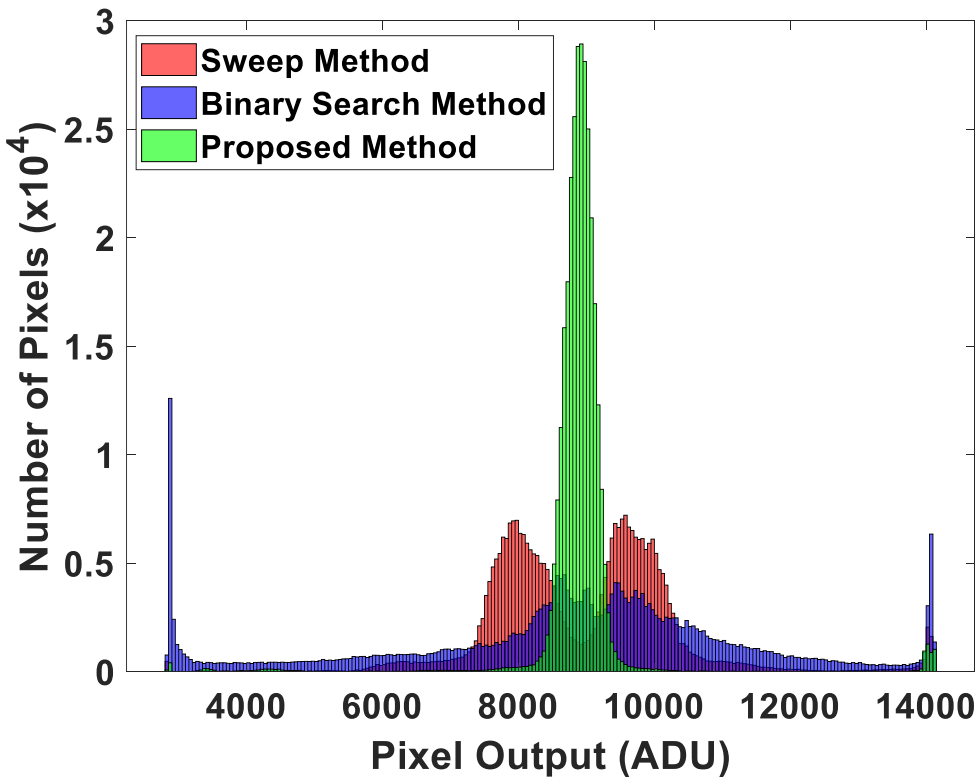


Figure 2-24: Output histogram comparison for the microbolometer obtained with conventional methods and the proposed algorithm.

The proposed algorithm improves uniformity significantly when compared to conventional methods. This shows that the effects of the interactions are estimated well; however, there are inevitable errors during these estimations. For this reason, it is possible to obtain higher uniformity by applying the algorithm more than once. Since all coefficients related to the interactions are known, it is enough to collect

outputs and apply the algorithm again easily. Change in the RNU for the microbolometer can be seen in Table 2-2 when the algorithm is applied more than once and the related histograms are shown in Figure 2-25.

Table 2-2: RNU values of the microbolometer for the number of the proposed algorithm repeated.

Case	First Iteration	Second Iteration	Third Iteration
RNU (%)	4.01	2.10	1.80

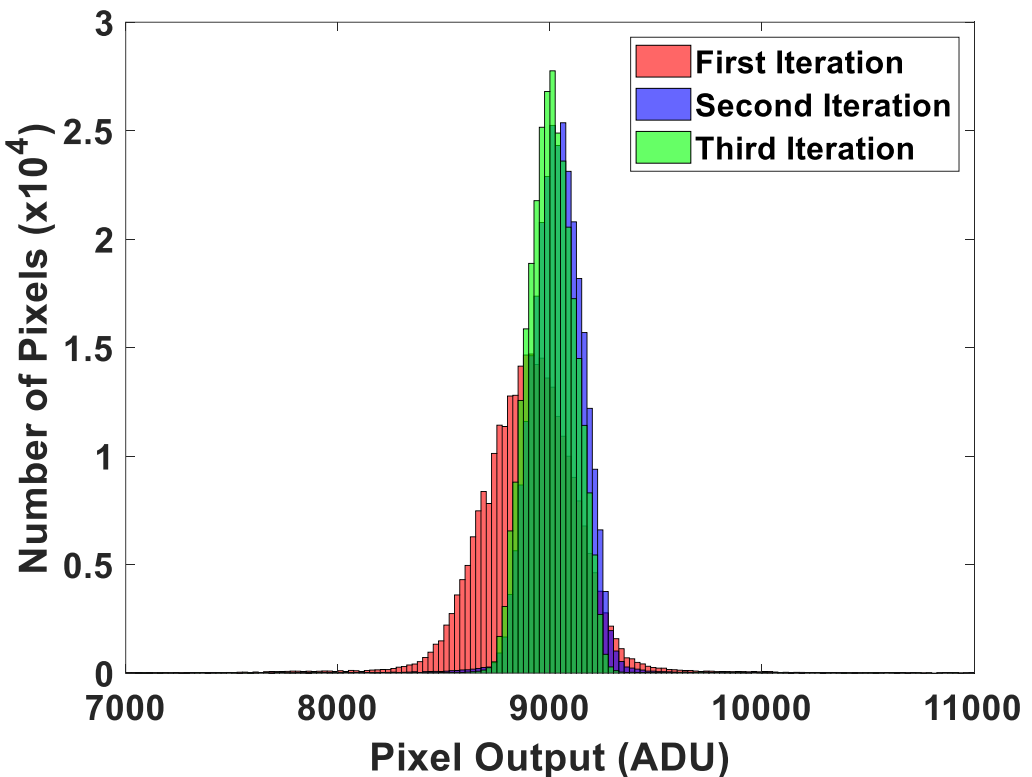


Figure 2-25: Output histogram of the microbolometer for the number of the proposed algorithm repeated.

Coefficients of the proposed algorithm are found with several experiments and this increases the calibration time considerably. To solve this issue, a method is developed and it can be explained step by step as:

1. The sweep method is applied to the microbolometer and outputs are observed. Data obtained during the progress, are used to calculate output steps of the pixels and pixel coefficients (PC).
2. One manipulated NUC voltage array is created by using the array found with the sweep method. In the manipulated array, the values of middle 160 pixels for a row is increased the determined amount (partial manipulation) and the values for a different row is also increased the determined amount (entire manipulation). The array is written into the memory and outputs are collected. It is important to notice that there should be at least 24 rows between the row of partial manipulation and the entire manipulation.
3. Outputs obtained from these two cases are compared to each other. After this, partial manipulation is used to calculate MBC and entire manipulation enables to find MBC_{rtr} and CC .
4. Coefficients found in step 3 are used to calculate final NUC voltages.

The method provides to find all coefficients by combining the experiments and calculate $NUC_{interacted}$ with one single manipulation. Thanks to this, the calibration time decreases significantly compared to the previous calibration.

The proposed algorithm is applied to additional five microbolometers by using the method as explained above to observe the reliability of the algorithm. The results are compared with the conventional methods in terms of RNU and saturated pixel ratios as seen in Table 2-3.

Table 2-3: Comparison of RNU values and saturated pixel ratios for five different microbolometers which are calibrated with the conventional methods and the proposed algorithm when the temperature of the microbolometer is 20 °C.

Die ID	Case of the NUC	Saturated Pixel Ratio (%)	RNU (%)
1	Sweep	1.41	6.33
	<i>Binary Search</i>	1.80	6.21
	<i>Interacted</i>	0.71	4.91
<hr/>			
2	Sweep	1.40	8.47
	<i>Binary Search</i>	3.16	8.13
	<i>Interacted</i>	0.77	3.67
<hr/>			
3	Sweep	1.92	8.99
	<i>Binary Search</i>	2.65	7.16
	<i>Interacted</i>	1.14	3.67
<hr/>			
4	Sweep	11.03	14.44
	<i>Binary Search</i>	9.43	10.51
	<i>Interacted</i>	1.38	5.18
<hr/>			
5	Sweep	2.23	9.02
	<i>Binary Search</i>	1.82	7.67
	<i>Interacted</i>	1.40	5.31

The proposed algorithm provides high uniformity which increases the operational temperature range and scene dynamic range of the microbolometer. During the experiments, RNU values are decreased lower than half of the ones obtained with conventional methods for all of these microbolometers. The main drawback of the proposed algorithm is the requirement of more time for the calibration; however, it will be done for each microbolometer externally and saved into the memory for real-time applications. Moreover, the calibration time will be decreased much more when the effects of the temperature are included in the calibrations which will be explained in CHAPTER 3 deeply.

2.4 Software-Based Correction

NUC voltages are inadequate to make all pixel outputs the same due to the nature of the DACs, quantization error. Therefore, more improvement is needed and this can be done with software-based correction. 2-point correction, as explained in section 1.5, is used in the work. 2-point correction includes the compensation of response nonuniformity (gain) and dark output differences (offset) by assuming the responsibility of the pixels are linear with temperature. The response of the microbolometer is observed experimentally as seen in Figure 2-26.

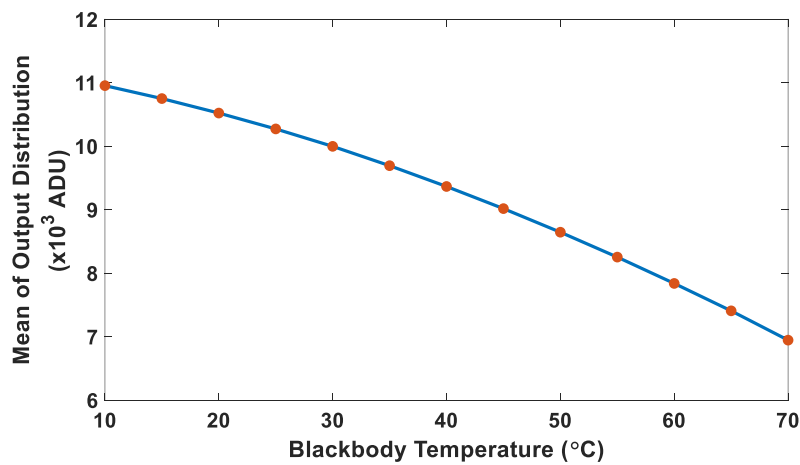


Figure 2-26: Mean of the output distribution for the microbolometer against the temperature of the blackbody.

The linear assumption for the microbolometer causes error in real response estimation yielding output nonuniformity due to characteristics of the microbolometer structures since the relation between incoming infrared illumination and temperature of the object is not linear and depends on Planck's Law. For this reason, scene dynamic range should be determined and two points should be chosen to keep output nonuniformity lower than a certain point in the scene dynamic range. Scene dynamic range is determined as between 10 °C and 70 °C for the work. It can be increased with the use of lower bias values for the resistance; however, this results in performance degradation for the microbolometer. In the determined range, output images are saved with 5 °C interval and 2-point corrections are applied to these images by using different two calibration points to observe output nonuniformity as seen in Figure 2-27.

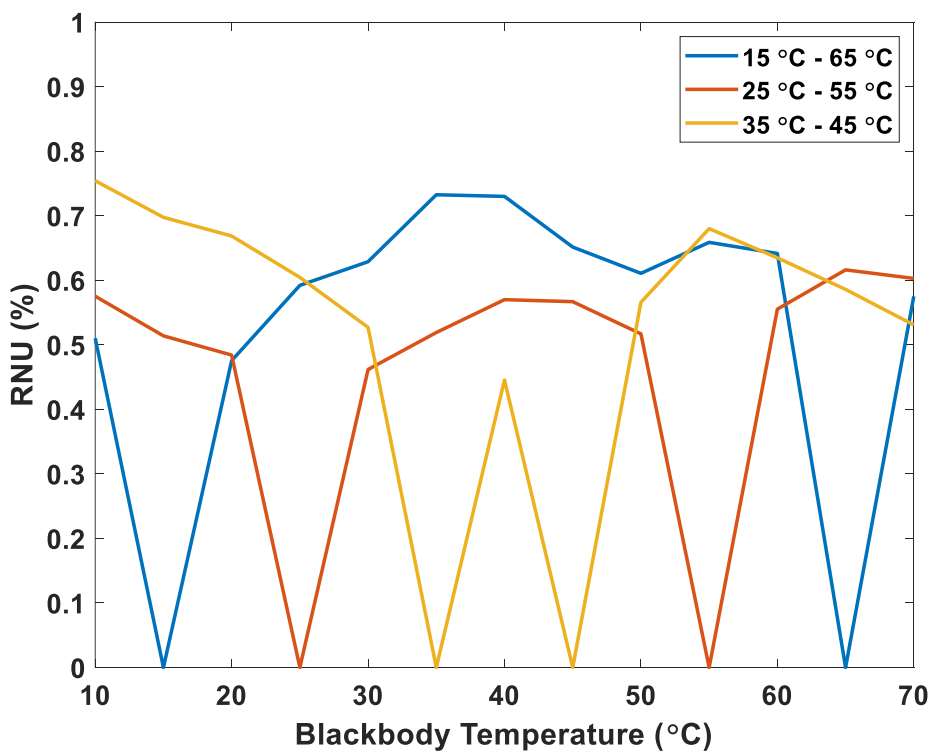


Figure 2-27: Output nonuniformity of the microbolometer in selected scene dynamic range (between 10 °C and 70 °C) after 2-point correction is applied by using different two calibration points.

The effect of nonlinear characteristics of the microbolometer is seen clearly from the output nonuniformity values. In other words, there are significant differences in the nonuniformity values the calibration and remaining points. However, for the sake of the simplicity of the algorithm, 2-point correction is preferred and the calibration points are selected as 25 °C and 55 °C by considering the nonuniformity behavior against scene temperature.

CHAPTER 3

COMPENSATION OF TEMPERATURE EFFECTS

Microbolometer structures are highly sensitive to the temperature of the detector due to the significant dependency of the active material on the temperature. Variations in ambient temperature causes change in the detector temperature which affects resistances in the microbolometer structure. Since the output of the microbolometer pixels depends on the voltages and resistances, pixel outputs diverge from the desired point due to detector temperature variations. This results in higher nonuniformity for output distribution yielding a lower scene dynamic range. Moreover, it is possible to make all pixel outputs saturated, and therefore, meaningful thermal images could not be obtained.

Microbolometer pixel output under constant bias values can be expressed for different temperatures as:

$$I_{out}(T_1) = I_{det}(T_1) - I_{ref}(T_1) = \frac{V_{det}}{R_{det}(T_1)} - \frac{V_{ref}}{R_{ref}(T_1)} \quad (3.1)$$

$$I_{out}(T_2) = I_{det}(T_2) - I_{ref}(T_2) = \frac{V_{det}}{R_{det}(T_2)} - \frac{V_{ref}}{R_{ref}(T_2)} \quad (3.2)$$

where T_1 and T_2 are detector temperatures. If the TCR of the active material is constant between these temperatures, the relation between resistances can be shown as:

$$R_{det}(T_2) = R_{det}(T_1) * (1 + \alpha_{det})^{T_2 - T_1} \quad (3.3)$$

$$R_{ref}(T_2) = R_{ref}(T_1) * (1 + \alpha_{ref})^{T_2 - T_1} \quad (3.4)$$

where α_{det} and α_{ref} indicate TCR values of the detector and reference resistances in the given temperature, respectively.

TCR characteristics of active materials used in microbolometer structures depend strongly on detector temperature. For this reason, modeling of pixel outputs for detector temperature becomes more complex.

TCR values of detector and reference resistances are not the same although the same active material is used due to process variations. This causes variations in the pixel output depending on detector temperature and therefore bias voltages should be reoptimized with the temperature. However, it is not logical to update the bias values continuously since they are controlled via the DACs. For this reason, bias values should be found for each determined temperature interval.

Software-based corrections should be updated when the bias values are reoptimized for the new detector temperature due to two reasons. The first one is that pixel output with reoptimized bias value may not be the same as the previous value due to the nature of the DACs. This situation requires optimization in offset parameters of 2-point correction. The second one is related to the responsivity distributions of the pixels. Since TCR and resistance value change with the temperature, pixel response values are strongly affected by the temperature, and therefore, gain parameters of 2-point correction should be reconfigured. Moreover, new gain parameters result in the requirement of an update for offset parameters.

Small temperature variations, where detector temperature stays in the range of constant bias values, causes a change in pixel outputs. This phenomenon is called temperature drift and requires reconfiguration in software-based corrections.

Compensation of temperature effects consists of three main parts, which are also related to each other. Firstly, bias voltages should be updated and after this, software-based corrections should be reconfigured for new bias voltages. Finally, software-based corrections should also be reoptimized for small temperature changes under constant bias values, which is called temperature drift compensation.

3.1 Bias Voltage Estimation

Bias voltages control the current drawn by the detector and reference resistances and they can be arranged for resistance values as explained in CHAPTER 2. NUC voltages can be set for each pixel whereas the reference bias voltage is applied to all pixels same and can be set globally in the CTIA type ROIC. It is time-consuming to calculate the optimum bias voltages experimentally for each temperature. Moreover, the data occupy significant space in the memory. For this reason, they should be modeled and found with the minimum number of calibration points to decrease experiment time and memory size.

Pixel output characteristics for temperature should be estimated to find the optimum bias voltages. TCR is kept constant and the compensation depends on only the NUC voltages to model pixel output initially, in other words, reference bias voltages stay the same for all temperatures. The known equations can be shown for temperature T1 and T2 as:

$$I_{out_1} = I_{det_1} - I_{ref_1} = \frac{V_{det_1}}{R_{det_1}} - \frac{V_{ref_1}}{R_{ref_1}} \quad (3.5)$$

$$I_{out_2} = I_{det_2} - I_{ref_2} = \frac{V_{det_2}}{R_{det_2}} - \frac{V_{ref_2}}{R_{ref_2}} \quad (3.6)$$

$$R_{det_2} = R_{det_1} * (1 + \alpha_{det})^{T_2 - T_1} \quad (3.7)$$

$$R_{ref_2} = R_{ref_1} * (1 + \alpha_{ref})^{T_2 - T_1} \quad (3.8)$$

$$V_{det_2} = V_{det_1} + \Delta V \quad (3.9)$$

$$V_{ref_2} = V_{ref_1} \quad (3.10)$$

where I_{out_1} and I_{out_2} are output currents, I_{det_1} and I_{det_2} are detector currents, I_{ref_1} and I_{ref_2} are reference currents, V_{det_1} and V_{det_2} are detector bias voltages, V_{ref_1} and V_{ref_2} are reference bias voltages, R_{det_1} and R_{det_2} are detector resistances, R_{ref_1} and R_{ref_2} are reference resistances, α_{det} and α_{ref} are TCR values of the detector and reference resistances at temperatures T1 and T2, respectively. The output current should be the same for these temperatures and therefore, the equation can be written as:

$$\frac{V_{det_1}}{R_{det_1}} - \frac{V_{ref_1}}{R_{ref_1}} = \frac{V_{det_2}}{R_{det_2}} - \frac{V_{ref_2}}{R_{ref_2}} \quad (3.11)$$

$$\frac{V_{det_1}}{R_{det_1}} - \frac{V_{ref_1}}{R_{ref_1}} = \frac{V_{det_1} + \Delta V}{R_{det_1} * (1 + \alpha_{det})^{T_2 - T_1}} - \frac{V_{ref_1}}{R_{ref_1} * (1 + \alpha_{ref})^{T_2 - T_1}} \quad (3.12)$$

$$I_{det_1} * \left(1 - \frac{1}{(1 + \alpha_{det})^{T_2 - T_1}}\right) - I_{ref_1} * \left(1 - \frac{1}{(1 + \alpha_{ref})^{T_2 - T_1}}\right) - \frac{\Delta V}{R_{det_1} * (1 + \alpha_{det})^{T_2 - T_1}} = 0 \quad (3.13)$$

Since TCR values are very small compared to 1, using Taylor Series Expansion, it can be written as:

$$\frac{1}{(1 + \alpha_{det})^{T_2 - T_1}} \approx (1 - \alpha_{det})^{T_2 - T_1} \quad (3.14)$$

$$\frac{1}{(1 + \alpha_{ref})^{T_2 - T_1}} \approx (1 - \alpha_{ref})^{T_2 - T_1} \quad (3.15)$$

Using these equations, the equation can be converted as:

$$I_{det_1} * (1 - (1 - \alpha_{det})^{T_2 - T_1}) - I_{ref_1} * (1 - (1 - \alpha_{ref})^{T_2 - T_1}) - \frac{\Delta V}{R_{det_1} * (1 + \alpha_{det})^{T_2 - T_1}} = 0 \quad (3.16)$$

Since $\alpha_{det} \ll 1$, $\alpha_{ref} \ll 1$, $\alpha_{det} * (T_2 - T_1) \ll 1$ and $\alpha_{ref} * (T_2 - T_1) \ll 1$ for small temperature differences, by using Binomial approximation, some terms can be simplified as:

$$(1 - \alpha_{det})^{T_2 - T_1} \approx (1 - (T_2 - T_1) * \alpha_{det}) \quad (3.17)$$

$$(1 - \alpha_{ref})^{T_2 - T_1} \approx (1 - (T_2 - T_1) * \alpha_{ref}) \quad (3.18)$$

Due to $I_{det_1} \approx I_{ref_1} \gg I_{out_1}$, the equation can be written as:

$$\begin{aligned} (I_{det_1} * R_{det_1}) * (1 + \alpha_{det})^{T_2 - T_1} * (T_2 - T_1) * (\alpha_{det} - \alpha_{ref}) \\ = \Delta V \end{aligned} \quad (3.19)$$

Using Binomial approximation again and $(T_2 - T_1) = \Delta T$, finally it can be expressed as:

$$V_{det_1} * (1 + \Delta T * \alpha_{det}) * (\Delta T) * (\alpha_{det} - \alpha_{ref}) = \Delta V \quad (3.20)$$

The final equation shows that at least a second-order polynomial function is needed although the TCR is assumed as constant. However, the assumption is not valid for vanadium oxide type microbolometer due to the material property. The TCR behavior of a vanadium oxide type microbolometer is shown in Figure 3-1. Activation energy of the vanadium oxide is not constant with temperature. For this reason, it is not logical to fit the characteristics into the Arrhenius equation in a wide temperature range. In Figure 3-1, the resistance value is measured from 20 °C to 30 °C with 1 °C steps and TCR is calculated for each of these temperature intervals discretely.

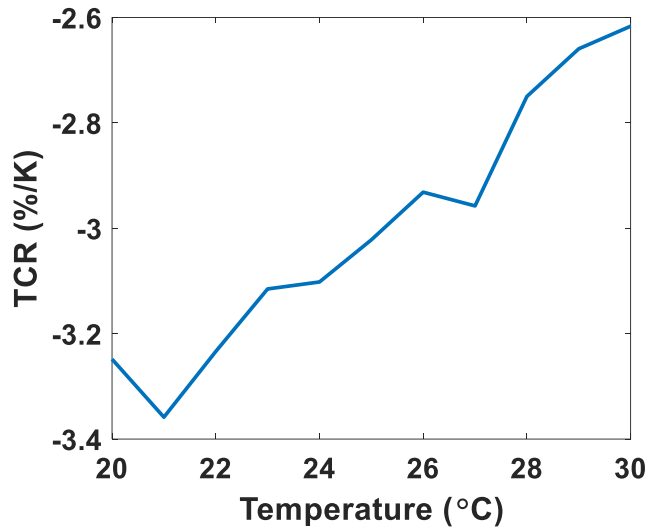


Figure 3-1: TCR characteristics of the vanadium oxide type microbolometer between the temperatures from 20 °C to 30 °C.

TCR characteristics of vanadium oxide could not be modeled exactly since it also depends on process variations such as doping qualities. To decrease error in the estimation of the TCR characteristics, it is assumed that the TCR of the material is constant for each 1 °C temperature interval. The assumption can be illustrated as seen in Figure 3-2.

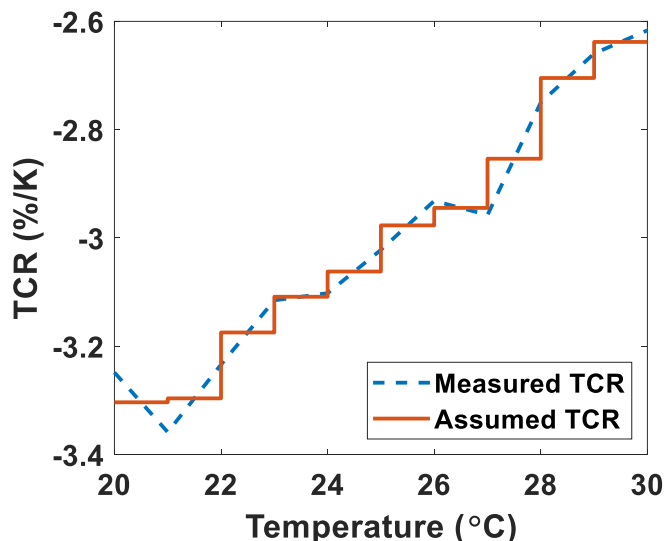


Figure 3-2: Assumed and real TCR characteristics of the vanadium oxide type microbolometer between the temperatures from 20 °C to 30 °C.

The modeled TCR characteristics enable to write of the equations below for 1 °C interval between the temperatures T1 and T2(=T1+1):

$$R_{det_2} = R_{det_1} * (1 + \alpha_{det}) \quad (3.21)$$

$$R_{ref_2} = R_{ref_1} * (1 + \alpha_{ref}) \quad (3.22)$$

These equations can be inserted into Equation (3.16), which can be written as:

$$\begin{aligned} I_{det_1} * \left(1 - \frac{1}{(1 + \alpha_{det})}\right) - I_{ref_1} * \left(1 - \frac{1}{(1 + \alpha_{ref})}\right) \\ = \frac{\Delta V}{R_{det_1} * (1 + \alpha_{det})} \end{aligned} \quad (3.23)$$

Due to $I_{det_1} \approx I_{ref_1}$, the equation can be simplified as:

$$V_{det_1} * \left(\frac{(1 + \alpha_{det})}{(1 + \alpha_{ref})} - 1\right) = \Delta V \quad (3.24)$$

Using the Taylor Series Expansion, it can be expressed as:

$$V_{det_1} * ((1 + \alpha_{det}) * (1 - \alpha_{ref}) - 1) = \Delta V \quad (3.25)$$

Because of $\alpha_{ref} * \alpha_{det} \ll \alpha_{ref}$ and $\alpha_{ref} * \alpha_{det} \ll \alpha_{det}$, the equation can be approximated as:

$$V_{det_1} * (\alpha_{det} - \alpha_{ref}) = \Delta V \quad (3.26)$$

By adding initial voltage into both sides, it is possible to find new optimum bias voltage as:

$$V_{det_1} * (1 + \alpha_{det} - \alpha_{ref}) = V_{det_2} \quad (3.27)$$

It is logical to assume the term $(1 + \alpha_{det} - \alpha_{ref})$ is constant since temperature characteristics of detector and reference resistances are similar although they are not the same. It is possible to obtain a general NUC voltage estimation equation as:

$$NUC_T * temp_coef^{\Delta T} = NUC_{T+\Delta T} \quad (3.28)$$

where ΔT shows the temperature difference, NUC_T is the NUC voltage at temperature T , $NUC_{T+\Delta T}$ indicates the NUC voltages at temperature $T + \Delta T$, and $temp_coef$ is the pixel dependent temperature coefficient which depends on TCR values of the detector and reference resistances and it can be shown as:

$$temp_coef = 1 + \alpha_{det} - \alpha_{ref} \quad (3.29)$$

The equation states that NUC voltages can be estimated by finding one unknown parameter for each pixel. The statement assumes the temperature characteristics of detector and reference resistances follow almost the same path and TCR values of the resistances are constant over 1 °C interval. To evaluate the statement, NUC voltages are found for vanadium oxide type microbolometer in the temperature range from 10 °C to 48 °C with 2 °C steps. Detector temperature is controlled via TEC and the measurement system, shown in Figure 2-2, is used again. The NUC voltages are calculated with the method proposed in CHAPTER 2. However, when the detector temperature reaches 20 °C during the experiment, it is seen that the NUC voltages of the pixels are saturated due to constant reference bias voltage as shown in Figure 3-3. The situation results in higher nonuniformity and a significant increase in dead pixel ratio.

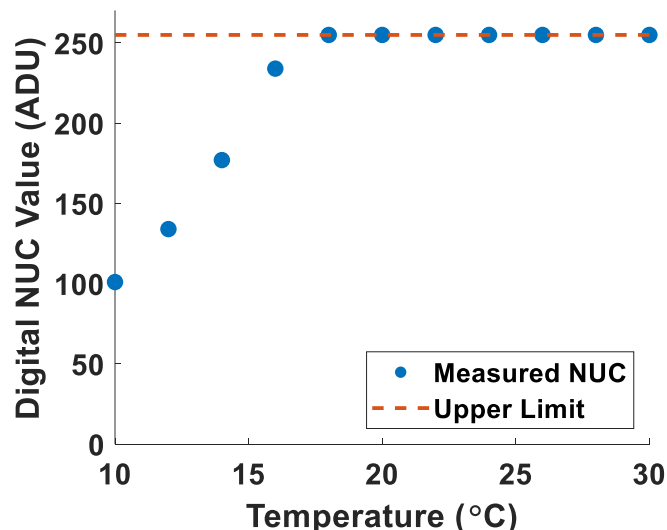


Figure 3-3: NUC values of a pixel from vanadium oxide type microbolometer for temperature.

The reference bias voltage is reoptimized for every 10 °C intervals to prevent pixels from being saturated. With the correction, NUC voltages are found in the temperature range, and obtained data are fitted into the expression for every 10 °C interval discretely as seen in Figure 3-4.

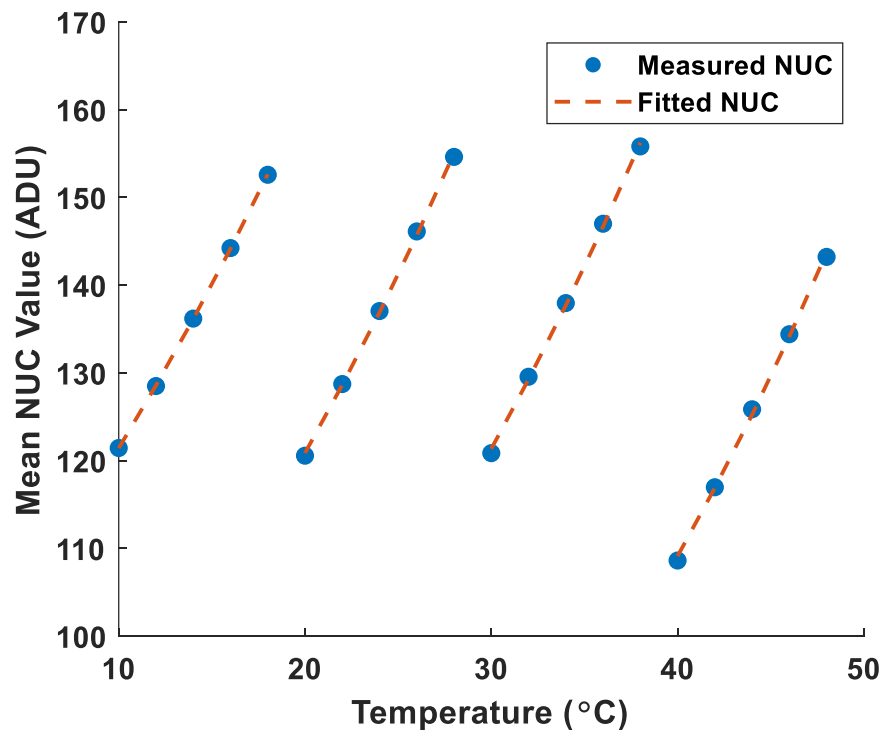


Figure 3-4: Fitted and measured mean NUC values for the vanadium oxide type microbolometer for temperature.

Temperature coefficients for the fit equations are found for each 10 °C interval as seen in Figure 3-5 and it is expected that they are close to 1 since the difference between the detector and reference TCR values should be small.

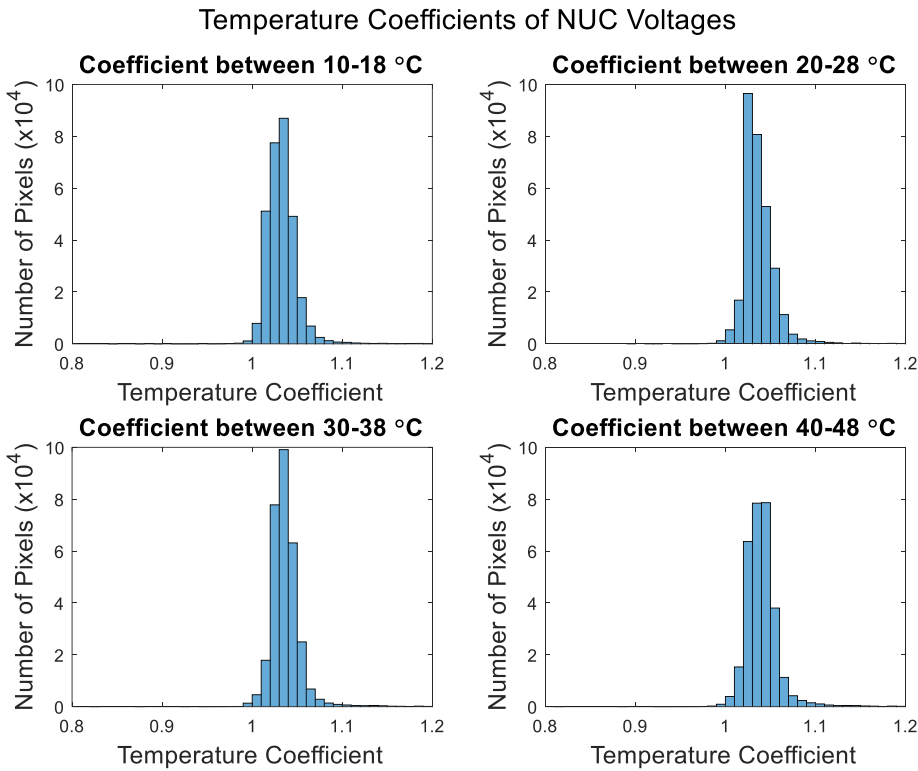


Figure 3-5: Temperature coefficients of NUC voltages for the vanadium oxide type microbolometer for each 10 °C interval from 10 °C to 48 °C.

The coefficients are higher than 1 for the microbolometer and the situation results in saturation of some pixel if the global reference bias is not reoptimized. To improve an algorithm that includes the global reference bias, it should be updated for each point where NUC voltages will be updated. At this point, optimum global reference biases at the minimum and maximum temperature values in the operational temperature range should be found and the number of steps should be calculated. It can be shown as:

$$\frac{GRB_{final} - GRB_{initial}}{resolution_{DAC} * \Delta T} = step_number \quad (3.30)$$

where GRB_{final} is the global reference bias for the final temperature, $GRB_{initial}$ is the global reference bias for the initial temperature, $resolution_{DAC}$ is the voltage value for one-step change of the DAC, ΔT is the temperature difference between initial and final temperature, and $step_number$ shows the number of steps which

the global reference bias should be updated for each temperature. The mathematical model for the NUC voltages should also be updated by including the global reference bias to control whether the fit equation is still valid. Equation (3.10) should be updated as:

$$V_{ref_2} = V_{ref_1} + \Delta V_{ref} \quad (3.31)$$

Equation (3.23) is changed as:

$$\begin{aligned} I_{det_1} * \left(1 - \frac{1}{(1 + \alpha_{det})}\right) - I_{ref_1} * \left(1 - \frac{1 + \frac{\Delta V_{ref}}{V_{ref}}}{(1 + \alpha_{ref})}\right) \\ = \frac{\Delta V_{det}}{R_{det_1} * (1 + \alpha_{det})} \end{aligned} \quad (3.32)$$

Using the relation $I_{det_1} \approx I_{ref_1}$, the equation can be written as:

$$\begin{aligned} I_{det_1} * \left(\frac{1}{(1 + \alpha_{ref})}(1 + \frac{\Delta V_{ref}}{V_{ref}}) - \frac{1}{(1 + \alpha_{det})}\right) \\ = \frac{\Delta V_{det}}{R_{det_1} * (1 + \alpha_{det})} \end{aligned} \quad (3.33)$$

Multiplying both sides with $R_{det_1} * (1 + \alpha_{det})$ and using $V_{det_2} = V_{det_1} + \Delta V_{det}$, it can be obtained as:

$$V_{det_1} * \left((1 + \alpha_{det}) * (1 - \alpha_{ref}) * (1 + \frac{\Delta V_{ref}}{V_{ref}})\right) = V_{det_2} \quad (3.34)$$

Using the relation $(1 + \alpha_{det}) * (1 - \alpha_{ref}) \approx 1 + \alpha_{det} - \alpha_{ref}$, it can be found as:

$$V_{det_1} * \left((1 + \alpha_{det} - \alpha_{ref}) * (1 + \frac{\Delta V_{ref}}{V_{ref}})\right) = V_{det_2} \quad (3.35)$$

It is seen that Equation 3.27 can be still used for the fit of NUC voltages, however, the temperature coefficients are changed as:

$$temp_coef = (1 + \alpha_{det} - \alpha_{ref}) * (1 + \frac{\Delta V_{ref}}{V_{ref}}) \quad (3.36)$$

The equation states that global reference bias can be used to make the temperature coefficients closer to 1 which prevents the pixels from being saturated. To check the statement, the procedure is applied to the microbolometer and step number is found as:

$$\frac{0.914951 - 0.747906}{0.0038 * 38} = 1.12 \xrightarrow{\text{round}} \text{step number} = 1 \quad (3.37)$$

The NUC voltages for the microbolometer are found again by updating the global reference bias at each point. The NUC voltages are fitted into the equation for each pixel and the mean NUC change is shown in Figure 3-6.

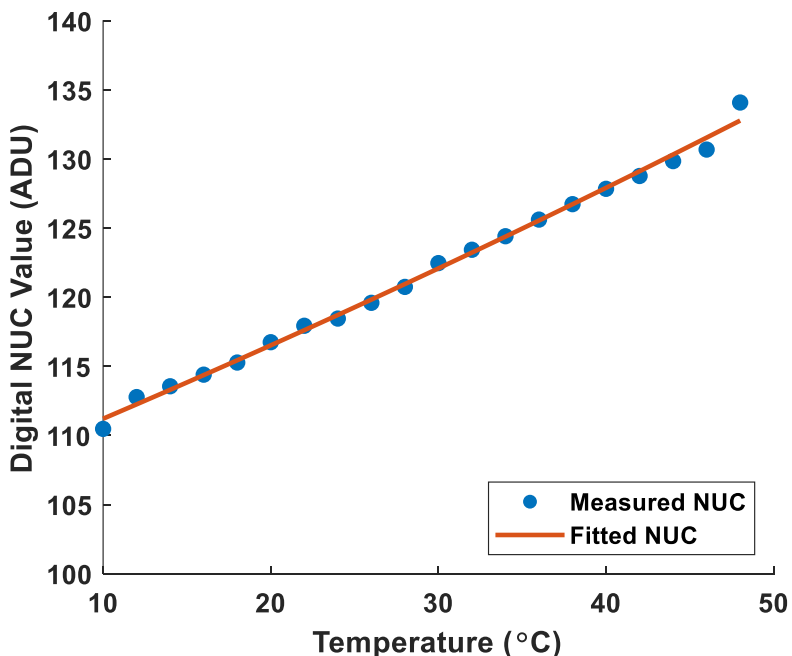


Figure 3-6: Fitted and measured mean NUC values by including global reference bias manipulations for the vanadium oxide type microbolometer for temperature.

The temperature coefficients are found for each pixel and it is seen that adjusting global reference bias makes the coefficients closer to 1 as seen in Figure 3-7. The mean of the temperature coefficients is found as 1.007.

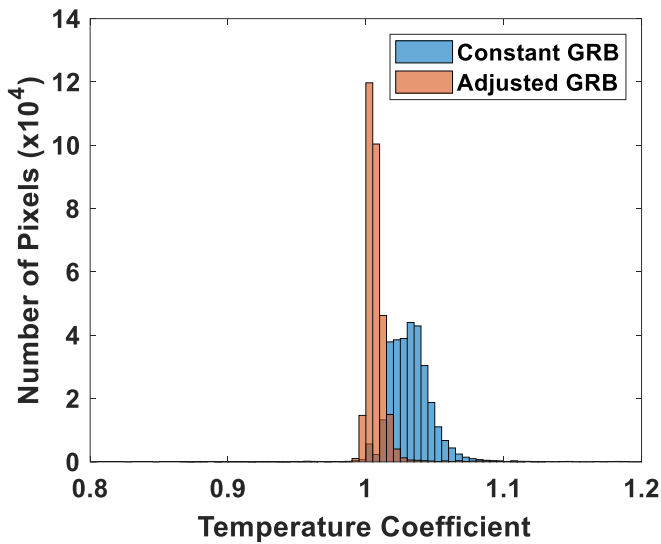


Figure 3-7: Temperature coefficients of NUC voltages for the vanadium oxide type microbolometer from 10 °C to 48 °C when the GRB is kept constant and adjusted for each temperature orderly.

Minimum and maximum errors of the estimation should be calculated to understand the quality of the estimation. For this purpose, two cases are created: NUC voltage estimation by fitting all measured NUC voltages (best case) and the estimation by fitting only initial and final NUC voltages (worst case) as seen in Figure 3-8.

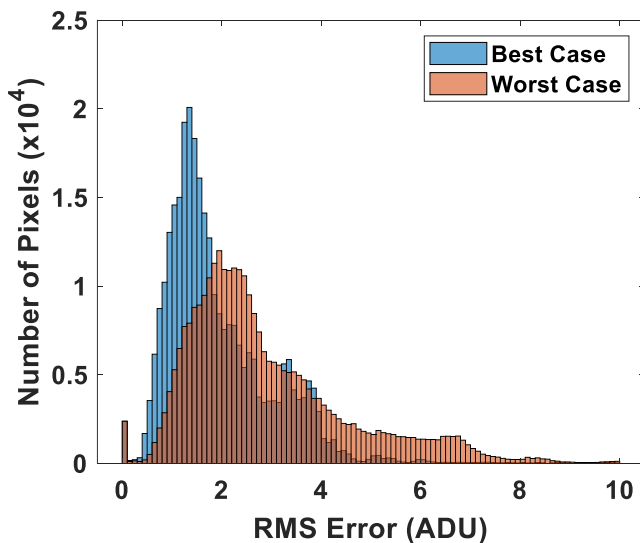


Figure 3-8: RMS errors of the estimation of NUC voltages of the vanadium oxide type microbolometer for the best and worst case.

The mean of the RMS error in the estimation is equal to 2.9 ADU for the worst-case while the value is found as 1.9 ADU for the best case. This shows that there is a relation between the number of calibration points and the error in the estimation. As a result, the estimation algorithm can be used to find NUC voltages with a small number of calibration points.

3.2 Software-Based Correction Parameters Estimation

The 2-Point correction which consists of gain and offset is used as the software-based correction. Estimation of these parameters can be divided into three groups: gain estimation, offset estimation, and temperature drift compensation. To analyze the groups, blackbody images at 25 °C, 40 °C, and 55 °C are collected for the vanadium oxide microbolometer in the temperature range between 0 °C and 50 °C, and the measurement setup in Figure 3-9 is used. The NUC voltages are estimated with the proposed method above by using the initial and final NUC voltages.

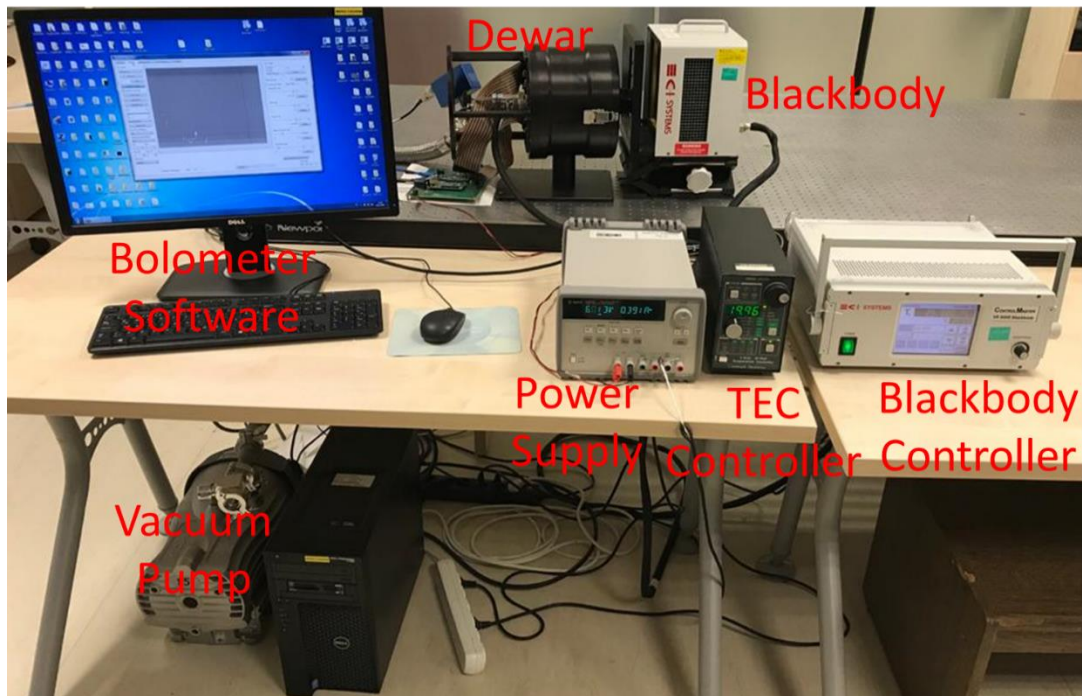


Figure 3-9: Measurement setup for microbolometers to collect uniform infrared images from the blackbody configurated in METU MEMS Center.

3.2.1 Gain Estimation

Gain can be defined as the ratio of a pixel response into the response of the FPA and it is independent of the pixel output. For this reason, the response characteristics of the pixels should be understood to estimate gain. The response of the pixel depends on the bias, detector resistance value, thermal conductance value, absorption, TCR of the detector resistance, and time constant. Temperature affects only TCR and the detector resistance value strongly. Absorption, the time constant, and thermal conductance can be thought of as constant for each pixel and the bias is controlled externally.

It is not reasonable to state that TCR characteristics of the resistances for temperature are the same although they tend to be similar and therefore, the gain map is varied. This situation makes the gain maps of the FPA material and temperature-dependent.

Bias values of the pixels are set with the proposed algorithm and it depends on the TCR differences between the detector and reference resistances. However, there is no relation between the response values of the pixels and TCR of the reference resistances. For this reason, the bias estimation causes alterations in the gain map of the FPA. Nevertheless, if the ratio of the bias into the resistances increases or decreases more than other pixels yielding an increase or decrease in the gain of the pixel when the temperature is raised, the gain tends to be higher with increasing temperature since the bias values of the pixels are set in the same ratio with temperature, in other words, temperature coefficients for NUC voltages are constant for each pixel in the entire temperature range. Thus, error in the estimation of the gain can be decreased by making linear regression for each pixel in the FPA as seen in Figure 3-10.

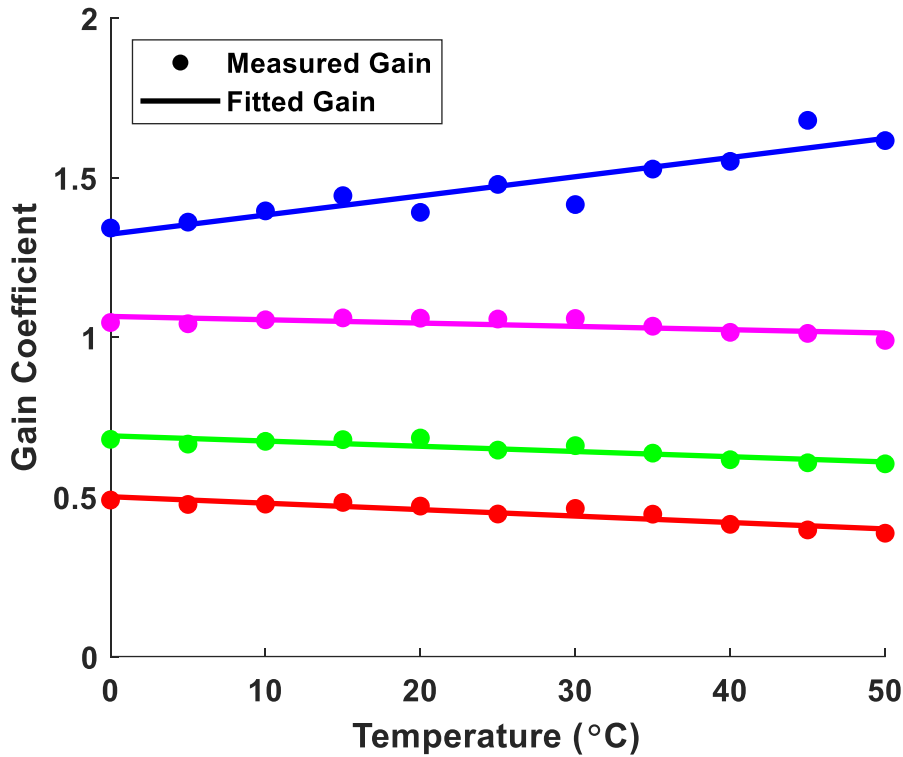


Figure 3-10: Linear regression of gain values for some pixels of the vanadium oxide type microbolometer. Each color indicates the different pixels in the FPA.

3.2.2 Offset Estimation

Offset values compensate for the difference of pixel outputs after the pixel outputs are multiplied with their gain values. Therefore, they are affected by both the gain and the bias which makes the offset estimation harder. Offset values of four different pixels of the vanadium oxide type microbolometer from 0 °C to 50 °C is shown in Figure 3-11.

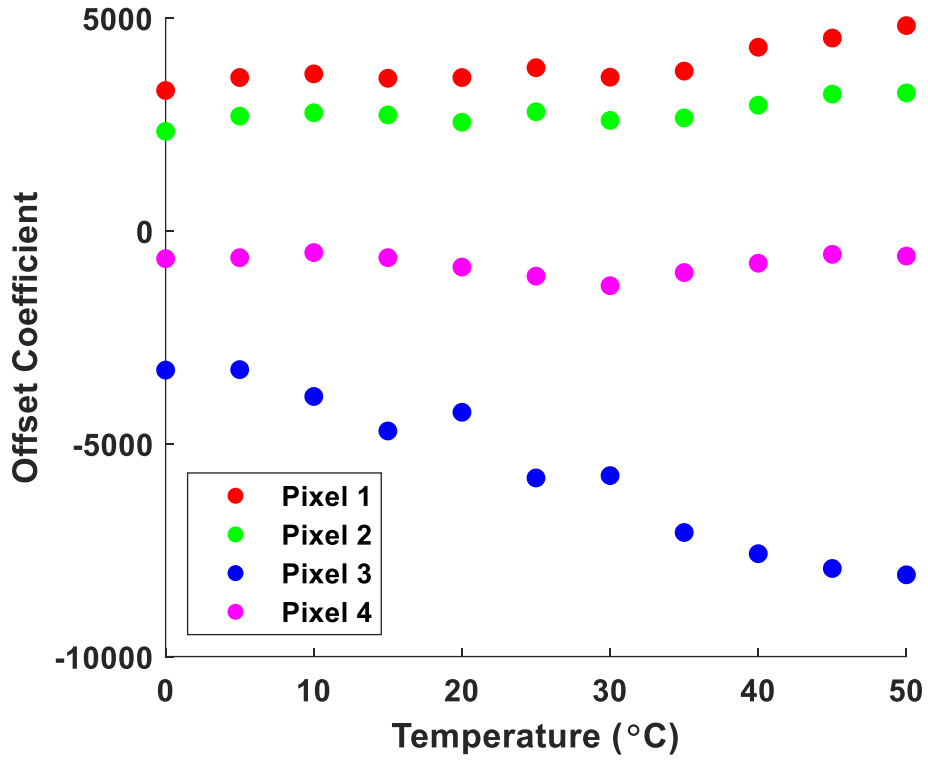


Figure 3-11: Offset values for some pixels of the vanadium oxide type microbolometer for temperature.

Bias values are updated with the proposed method which aims to find optimum NUC voltages for each temperature of the microbolometer. However, the NUC values are controlled by the DACs and input should be a digital number. Therefore, the NUC voltages found with the algorithm should be rounded. This situation results in rounding (quantization) error yielding pixel output change which should be considered while calculating the offset coefficients.

Quantization error can be explained by an example clearly. Assume that NUC voltages for a pixel is 120 at 20 °C and the temperature coefficient for the pixel is 1.02. The NUC voltages at 25 °C can be found with the algorithm as:

$$NUC_T * temp_{coef}^{\Delta T} = NUC_{T+\Delta T}$$

$$120 * 1.02^5 = 132.49 \rightarrow NUC_{25} = 132 \rightarrow \text{Rounding Error}$$
(3.38)

If the NUC step is equal to 250 ADU for the pixel at the temperature, this means that the error is 122 ADU for the case and it should be compensated by including the error into the offset value. To observe the effect, offset for the pixels are assumed as constant, and offset array at 25 °C is estimated by using the array at 20 °C and including the rounding error. After this, the difference between estimated and real offset array at 25 °C is analyzed and the effect of the rounding error compensation (REC) can be seen clearly in Figure 3-12.

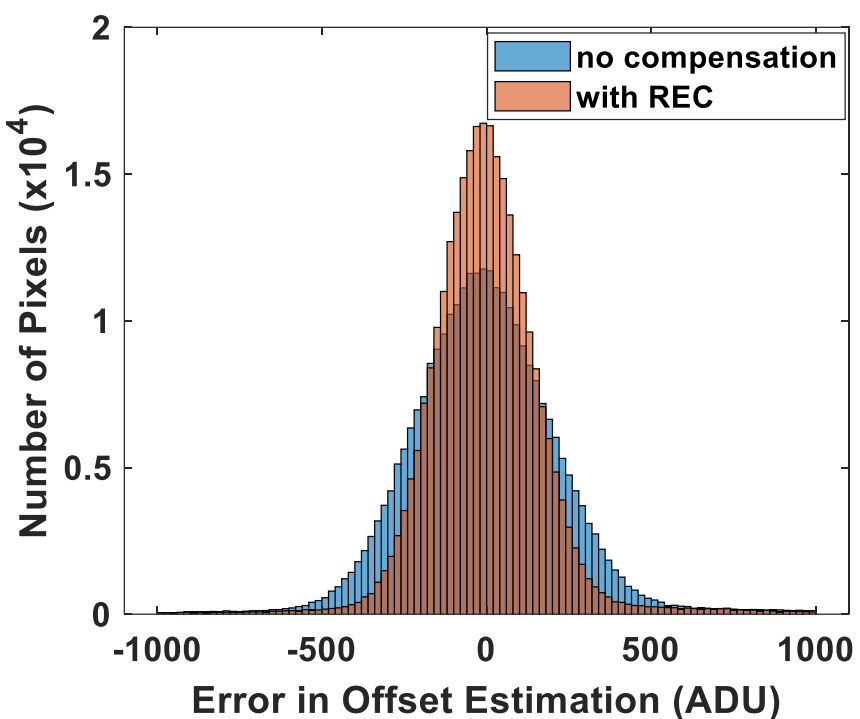


Figure 3-12: Error histograms in offset estimation to show the effect of rounding error compensation (REC) for the vanadium oxide type microbolometer.

REC decreases the error in the estimation; however, the estimation should be improved more. For this purpose, the effect of NUC voltages is analyzed deeply by selecting a pixel for which the temperature coefficient is equal to 1. In other words, pixel offset is observed against temperature when the rounding error is equal to 0. It is seen pixel offset changes as shown in Figure 3-13.

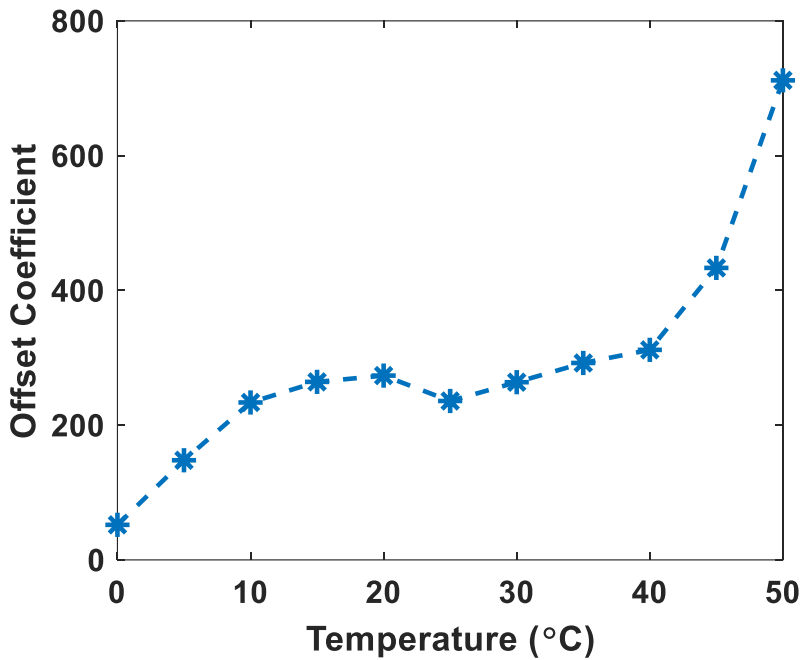


Figure 3-13: Pixel offset observation against temperature when the rounding error is 0 for the pixel.

The offset coefficient increases while the NUC voltages for the pixel is found without rounding error. Since resistances of the pixel decreases with the temperature and the NUC voltages determine the voltage on the resistances, the effect of the NUC voltage step on the pixel output increases also with the temperature. In other words, the pixel gives more response to change in the same amount of input bias due to lower resistances. It is difficult to model the effect since it depends only on the resistance values. However, to decrease the error, the linear regression method can be used as the gain. The offset array at 25 °C for the microbolometer is estimated by including the rounding error and the linear regression with the data at 20 °C and 30 °C as shown in Figure 3-14.

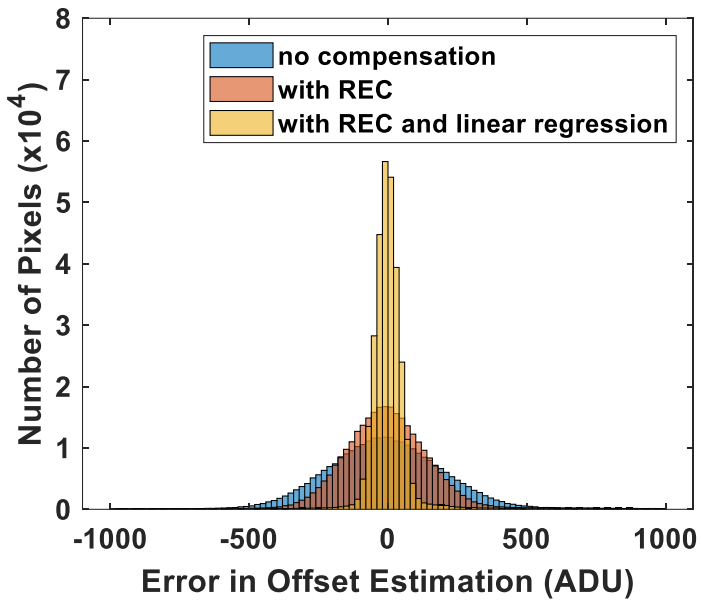


Figure 3-14: Error histograms in offset estimation to show the effect of rounding error compensation and linear regression for the vanadium oxide type microbolometer.

Offset estimations of the four pixels for the microbolometer shown in Figure 3-11 are done with REC and the linear regression by using consecutive data for each 10 °C interval as seen in Figure 3-15.

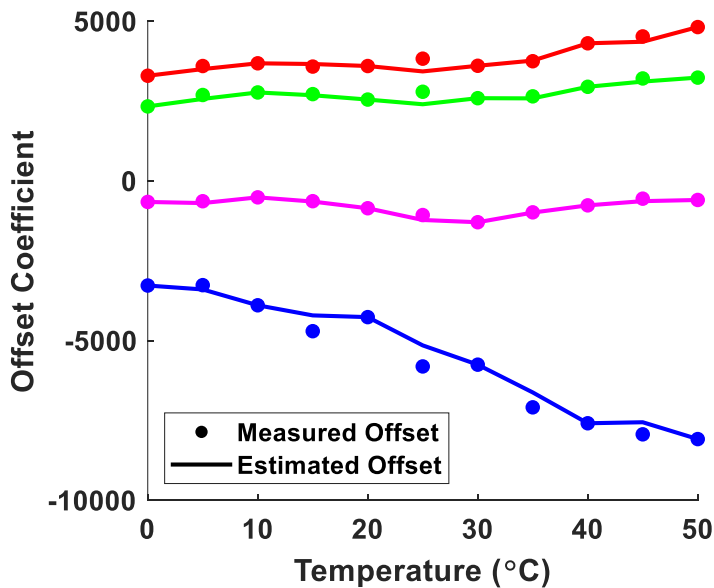


Figure 3-15: Real and estimated offset values for some pixels of the vanadium oxide type microbolometer for temperature.

3.2.3 Temperature Drift Compensation

Temperature drift definition is used to explain pixel output alterations for small temperature differences. In the proposed architecture, NUC voltages are updated for each temperature, however, pixel outputs change in the interval continuously yielding variations in gain and offset coefficients. Firstly, gain parameters should be estimated and after this, offset parameters should be considered.

Gain coefficients are strongly related to the responsivity of the pixels. Bias values are constant in the temperature range for the drift case and it is not expected to observe considerable variations in the other parameters such as resistance and TCR which affects the responsivity of the pixel. Therefore, it is logical to assume that gain coefficients are stable for a small temperature range. To analyze the assumption, gain coefficients of four different pixels are observed for 1 °C interval with 0.1 °C steps as shown in Figure 3-16.

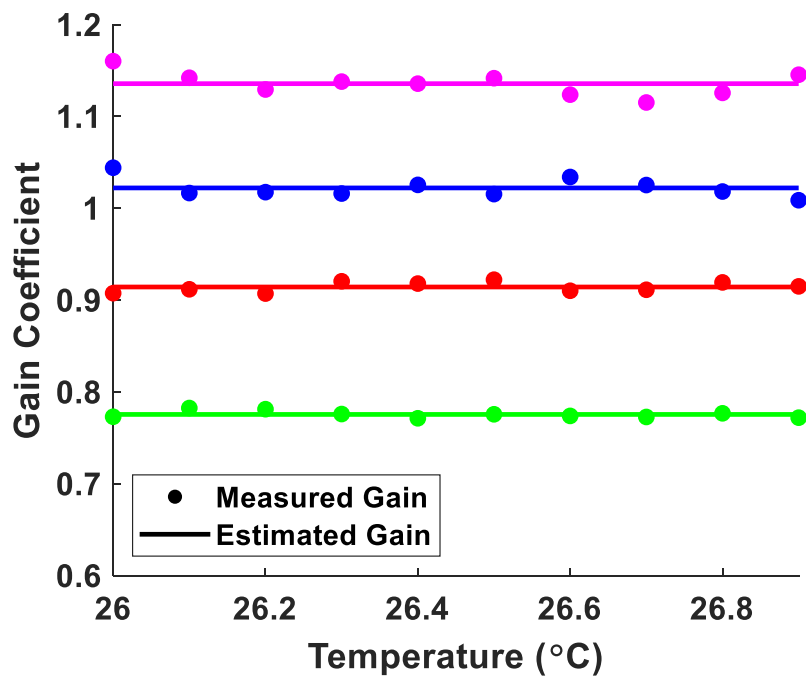


Figure 3-16: Gain coefficients of some pixels in the vanadium oxide type microbolometer for 1 °C temperature interval.

The error in the gain estimation is seen as low when the gain is kept constant. However, offset coefficients alter considerably since even small resistance variations cause significant changes in the offset when the pixel bias is high. Therefore, offset changes should be analyzed even for a small temperature range. Pixel outputs after 2-point correction at temperature T can be written as:

$$\begin{aligned} I_{out_1} &= I_{det} - I_{ref} \\ I'_{out_1} &= Gain_1 * I_{out_1} + Offset_1 \end{aligned} \quad (3.39)$$

When the temperature is raised to $T + \Delta T$, the equation becomes:

$$\begin{aligned} I_{out_2} &= I_{det} * (1 - \alpha_{det})^{\Delta T} - I_{ref} * (1 - \alpha_{det})^{\Delta T} \\ I'_{out_2} &= Gain_2 * I_{out_2} + Offset_2 \end{aligned} \quad (3.40)$$

Gain is assumed as constant in the temperature range ($Gain_1 = Gain_2 = Gain$) and to make $I'_{out_1} = I'_{out_2}$, the equation should be:

$$\begin{aligned} Gain * I_{det} * ((1 - \alpha_{det})^{\Delta T} - I_{ref} * (1 - \alpha_{ref})^{\Delta T}) + Offset_2 \\ = Gain * (I_{det} - I_{ref}) + Offset_1 \end{aligned} \quad (3.41)$$

The binomial approximation can be used to simplify some terms as:

$$\begin{aligned} (1 - \alpha_{det})^{\Delta T} &\approx 1 - \Delta T * \alpha_{det} \\ (1 - \alpha_{ref})^{\Delta T} &\approx 1 - \Delta T * \alpha_{ref} \end{aligned} \quad (3.42)$$

The equation can be written finally as:

$$Gain * (I_{det} * \alpha_{det} - I_{ref} * \alpha_{ref}) * \Delta T + Offset_1 \approx Offset_2 \quad (3.43)$$

The final equation states that offset coefficients can be modeled as linear by assuming the TCR and gain coefficients are constant for small temperature ranges.

Offset coefficients for four pixels from the vanadium oxide type microbolometer used in Figure 3-16 are fitted into the linear equation for the same temperature range to observe whether the linear regression can be used as shown in Figure 3-17.

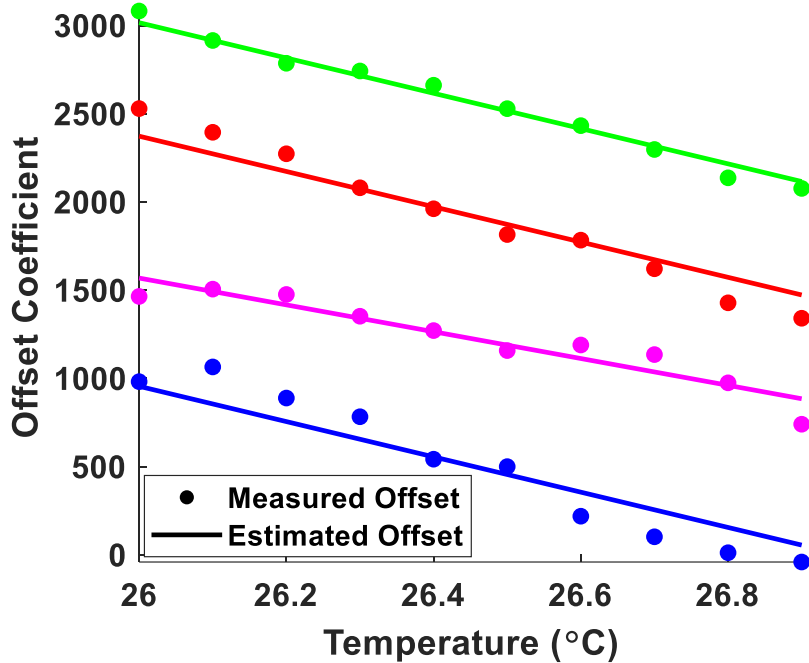


Figure 3-17: Offset coefficients of some pixels in the vanadium oxide type microbolometer for 1 °C temperature interval.

The slope of the offset coefficients for temperature drift depends on the gain, current drawn by the resistances, and the TCR values. All of these parameters change for each temperature yielding alteration in the slope. For this reason, the slope is analyzed mathematically when the temperature is raised in the amount of 1 °C.

At temperature T, the slope can be written as:

$$\begin{aligned} Slope_1 &= Gain_1 * (I_{det} * \alpha_{det} - I_{ref} * \alpha_{ref}) \\ &\approx Gain_1 * I_{det}(\alpha_{det} - \alpha_{ref}) \end{aligned} \quad (3.44)$$

At the temperature T+1, the slope equation should be updated as:

$$\begin{aligned} Slope_2 &= Gain_2 * (I'_{det} * \alpha'_{det} - I'_{ref} * \alpha'_{ref}) \\ &\approx Gain_2 * I'_{det}(\alpha'_{det} - \alpha'_{ref}) \end{aligned} \quad (3.45)$$

The ratio of these slopes (r) can be shown as:

$$r = \frac{Slope_1}{Slope_2} = \frac{Gain_1 * I_{det}(\alpha_{det} - \alpha_{ref})}{Gain_2 * I'_{det}(\alpha'_{det} - \alpha'_{ref})} \quad (3.46)$$

The differences between the detector and reference resistances can be assumed as constant like the analysis of NUC voltage estimation. Moreover, the ratio of the gain values is thought as very close to 1 when the temperature difference is 1 °C. Therefore, the ratio can be simplified as:

$$r = \frac{I_{det}}{I'_{det}} = \frac{1}{(1 + \alpha_{det})} \quad (3.47)$$

It is seen that the ratio depends strongly on the TCR values, however, it can be fitted into the exponential function to decrease error in the estimation as:

$$Slope_{T+\Delta T} = Slope_T * dc^{\Delta T} \quad (3.48)$$

where dc implies the drift coefficient. The equation assumes the terms of $1 + \alpha_{det}$ is constant in the temperature range. Whereas nonlinear TCR characteristics of the vanadium oxide make this assumption worse, the fact that the TCR is very small compared to 1 improves the quality of the assumption. Since the TCR of the vanadium oxide changes between -2 %/K and -5 %/K, the coefficient should be calculated in the range between 1.02 and 1.05. For this purpose, the slopes are found for each 5 °C in the temperature range between 0 °C and 50 °C and fitted into the equation. As a result, the coefficient which the fit equation gives is equal to 1.033 as expected shown in Figure 3-18.

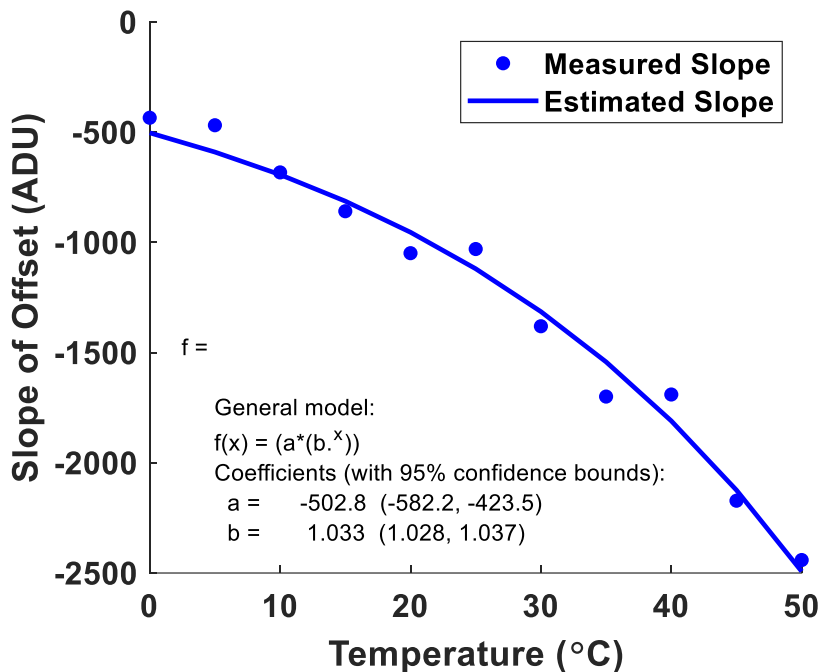


Figure 3-18: Measured and fitted temperature drift slopes for the microbolometer.

3.3 Results and Discussion

Three vanadium oxide type microbolometers which have an array size of 640x480 are used to analyze the algorithms in the thesis work. They belong to different wafers and there are differences in the process of these wafers such as the thickness of some layers and they are labeled as *Sample 6*, *Sample 7*, and *Sample 8*. Since the first five samples (from *Sample 1* to *Sample 5*) are used for comparison of NUC methods as seen in Table 2-3. Therefore, it is expected that their temperature characteristics are not the same. In the experiment, temperatures of the microbolometers are controlled via the TEC and the measurement setup shown in Figure 3-9 is used for all of them. The vacuum level is decreased down to 5 mTorr for the measurements. Firstly, NUC voltages are optimized for each 5 °C in the temperature range between 0 °C and 50 °C with the algorithm proposed in CHAPTER 2. Improvements in the uniformity are illustrated at 20 °C for each microbolometer in Figure 3-19.

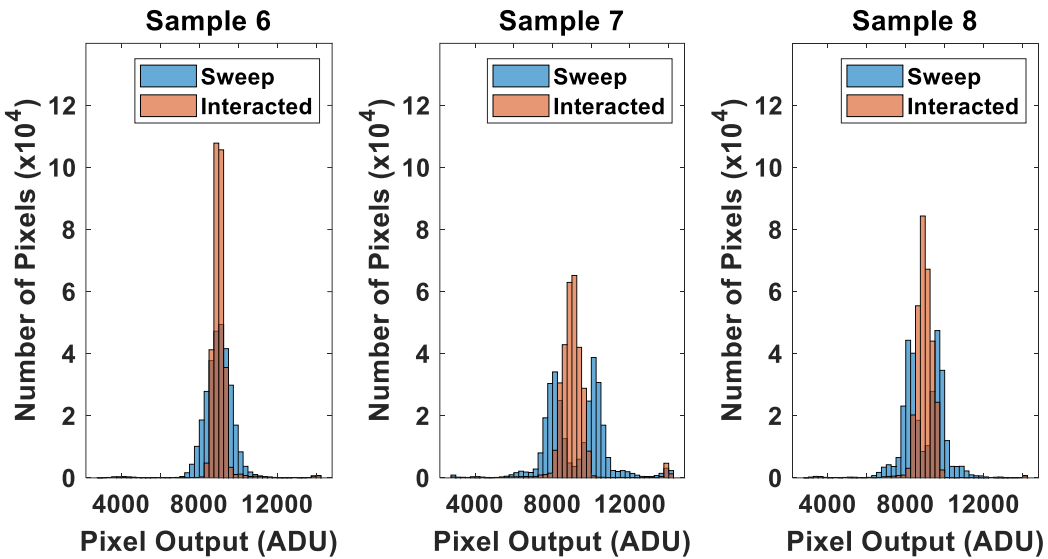


Figure 3-19: Output histograms for *Sample 6*, *Sample 7*, and *Sample 8* after NUC voltages are found with sweep and interacted algorithms, respectively.

NUC voltages are estimated by using the data for each 10 °C in the temperature range. After this, outputs are saved for each temperature point to compare output uniformities with the calibrated data for each point as seen in Figure 3-20, Figure 3-21, and Figure 3-22.

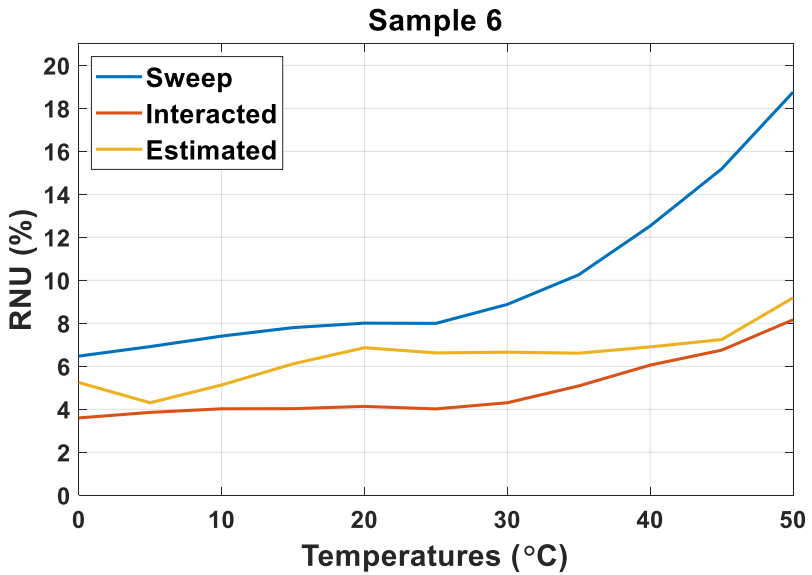


Figure 3-20: RNU values of output distribution at each temperature point after NUC voltages are found with the sweep method, interacted method, and NUC voltages estimation for *Sample 6*.

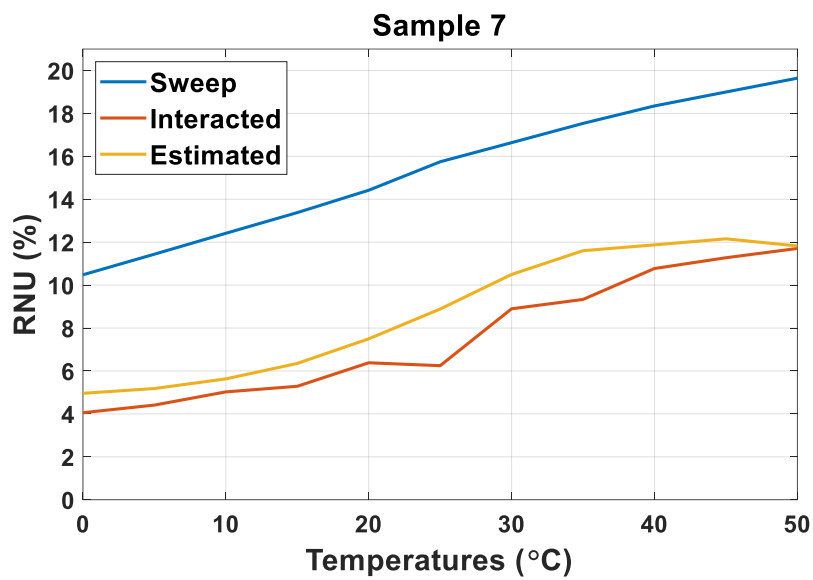


Figure 3-21: RNU values of output distribution at each temperature point after NUC voltages are found with the sweep method, interacted method, and NUC voltages estimation for *Sample 7*.

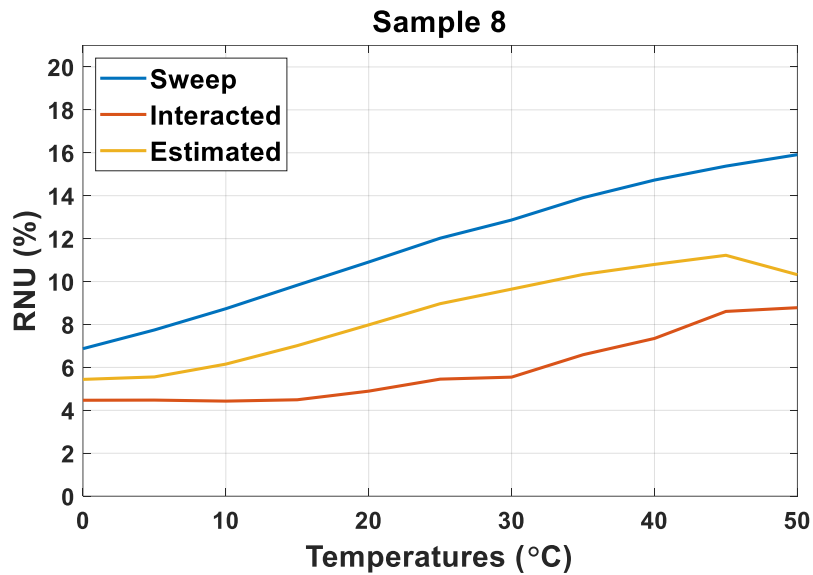


Figure 3-22: RNU values of output distribution at each temperature point after NUC voltages are found with the sweep method, interacted method, and NUC voltages estimation for *Sample 8*.

The NUC voltage estimation results in lower RNU than obtained one with sweep algorithm for each temperature, whereas the RNU values higher than the interacted algorithm due to error in the estimation.

NUC voltage estimation causes deviation in the mean of output distribution because of estimation error. Generally, all pixel outputs shift and the RNU value is not changed much whereas the mean of the output distribution alters. The deviations in the mean can be seen in Figure 3-23 for all samples.

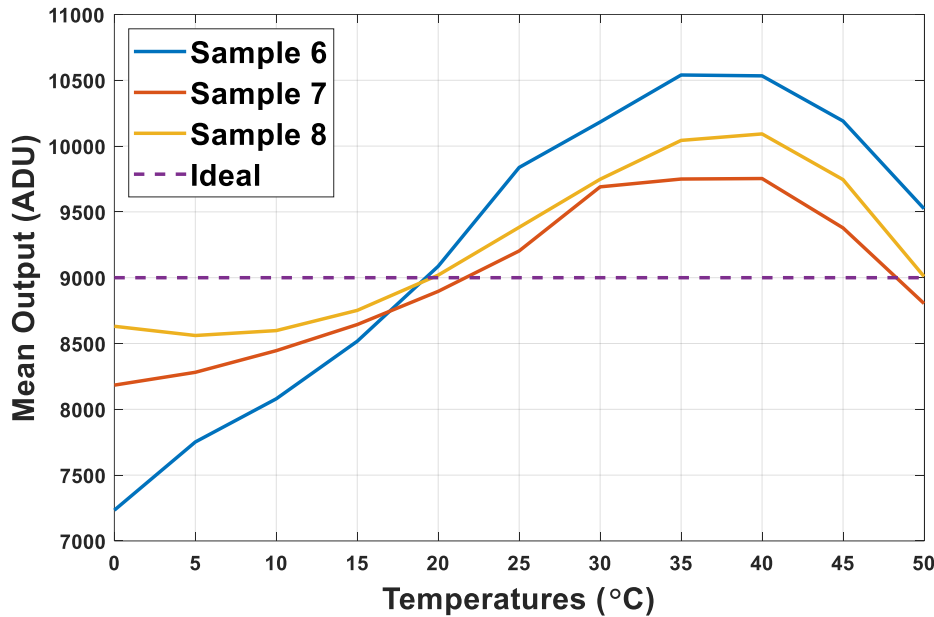


Figure 3-23: Mean values of output distributions for *Sample 6*, *Sample 7*, and *Sample 8* when NUC voltages are found with the proposed estimation method.

Pixel outputs are not saturated considerably whereas the mean shifts since the mean values change between 7000 ADU and 11000 ADU for the worst case when *Sample 6* is used. The difference between the quality of the estimation depends on the TCR characteristics of the microbolometers. The estimation algorithm assumes that the TCR difference between the detector and reference resistances is constant. The results show that the assumption is more valid for *Sample 8*. The functional region for pixels is between 2500 ADU and 14400 ADU and the mean values do not reach these points. This enables to compensate for the shift in the mean of output distribution with software-based corrections. However, some pixels can reach these points, and to observe this, saturated pixel ratios obtained with these algorithms are compared in Figure 3-24, Figure 3-25, and Figure 3-26.

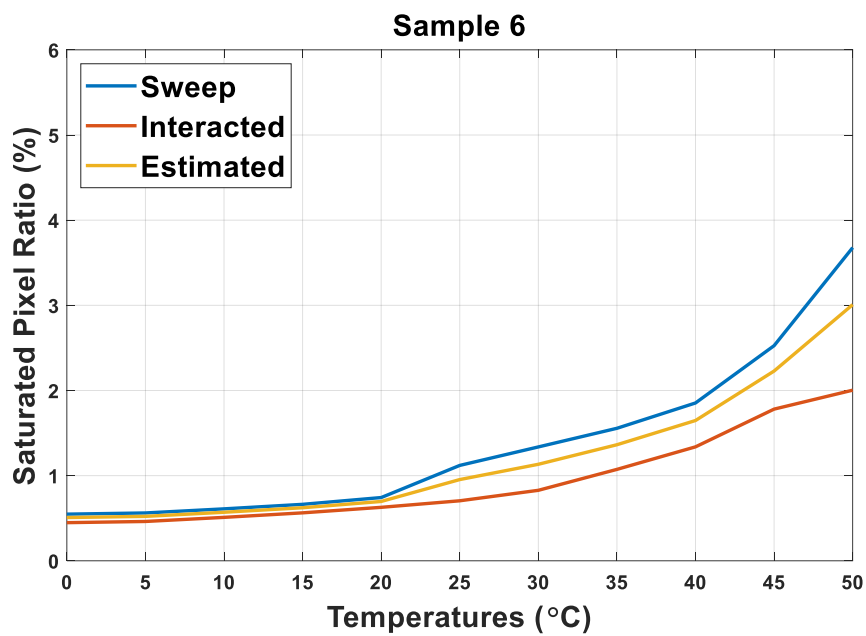


Figure 3-24: Saturated pixel ratios at each temperature point after NUC voltages are found with the sweep method, interacted method, and NUC voltages estimation method for *Sample 6*.

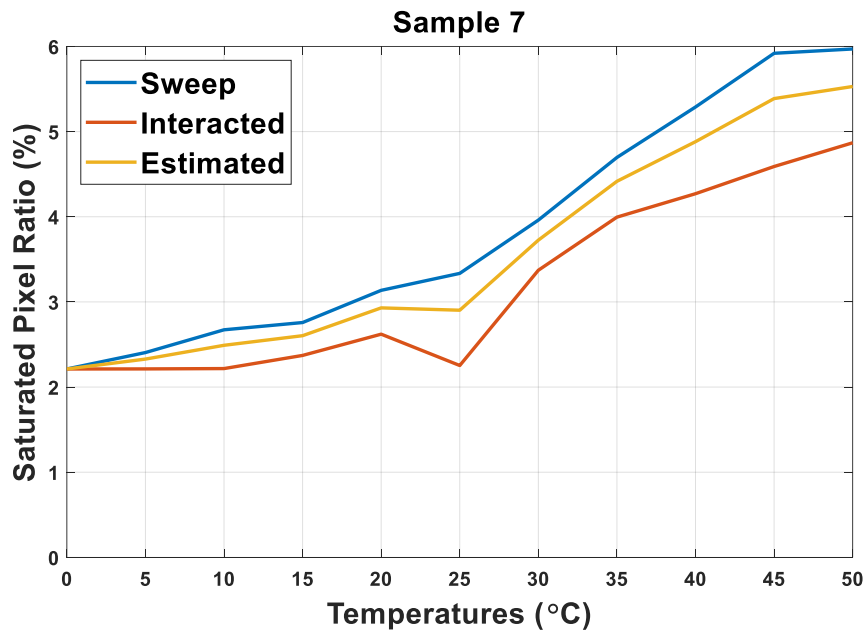


Figure 3-25: Saturated pixel ratios at each temperature point after NUC voltages are found with the sweep method, interacted method, and NUC voltages estimation method for *Sample 7*.

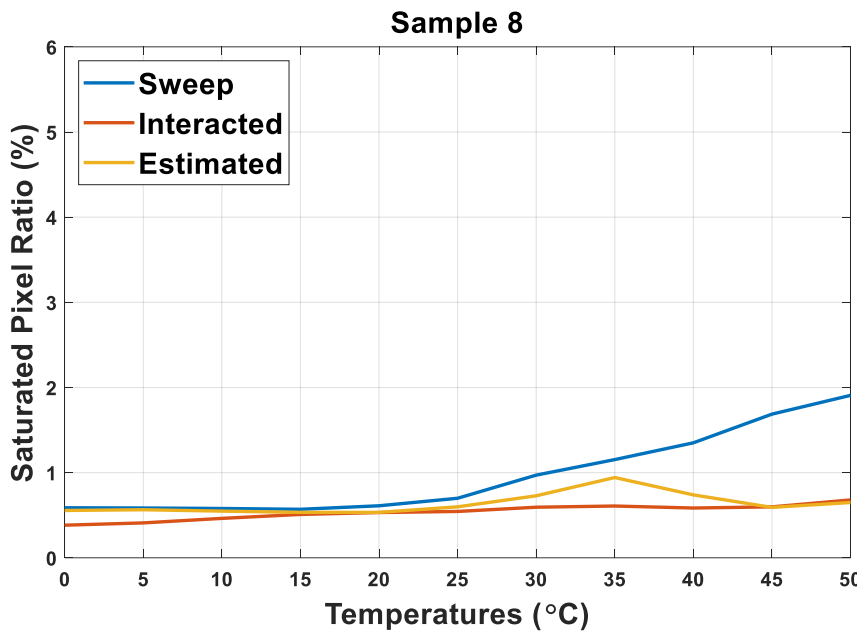


Figure 3-26: Saturated pixel ratios at each temperature point after NUC voltages are found with the sweep method, interacted method, and NUC voltages estimation method for *Sample 8*.

The saturated pixel ratio increases with the temperature due to the increase in the NUC step. At low temperatures, even if NUC voltages are estimated wrongly, the pixel output does not reach to saturation region. However, small errors in the estimations are enough to saturate pixels when the temperature is increased. Therefore, the difference in saturated pixel ratios between the interacted NUC and the estimation becomes significant at high temperatures. Nevertheless, the estimated NUC voltages provide a lower saturated pixel ratio than the sweep method for all temperature points.

Blackbody images at 25 °C, 40 °C, and 55 °C are obtained for each 5 °C from 0 °C to 50 °C when the NUC voltages are found with the estimation. Moreover, three temperature points are added for each temperature point with 0.3 °C steps while the NUC voltages are constant to analyze the temperature drift. In other words, each temperature point used in the NUC voltage analysis is divided into 4 groups with a 0.3 °C temperature step to analyze 2-point correction parameters seen in Table 3-1.

Table 3-1: Microbolometer temperature points when the data are collected.

Data	Microbolometer Temperature (°C)										
NUC Voltages	0.0	5.0	10.0	15.0	20.0	25.0	30.0	35.0	40.0	45.0	50.0
Software-Based Correction	0.0	5.0	10.0	15.0	20.0	25.0	30.0	35.0	40.0	45.0	50.0
	0.3	5.3	10.3	15.3	20.3	25.3	30.3	35.3	40.3	45.3	50.3
	0.6	5.6	10.6	15.6	20.6	25.6	30.6	35.6	40.6	45.6	50.6
	0.9	5.9	10.9	15.9	20.9	25.9	30.9	35.9	40.9	45.9	50.9

The images taken from the blackbody at 25 °C and 55 °C are used to calculate 2-point correction parameters and these parameters are applied to the images collected when the blackbody is at 40 °C. RNU values for each temperature point are obtained after the 2-point correction. Estimation error of gain and offset parameters increases if the number of temperature points for linear regression is decreased seen in Figure 3-27.

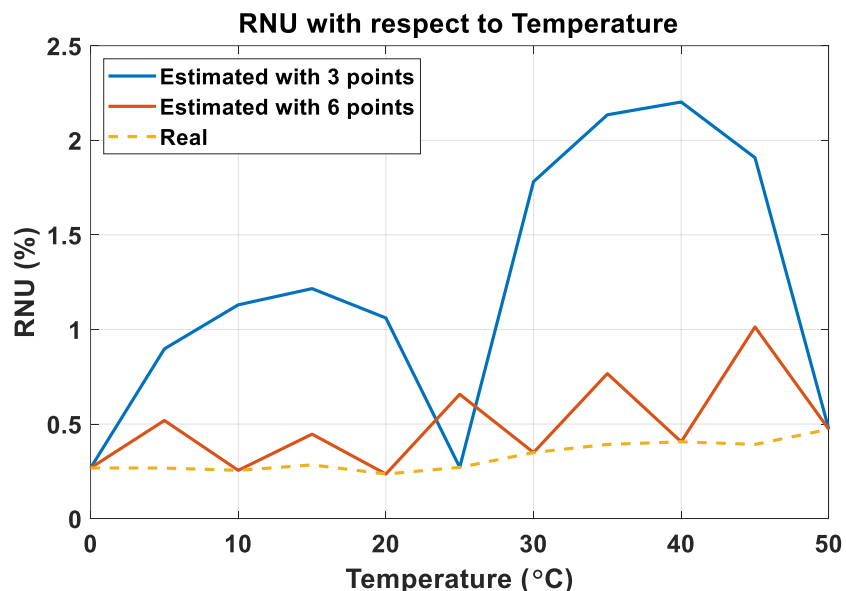


Figure 3-27: RNU values for temperature when 3 and 6 temperature points are used to linear regression for *Sample 6*.

The number of temperature points used in the estimation has a significant effect on the RNU values. Therefore, to decrease the RNU, gain arrays are estimated by using the data at each 10 °C from 0.0 °C to 50.0 °C with the linear regression method explained in Part 3.2.1. Offset arrays at these 6 temperature points are calculated by using the estimated gain parameters. Linear regression method is used to estimate offset coefficients for each temperature point by considering also rounding error compensation (REC) as stated in 3.2.2. REC is applied before the linear regression to decrease the error in the estimation. Finally, temperature drift compensation parameters are found by exponentially fitting the initial and final slopes. For each pixel, the initial slope is found with the data collected at 0.0 °C, 0.3 °C, 0.6 °C, and 0.9 °C while the data between 50 °C and 50.9 °C with 0.3 °C step provide the final slope. As a result, 12 temperature points are used to estimate 2-point correction parameters via 44 temperature points. The algorithm is applied to these three samples and RNU values are compared with one obtained by using real 2-point correction parameters as seen in Figure 3-28, Figure 3-29, and Figure 3-30.

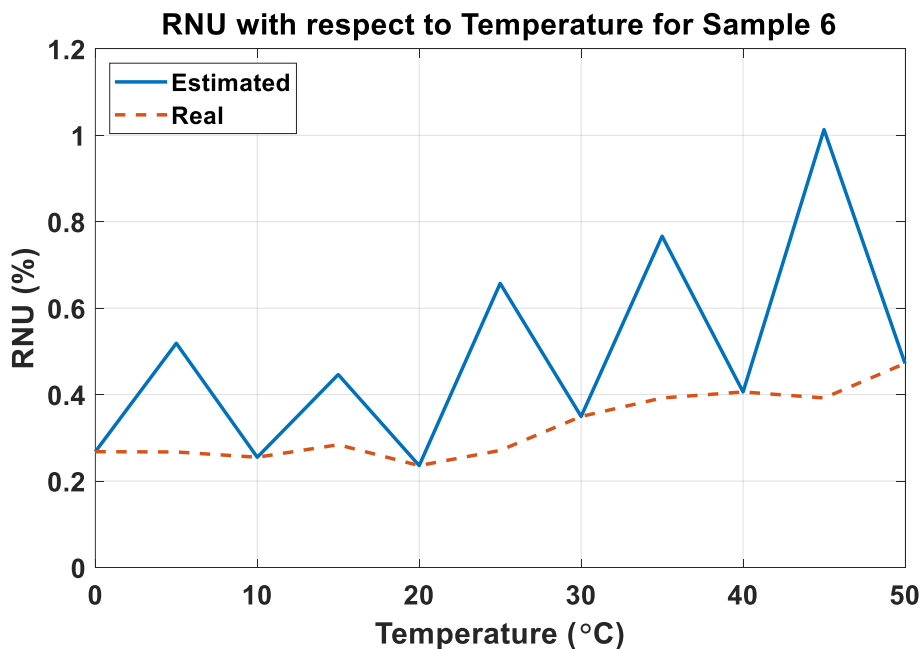


Figure 3-28: RNU values for temperature when 6 temperature points are used to linear regression for *Sample 6*.

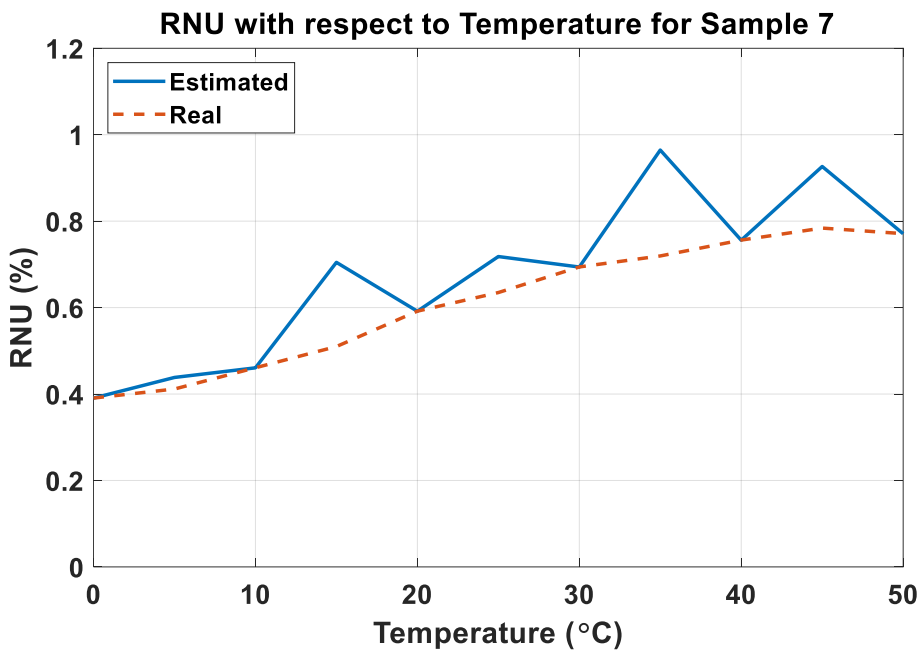


Figure 3-29: RNU values for temperature when 6 temperature points are used to linear regression for *Sample 7*.

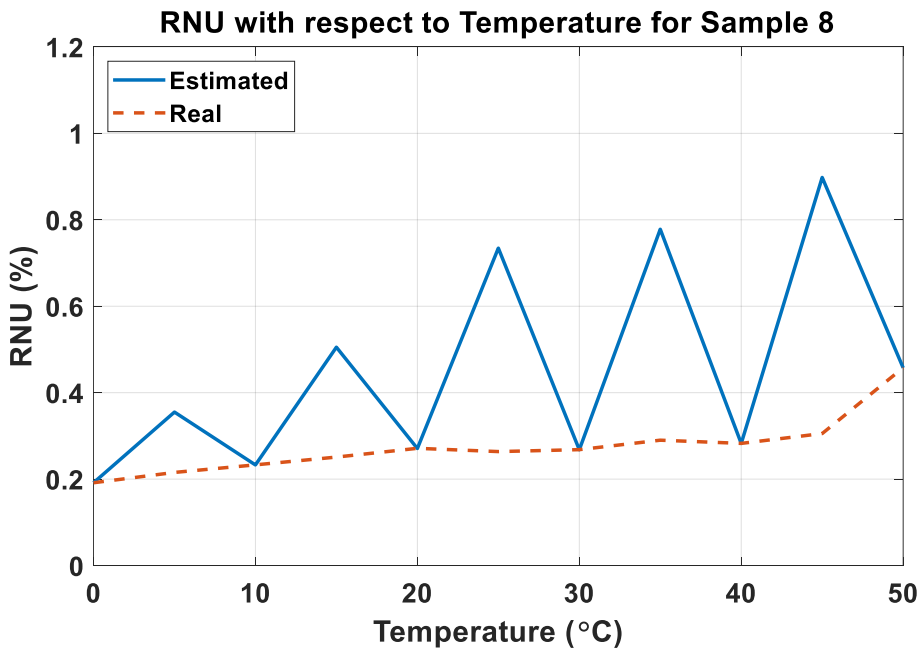


Figure 3-30: RNU values for temperature when 6 temperature points are used to linear regression for *Sample 8*.

The RNU values for these samples at the temperatures which are not used in the linear regression are also shown numerically in Table 3-2.

Table 3-2: RNU values for *Sample 6*, *Sample 7*, and *Sample 8* obtained with the proposed algorithm.

Sample ID	RNU (%)				
	5 °C	15 °C	25 °C	35 °C	45 °C
<i>Sample 6</i>	0.52	0.45	0.66	0.77	1.01
<i>Sample 7</i>	0.44	0.70	0.72	0.96	0.93
<i>Sample 8</i>	0.36	0.51	0.73	0.78	0.90

RNU values increase with the temperature after the 2-point correction. This can be explained by two reasons: The first one is related to the responsivity of the pixels and the second one is related to NUC voltage estimation. Responsivity increases with the temperature since the current drawn by the resistances also increases. This situation makes the response characteristics for incoming infrared illumination high order polynomial. Therefore, the linear assumption gives more error at high temperatures. Moreover, the error in the NUC voltage estimation increases with the temperature due to the higher NUC step as explained in 3.1 and it results in a higher error in the offset estimation yielding a higher RNU value. *Sample 8* gives better results than other samples as observed in the NUC voltage estimation. It is seen that the assumptions used in the algorithm are more suitable for *Sample 8*. A significant increase is observed in the RNU values of *Sample 7* when the temperature is raised from 25 °C to 35 °C. Most probably, TCR values of reference and detector resistances show different temperature characteristics in the region. This results in a considerable increase in the error of NUC voltage estimation as seen in Figure 3-21 and the error increases the RNU. This situation implies that the efficiency of the algorithm changes with the characteristics of the sample. As a result, it is possible to state that the proposed algorithm provides RNU lower than 1% at low temperatures whereas the value is around %1 when the temperature is increased.

Thermal images without any correction from *Sample 7* and *Sample 8* for each temperature point used in Table 3-2 are saved. *Sample 6* is damaged electrically during the experiment at 15 °C. After this, real and estimated 2-point correction parameters are applied to these images. Finally, 3x3 median filtering is used for dead pixels and histogram equalization is used to increase contrast. As an example, corrected images at 5 °C are shown in Figure 3-31.

Real 2-P. Correction



Sample 6



Sample 7



Sample 8

Estimated 2-P. Correction



Sample 6



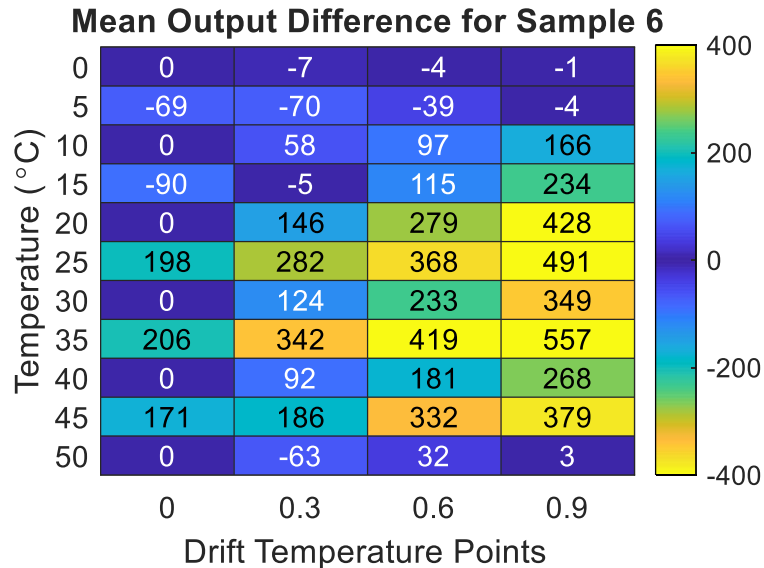
Sample 7



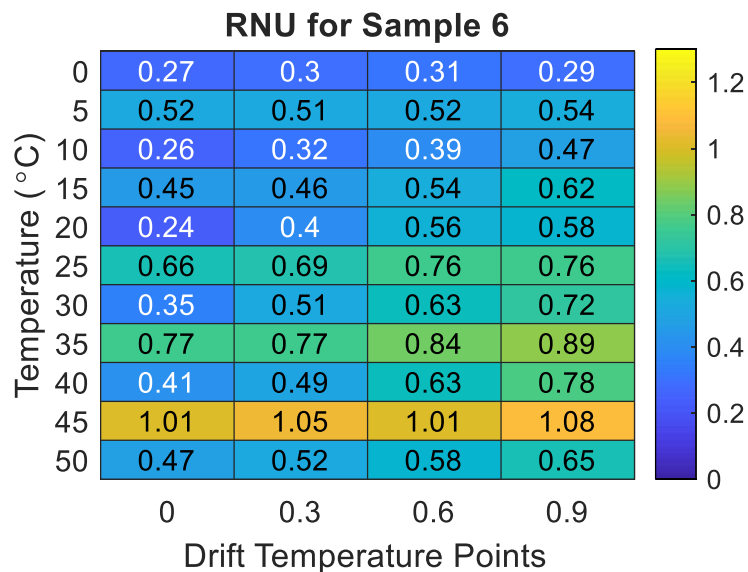
Sample 8

Figure 3-31: Thermal images obtained from *Sample 6*, *Sample 7*, and *Sample 8* with real and estimated 2-point correction at 5 °C.

Temperature drift is compensated also for the temperatures as shown in Table 3-1 and RNU values for each temperature point are found. Moreover, the mean values of the output are also calculated. The RNU and mean output difference between real and estimated cases can be seen in Figure 3-32, Figure 3-33, and Figure 3-34.

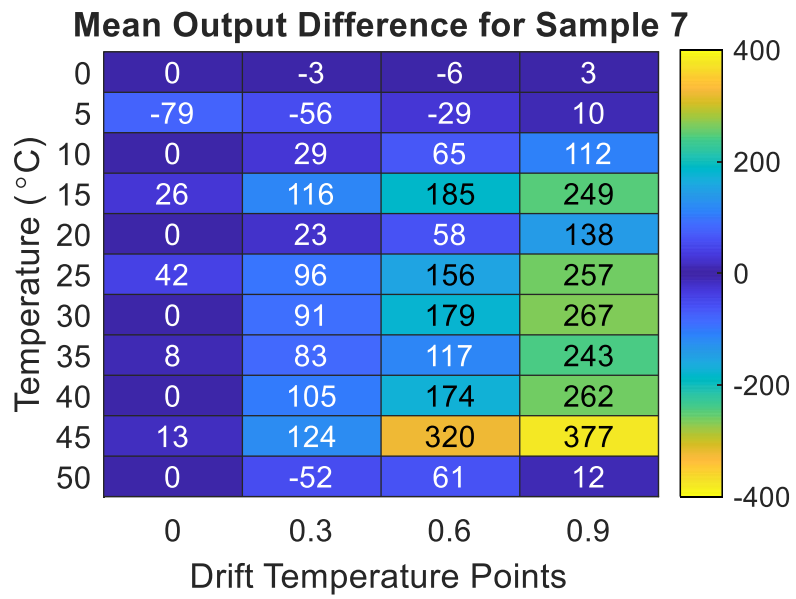


(a)

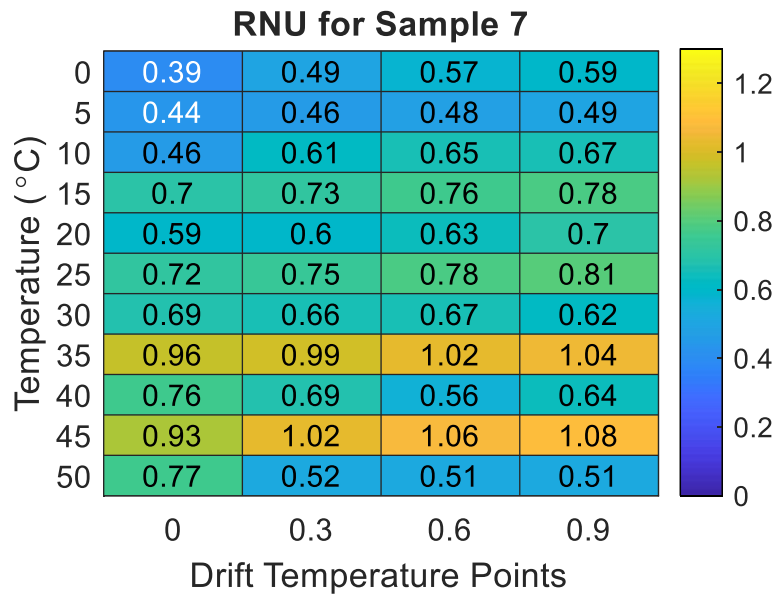


(b)

Figure 3-32: (a) Mean (ADU) and (b) RNU (%) values of *Sample 6* after 2-point correction parameters are found with the temperature drift compensation algorithm.

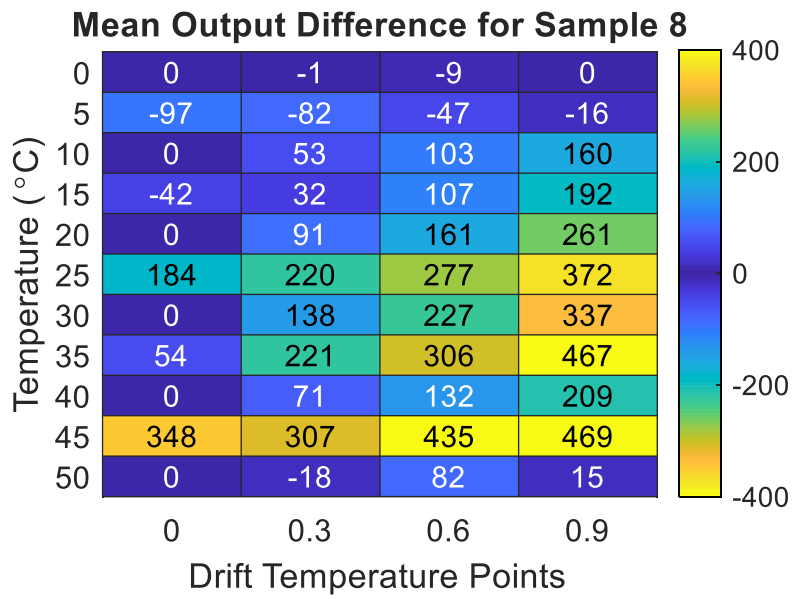


(a)

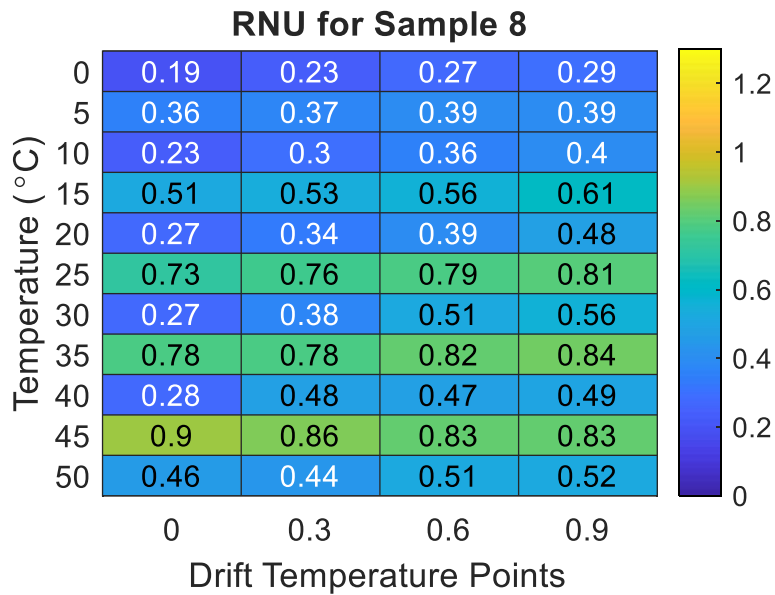


(b)

Figure 3-33: (a) Mean (ADU) and (b) RNU (%) values of *Sample 7* after 2-point correction parameters are found with the temperature drift compensation algorithm.



(a)



(b)

Figure 3-34: (a) Mean (ADU) and (b) RNU (%) values of *Sample 8* after 2-point correction parameters are found with the temperature drift compensation algorithm.

The x-axis and y-axis show the microbolometer temperatures in the figures above. For example, the data in the 3rd row and the 2nd column indicates the microbolometer temperature is 10.3 °C.

The mean output difference increases with the drift temperature points since the slope of the drift is estimated in the temperature drift algorithm and the error in the slope estimation causes higher errors with increasing temperature. Moreover, due to the increase in the error of NUC voltage estimation for high temperatures, the mean output difference becomes higher at these temperatures. The highest difference among these samples is 557 ADU which is obtained at 35.9 °C for *Sample 6*. The value is insufficient to make pixels saturated and it is not seen clearly in thermal images if histogram equalization mode is automatic, which implies the minimum and maximum points of the colormap are updated concerning the mean of the output histogram. The maximum difference between the mean values is 82 ADU at calibration temperatures for temperature drift estimation (0 °C and 50 °C). This situation shows that the main error contribution in thermal drift compensation depends on the offset estimation and exponential modeling of slope values for the drift. In other words, although linear regression for the drift compensation provides a small error, the error increases considerably due to contributions of other estimations. It is possible to increase the number of used temperatures for the drift compensation to decrease error in the estimation, however, this increases the computational time significantly. Since, when two points are used for the exponential estimation, no fit equation is required and related coefficients can be found directly. On the other hand, when RNU values are compared for drift temperature points, it is seen that the RNU value at the initial case is almost protected. This shows the error in the slope calculation is almost the same for all pixels. The situation prevents thermal images from getting worse with drift temperature points considerably. Images obtained from *Sample 8* at 15.0 °C, 15.3 °C, 15.6 °C, and 15.9 °C are shown in Figure 3-35. The RNU values for the temperature range increase from 0.51% to 0.61% and mean output differences are raised from -42 ADU to 192 ADU. However, there are small differences that are appeared in the images and therefore it is possible to claim that the temperature drift algorithm works properly. In addition to these, all images taken from these samples can be seen in A, B, and C, respectively.

Real 2-P. Correction



15.0 °C



15.3 °C



15.6 °C



15.9 °C

Estimated 2-P. Correction



15.0 °C



15.3 °C



15.6 °C



15.9 °C

Figure 3-35: Thermal images obtained from *Sample 8* at 15.0 °C, 15.3 °C, 15.6 °C, and 15.9 °C with real and estimated 2-point correction parameters.

The performance of the algorithm is compared with some studies performed about the issue. In the study in 2015 [49], a shutterless algorithm is proposed and the performance of the algorithm is shown by using RNU in terms of mK. Therefore, the performances of all samples used in the thesis are converted into RNU in terms of mK to compare the results as shown in Figure 3-36.

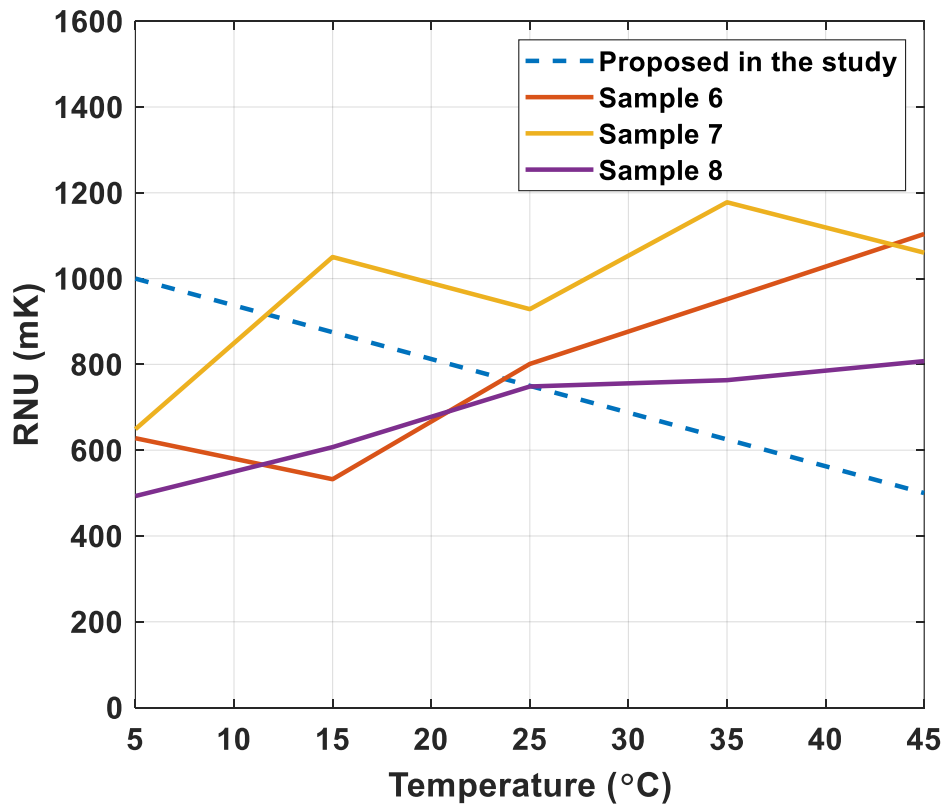


Figure 3-36: Comparison of proposed algorithms in the study [49] and the thesis.

The RNU value should be increased with the temperature in terms of ADU. However, the responsivity of the microbolometers is also increased with the temperature due to the higher current under almost the same bias. Therefore, The RNU value in terms of mK can be decreased as seen in the study [49]. At low temperatures, the algorithm proposed in the thesis gives better results, however, the performance is getting worse with increasing temperature. If the mean RNU values are compared, it is possible to state that the algorithm can work as well as the algorithm in the study for shutterless applications.

The performance of the algorithm is also compared with the study performed in 2017 [52] and the PSNR values are calculated for the comparison as seen in Figure 3-37. The images taken at the temperatures from 5 °C to 45 °C with 10 °C steps are used in the calculation.

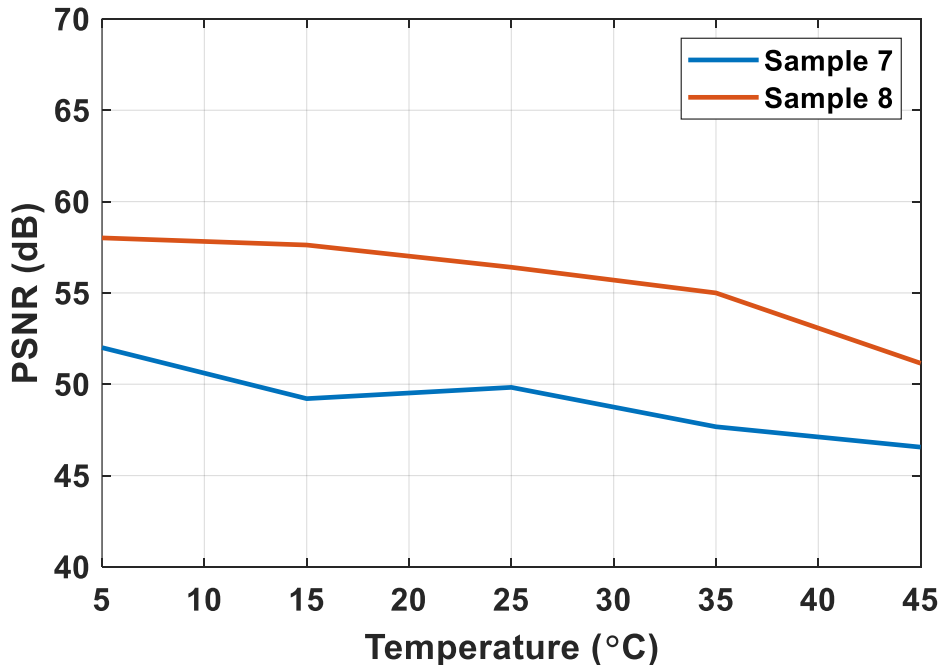


Figure 3-37: PSNR values of *Sample 7* and *Sample 8* for temperature.

The proposed algorithm in the study [52], which can be called LIM (Lagrange interpolation method), is compared with two known shutterless algorithms which are MSSE (minimizing the sum of squares of errors) and TBS (template-based solution). The PSNR values are compared with the average PSNR values obtained with the algorithm in the thesis as seen in Table 3-3.

Table 3-3: PSNR value comparison of different algorithms.

Shutterless Algorithm	LIM	MSSE	TBS	Proposed	
				Sample 7	Sample 8
PSNR (dB)	57.44	57.06	53.03	49.05	55.64

There is a significant difference between the PSNR values of *Sample 7* and *Sample 8* like observed in the RNU values. Moreover, the values alter considerably with microbolometer temperature. When the average values are compared, it is observed that the performance of the algorithm is close to the LIM and MSSE methods and better than the TBS method for *Sample 8*. The PSNR difference between LIM or MSSE and the proposed algorithm does not indicate directly that these algorithms are better than the proposed algorithm since the microbolometer camera used in the study is an amorphous silicon type microbolometer which is much more uniform TCR characteristics compared to vanadium oxide. As a result, it can be said that the proposed algorithm is suitable for shutterless applications even for vanadium oxide type microbolometers.

CHAPTER 4

CONCLUSION AND FUTURE WORK

The study conducted in the thesis focuses on the shutterless algorithm for infrared imaging systems with vanadium oxide type microbolometers. The algorithm is composed of two main parts: bias optimization and software-based corrections. Initially, bias values for the pixels, NUC voltages, are optimized at steady-state case including the interactions between pixels to decrease nonuniformity and saturated pixel ratio. After this, the NUC voltage estimation algorithm is developed which requires at least two calibration points so that NUC voltages can be found for each temperature with acceptable error. Finally, software-based corrections are estimated for each temperature point concerning response characteristics and pixel output levels after the related NUC voltages are applied. The algorithm is applied to three different microbolometers and obtained results are compared with known shutterless algorithms. It is seen that the algorithm provides low RNU and high PSNR values, especially at low temperatures.

The achievements obtained during the thesis work can be listed as:

1. Saturated pixel ratio is decreased with the NUC voltage optimization. This can also reduce the size of the clusters since neighboring pixels to clusters tend to be saturated due to interaction between pixels. Higher than 99% operability is obtained by using the optimization.
2. RNU improvement with the NUC voltage optimization can change from die to die. Among the measured dies, the improvement is between 21% and 64%. However, generally, the RNU is decreased down to half of the value obtained with the sweep or binary search method. It is possible to obtain higher uniformity by applying the algorithm more than once. The RNU value is decreased from 4.01% to 1.80% with two iterations.

3. NUC voltages can be estimated with 2 calibration points. However, to increase the efficiency in the proposed shutterless algorithm, 6 calibration points are used for the temperature range between 0 °C and 50 °C. The NUC voltages are updated with 1 °C step. This means that the required NUC voltage matrices (480x640) number is lowered from 51 to 6 with the estimation and the required array size is decreased by about 88%.
4. RNU values are kept below 1% after estimated 2-point correction parameters are applied. The highest RNU value obtained from the three samples is 1.01% at 45 °C and the lowest value is 0.34%.
5. PSNR values with the algorithm are higher than 40 dB for *Sample 7* and 50 dB for *Sample 8* in the entire temperature range (between 0 °C and 50 °C).
6. The temperature drift algorithm provides good stability at the pixel outputs in the 1 °C interval. The highest error in the mean output from the three samples is 557 ADU and this means that the maximum shift at the output is around 6%. Moreover, the RNU values are almost protected in the temperature interval. The highest change in the RNU is observed for *Sample 6* at 40 °C which is from 0.41% to 0.77%. However, generally, the change in the RNU is around 0.1%.
7. Calibration should be at least 12 temperature points over the entire temperature range to calculate the required parameters for the shutterless algorithm. If the parameters are calibrated for each temperature, 51 calibrations are needed. This provides to decreases the time for the entire calibration significantly.
8. The shutterless algorithm requires 2 matrices for NUC voltages, 6 matrices for gain coefficients, 6 matrices for offset coefficients, and 2 matrices for temperature drift coefficients. Totally, 16 matrices (480x640x16) are needed for the shutterless algorithm. However, 51 arrays for each gain and offset parameters are necessary for the standard method. This shows required array size is decreased by about 84% whereas temperature drift compensation is not considered in the standard case.

Whereas the results obtained with the shutterless algorithm are promising, it is possible to improve the performance. For this purpose, future works that can be done are listed below:

1. 2-point calibration can be improved by using the 3-point calibration since the response characteristics of the pixels is nonlinear. Obtained error with linear modeling of the response will decrease if the model is fitted into the second-order polynomial function. Each coefficient in the polynomial function should be modeled for temperature carefully. Moreover, three points that will be used in the calculation of the coefficients should be found precisely to provide the lowest error with the second-order function in the scene dynamic range. This can improve the quality of the image especially in the scenes where the differences between object temperatures are high.
2. The infrared illumination for the package of the microbolometer changes with temperature and this can increase the nonuniformity a little bit. It is not expected high temperature difference between the microbolometer and the package. However, if the ambient temperature changes suddenly, the difference can become high until their temperatures are settled. For these situations, the effect of the package temperature can be included in the shutterless algorithm to protect the RNU value. For real-time operations, the temperature of the package should be read via a temperature sensor on the package and the value should be considered for estimation of offset coefficients. Moreover, although the housing of the microbolometer camera is generally produced with specific material to decrease effect of the housing infrared illumination, it can be modeled to decrease the error more. Several temperature sensors should be placed into the microbolometer camera core even microbolometer lens and effect of the illumination for these components should be modeled. For this reason, an experiment setup should be prepared which enables to sweep temperature of these components discretely. This mean that the setup is complex, however, it will improve the uniformity and efficient especially in radiometric cameras.

3. Scene based algorithms such as denoising filter can be added into the shutterless algorithm to improve the uniformity and decrease the difference between RNU values at low and high temperatures. In addition to this, there are some studies are performed to remove effect of column based nonuniformity, called stripe nonuniformity [53]. In these studies, offset difference between output channels of the microbolometer due to mismatch in the output channels is analyzed. Firstly, edge detection methods are applied and non-edge area is found. After this, some statistical methods are applied to compensate the column based nonuniformity. In the proposed system, the nonuniformity is between rows due to error in NUC voltage estimation and inside row interactions; however, this can be adapted into proposed shutterless algorithm with some modifications in order to decrease row based nonuniformities in the images.

REFERENCES

- [1] A. M. Jensen, M. McKee and Y. Chen, "Procedures for processing thermal images using low-cost microbolometer cameras for small unmanned aerial systems," 2014 IEEE Geoscience and Remote Sensing Symposium, Quebec City, QC, 2014, pp. 2629-2632, doi: 10.1109/IGARSS.2014.6947013.
- [2] R. Vadivambal and D.S. Jayas, "Applications of Thermal Imaging in Agriculture and Food Industry—A Review." *Food Bioprocess Technol*, 2011, vol. 4, pp. 186–199, <https://doi.org/10.1007/s11947-010-0333-5>
- [3] A Rogalski, P Martyniuk, and M Kopytko, "Challenges of small-pixel infrared detectors: a review," 2016, *Rep. Prog. Phys.*, vol. 79, 046501, doi:10.1088/0034-4885/79/4/046501
- [4] A. Voshell, N. Dhar, and M. M. Rana, "Materials for microbolometers: vanadium oxide or silicon derivatives," Proc. SPIE 10209, Image Sensing Technologies: Materials, Devices, Systems, and Applications IV, 102090M (28 April 2017); <https://doi.org/10.1117/12.2263999>
- [5] J. Su, W. Yeh, W. Chang, B. Wu, J. Lu, J. Wang, Y. Fang, and P. Chen, "Temperature coefficient of resistance related to amorphous silicon/metal contact design of microbolometers," 2016 3rd International Conference on Devices, Circuits and Systems (ICDCS), Coimbatore, 2016, pp. 63-67, doi: 10.1109/ICDCSyst.2016.7570626.
- [6] A. Abdullah, A. Koppula, O. Alkorjia, C. Warder, T. Liu, E. Kinzel, and M. Almasri, "Micromachined Uncooled SixGeyO_{1-x-y} Microbolometer Integrated Metasurface for Uncooled Infrared Detection," 2019 20th International Conference on Solid-State Sensors, Actuators and Microsystems & Eurosensors XXXIII (TRANSDUCERS & EUROSENSORS XXXIII), Berlin, Germany, 2019, pp. 641-644, doi: 10.1109/TRANSDUCERS.2019.8808347.
- [7] M. Rafat M., Mohamed H. El-Mahlawy, A.H. Zaki, and M.S. Hamid, "Low-Power Low-Noise CTIA Readout Integrated Circuit Design for Thermal Imaging Applications," *Communications on Applied Electronics*, vol. 2, no. 8 September 2015.
- [8] S. Eminoglu, M.A. Gulden, N. Bayhan, O.S. Incedere, and M. Isikhan "A 640×480-17μm ROIC for uncooled microbolometer FPAs," Proc. SPIE 9451, Infrared Technology and Applications XLI, 94510Z (4 June 2015); <https://doi.org/10.1117/12.2179538>

- [9] J. Lv, H. Zhong, Y. Zhou, B. Liao, J. Wang, and Y. Jiang, "Model-Based Low-Noise Readout Integrated Circuit Design for Uncooled Microbolometers," in *IEEE Sensors Journal*, vol. 13, no. 4, pp. 1207-1215, April 2013, doi: 10.1109/JSEN.2012.2230621.
- [10] S. Liu, Y. Zhang, X. Meng, W. Lu, and Z. Chen, "A design of readout circuit for 384×288 uncooled microbolometer infrared focal plane array," *2012 IEEE 11th International Conference on Solid-State and Integrated Circuit Technology*, Xi'an, 2012, pp. 1-3, doi: 10.1109/ICSICT.2012.6467776.
- [11] S. Eminoglu and T. Akin, "MT3250BA: a 320×256-50 μ m Snapshot Microbolometer ROIC for high-resistance Detector Arrays," Proc. SPIE 8704, Infrared Technology and Applications XXXIX, 87042Y (18 June 2013); <https://doi.org/10.1117/12.2019525>
- [12] M. Tepegoz, "A Monolithic Readout Circuit for Large Format Uncooled Infrared Detector Focal Plane Arrays," Dissertation for the Degree of Doctor of Philosophy, Middle East Technical University, 2009.
- [13] D. J. de Waal and J. Schoeman, "An instrumentation amplifier based readout circuit for a dual element microbolometer infrared detector," Proc. SPIE 9257, Sensors, MEMS and Electro-Optical Systems, 92570L (23 June 2014); <https://doi.org/10.1117/12.2066301>
- [14] C. C. Li, C. Han, and G. D. Skidmore, "Overview of DRS uncooled VOx infrared detector development," Opt. Eng. 50(6) 061017 (1 June 2011) <https://doi.org/10.1117/1.3593155>
- [15] J. Lv, H. Zhong, Y. Zhou, B. Liao, J. Wang, and Y. Jiang, "Model-Based Low-Noise Readout Integrated Circuit Design for Uncooled Microbolometers," in *IEEE Sensors Journal*, vol. 13, no. 4, pp. 1207-1215, April 2013, doi: 10.1109/JSEN.2012.2230621.
- [16] B. Dupont, A. Dupret, E. Belhaire, and P. Villard, "FPN Sources in Bolometric Infrared Detectors," in *IEEE Sensors Journal*, vol. 9, no. 8, pp. 944-952, Aug. 2009, doi: 10.1109/JSEN.2009.2024041.
- [17] B. Hu, P. Li, A. Ruan, and D. Lin, "Design and verification of 160 × 120 bolometer ROIC," *2011 International Conference on Computational Problem-Solving (ICCP)*, Chengdu, 2011, pp. 275-278, doi: 10.1109/ICCP.2011.6092228.
- [18] S. Liu, Y. Zhang, X. Meng, W. Lu, and Z. Chen, "A design of readout circuit for 384×288 uncooled microbolometer infrared focal plane array," *2012 IEEE 11th International Conference on Solid-State and Integrated Circuit Technology*, Xi'an, 2012, pp. 1-3, doi: 10.1109/ICSICT.2012.6467776.

- [19] D. Svärd, C. Jansson, and A. Alvandpour, "A readout IC for an uncooled microbolometer infrared FPA with on-chip self-heating compensation in $0.35\text{ }\mu\text{m}$ CMOS." *Analog Integr Circ Sig Process* **77**, 29–44 (2013). <https://doi.org/10.1007/s10470-013-0116-9>
- [20] M. Tepegoz, A. Kucukkomurler, F. Tankut, S. Eminoglu, and T. Akin, "A miniature low-cost LWIR camera with a 160x120 microbolometer FPA," Proc. SPIE 9070, Infrared Technology and Applications XL, 90701O (24 June 2014); <https://doi.org/10.1117/12.2057508>.
- [21] M. Perenzoni, D. Mosconi, and D. Stoppa, "A 160×120 -pixel uncooled IR-FPA readout integrated circuit with on-chip non-uniformity compensation," *2010 Proceedings of ESSCIRC*, Seville, 2010, pp. 122-125, doi: 10.1109/ESSCIRC.2010.5619821.
- [22] I. W. Seo, E. S. Jung, and M. Y. Sung, "An Analog Front-End IC Design for 320 x 240 Microbolometer Array Applications," in *IEEE Transactions on Circuits and Systems II: Express Briefs*, vol. 62, no. 11, pp. 1048-1052, Nov. 2015, doi: 10.1109/TCSII.2015.2455391.
- [23] F. Tankut, M. H. Cologlu, H. Askar, H. Ozturk, H. K. Dumanli, F. Oruc, B. Tilkioglu, B. Ugur, O. S. Akar, M. Tepegoz, and T. Akin, "An 80x80 microbolometer type thermal imaging sensor using the LWIR-band CMOS infrared (CIR) technology," Proc. SPIE 10177, Infrared Technology and Applications XLIII, 101771X (2017); <https://doi.org/10.1117/12.2275161>
- [24] M. A. Gulden, "A Low-Cost Uncooled Infrared Imaging Sensor using MEMS and a Modified Standard CMOS Process," Dissertation for the Degree of Master of Science, Middle East Technical University, 2009.
- [25] A. Shafique, O. Ceylan, M. Yazici, M. Kaynak, and Y. Gurbuz, "A low-power CMOS readout IC with on-chip column-parallel SAR ADCs for microbolometer applications," Proc. SPIE 10624, Infrared Technology and Applications XLIV, 1062422 (2018); <https://doi.org/10.1117/12.2304994>
- [26] J. Lv, H. Zhong, Y. Zhou, B. Liao, J. Wang, and Y. Jiang, "Model-Based Low-Noise Readout Integrated Circuit Design for Uncooled Microbolometers," in *IEEE Sensors Journal*, vol. 13, no. 4, pp. 1207-1215, April 2013, doi: 10.1109/JSEN.2012.2230621.
- [27] D. Benirschke and S. Howard, "Characterization of a low-cost, commercially available, vanadium oxide microbolometer array for spectroscopic imaging," *Opt. Eng.* **56**(4) 040502 (2017) <https://doi.org/10.1117/1.OE.56.4.040502>
- [28] S. Abbasi, A. Shafique, O. Ceylan, and Y. Gurbuz, "A Digital Readout IC for Microbolometer Imagers Offering Low Power and Improved Self-Heating

Compensation," in *IEEE Sensors Journal*, vol. 20, no. 2, pp. 909-917, 15 Jan.15, 2020, doi: 10.1109/JSEN.2019.2944236.

- [29] M. Kohin and N. R. Butler, "Performance limits of uncooled VOx microbolometer focal plane arrays," Proc. SPIE 5406, Infrared Technology and Applications XXX, (2004); <https://doi.org/10.1117/12.542482>
- [30] M. Tepegoz, F. Civitci, and T. Akin, "An optimum reference detector design for uncooled microbolometer FPAs," Proc. SPIE 6940, Infrared Technology and Applications XXXIV, 694028 (2008); <https://doi.org/10.1117/12.786611>
- [31] Sui Xiu-Bao, Chen Qian, Gu Guo-Hua, and Liu Ning, "Research on the response model of microbolometer," *Chin. Phys. B*, vol. 19, no. 10, 2010.
- [32] M. Tepegoz, A. Oguz, A. Toprak, S. U. Senveli, E. Canga, M. Y. Tanrikulu, and T. Akin, "An uncooled microbolometer focal plane array using heating based resistance nonuniformity compensation," Proc. SPIE 8353, Infrared Technology and Applications XXXVIII, 83531E (2012); <https://doi.org/10.1117/12.964525>
- [33] X. Chen and K. Wu, "A New Bias Equalization for Microbolometer Array," *2010 Symposium on Photonics and Optoelectronics*, Chengdu, 2010, pp. 1-4, doi: 10.1109/SOPO.2010.5504031.
- [34] W. J. Parrish and J. T. Woolaway II, "Improvements in uncooled systems using bias equalization," Proc. SPIE 3698, Infrared Technology and Applications XXV, (1999); <https://doi.org/10.1117/12.354575>
- [35] M. Perenzoni, D. Mosconi, and D. Stoppa, "A 160×120 -pixel uncooled IR-FPA readout integrated circuit with on-chip non-uniformity compensation," *2010 Proceedings of ESSCIRC*, Seville, 2010, pp. 122-125, doi: 10.1109/ESSCIRC.2010.5619821.
- [36] M. Tepegoz, T. Akin, and M. H. Cologlu, "On-Chip Bias Calibration for Microbolometer Detectors and Readout Integrated Circuits". United States Patent US 2020/0120292 A1, 16 April 2020.
- [37] W. J. Parrish, "BOLOMETER ARRAY COMPENSATION". United States Patent US 7,709,793 B2, 4 May 2010.
- [38] D. L. Perry and E. L. Dereniak, "Linear theory of nonuniformity correction in infrared staring sensors," *Opt. Eng.* 32(8) (1993) <https://doi.org/10.1117/12.145601>
- [39] M. Krupiński, J. Barela, K. Firmanty, and M. Kastek, "Test stand for non-uniformity correction of microbolometer focal plane arrays used in thermal

cameras," Proc. SPIE 8896, Electro-Optical and Infrared Systems: Technology and Applications X, 889611 (2013); <https://doi.org/10.1117/12.2028633>

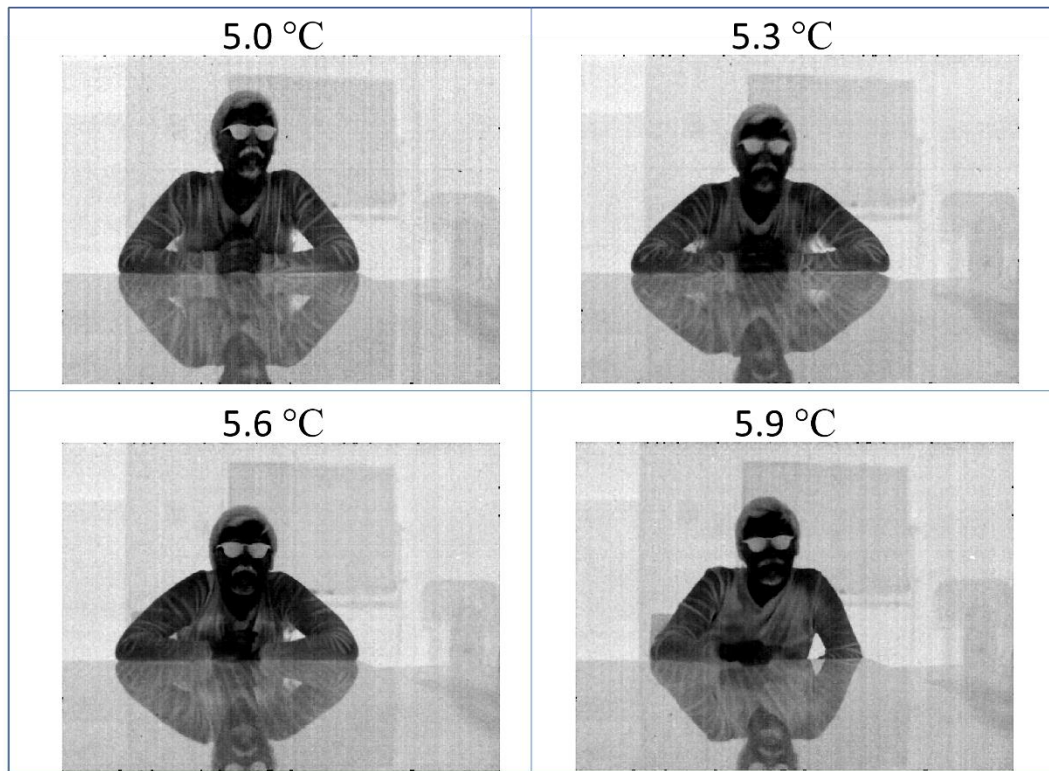
- [40] T. Orżanowski, and H. Madura, "Test and evaluation of reference-based nonuniformity correction methods for microbolometer infrared detectors", *Opto-Electronics Review* 18, 1 (2010): 91-94, doi: <https://doi.org/10.2478/s11772-009-0024-9>
- [41] A.S.H.Ahmed, M.M.Aboudina, and S.E.D.Habib, "Offset calibration technique for capacitive transimpedance amplifier used in uncooled infrared detection," *MicroelectronicsJournal*, vol 53, pp. 56-64, 2016. doi: <https://doi.org/10.1016/j.mejo.2016.03.012>.
- [42] S. Park, T. Cho, M. Kim, H. Park, and K. Lee, "A shutter-less micro-bolometer thermal imaging system using multiple digital correlated double sampling for mobile applications," *2017 Symposium on VLSI Circuits*, Kyoto, 2017, pp. C154-C155, doi: 10.23919/VLSIC.2017.8008577.
- [43] T. Orżanowski, "Nonuniformity correction algorithm with efficient pixel offset estimation for infrared focal plane arrays," *SpringerPlus* 5, 1831 (2016). <https://doi.org/10.1186/s40064-016-3534-1>
- [44] R.Strakowski and B. Wiecek, "Temperature drift compensation in metrological bolometer camera using multi sensor approach," 13th International Conference on QIRT 2016, Issue 2017-2, 2016
- [45] R. Olbrycht and B. Więcek (2015) New approach to thermal drift correction in microbolometer thermal cameras, Quantitative InfraRed Thermography Journal, 12:2, 184-195, DOI: [10.1080/17686733.2015.1055675](https://doi.org/10.1080/17686733.2015.1055675)
- [46] A. Voshell, N. Dhar, and M.M. Rana, "Materials for microbolometers: vanadium oxide or silicon derivatives," Proc. SPIE 10209, Image Sensing Technologies: Materials, Devices, Systems, and Applications IV, 102090M (2017); <https://doi.org/10.1117/12.2263999>
- [47] J. M. Tissot, S. Tinnes, A. Durand, C. Minassian, P. Robert, M. Vilain, and J. Yon, "High-performance uncooled amorphous silicon video graphics array and extended graphics array infrared focal plane arrays with 17-μm pixel pitch," Opt. Eng. 50(6) 061006 (2011) <https://doi.org/10.1117/1.3572155>
- [48] G. Bieszczad, T. Orżanowski, T. Sosnowski, and M. Kastek, "Method of detectors offset correction in thermovision camera with uncooled microbolometric focal plane array," Proc. SPIE 7481, Electro-Optical and Infrared Systems: Technology and Applications VI, 74810O (2009); <https://doi.org/10.1117/12.830678>

- [49] J. Das, D. de Gaspari, P. Cornet, P. Deroo, J. Vermeiren, and P. Merken, "Implementation and performance of shutterless uncooled micro-bolometer cameras," Proc. SPIE 9451, Infrared Technology and Applications XLI, 94511G (2015); <https://doi.org/10.1117/12.2177315>
- [50] A. Tempelhahn, H. Budzier, V. Krause, and G. Gerlach, "Shutter-less calibration of uncooled infrared cameras," J. Sens. Sens. Syst., 5, 9–16, <https://doi.org/10.5194/jsss-5-9-2016>, 2016.
- [51] C. Liu and X. Sui, "Improved calibration-based non-uniformity correction method for uncooled infrared camera," Proc. SPIE 10404, Infrared Sensors, Devices, and Applications VII, 104040X (2017); <https://doi.org/10.1117/12.2271410>
- [52] K. Liang, C. Yang, L. Peng, and B. Zhou, "Nonuniformity correction based on focal plane array temperature in uncooled long-wave infrared cameras without a shutter," Appl. Opt. 56, 884-889 (2017)
- [53] W. Qian, Q. Chen, G. Gu, and Z. Guan, "Correction method for stripe nonuniformity," Appl. Opt. 49, 1764-1773 (2010)
- [54] C. Zuo, Q. Chen, G. Gu, X. Sui, and J. Ren, "Improved interframe registration based nonuniformity correction for focal plane arrays," *Infrared Physics & Technology*, vol. 55, pp. 263-269, 2012. <https://doi.org/10.1016/j.infrared.2012.04.002>.
- [55] H. Yu, Z. Zhang, F. Chen, and C. Wang, "Non-local means-based nonuniformity correction for infrared focal-plane array detectors," Proc. SPIE 9301, International Symposium on Optoelectronic Technology and Application 2014: Image Processing and Pattern Recognition, 93013K (2014); <https://doi.org/10.1117/12.2074379>
- [56] A. Boutemedjet, C. Deng, and B. Zhao, "Robust Approach for Nonuniformity Correction in Infrared Focal Plane Array," *Sensors* 2016, 16, 1890.
- [57] Z. He, Y. Cao, Y. Dong, J. Yang, Y. Cao, and C. Tisse, "Single-image-based nonuniformity correction of uncooled long-wave infrared detectors: a deep-learning approach," Appl. Opt. 57, D155-D164 (2018)
- [58] Y. Shamay, E. Braunstain, R. Gazit, Y. Gridish, R. Iosevich, S. Linzer Horesh, Y. Lury, R. Meshorer, U. Mizrahi, E. Raz, M. Savchenko, N. Syrel, and S. Yuval, "Low SWaP 640×480/17μm Uncooled Detector and Video Core," in 2016 (International Symposium on Optronics in Defense and Security), (2016)

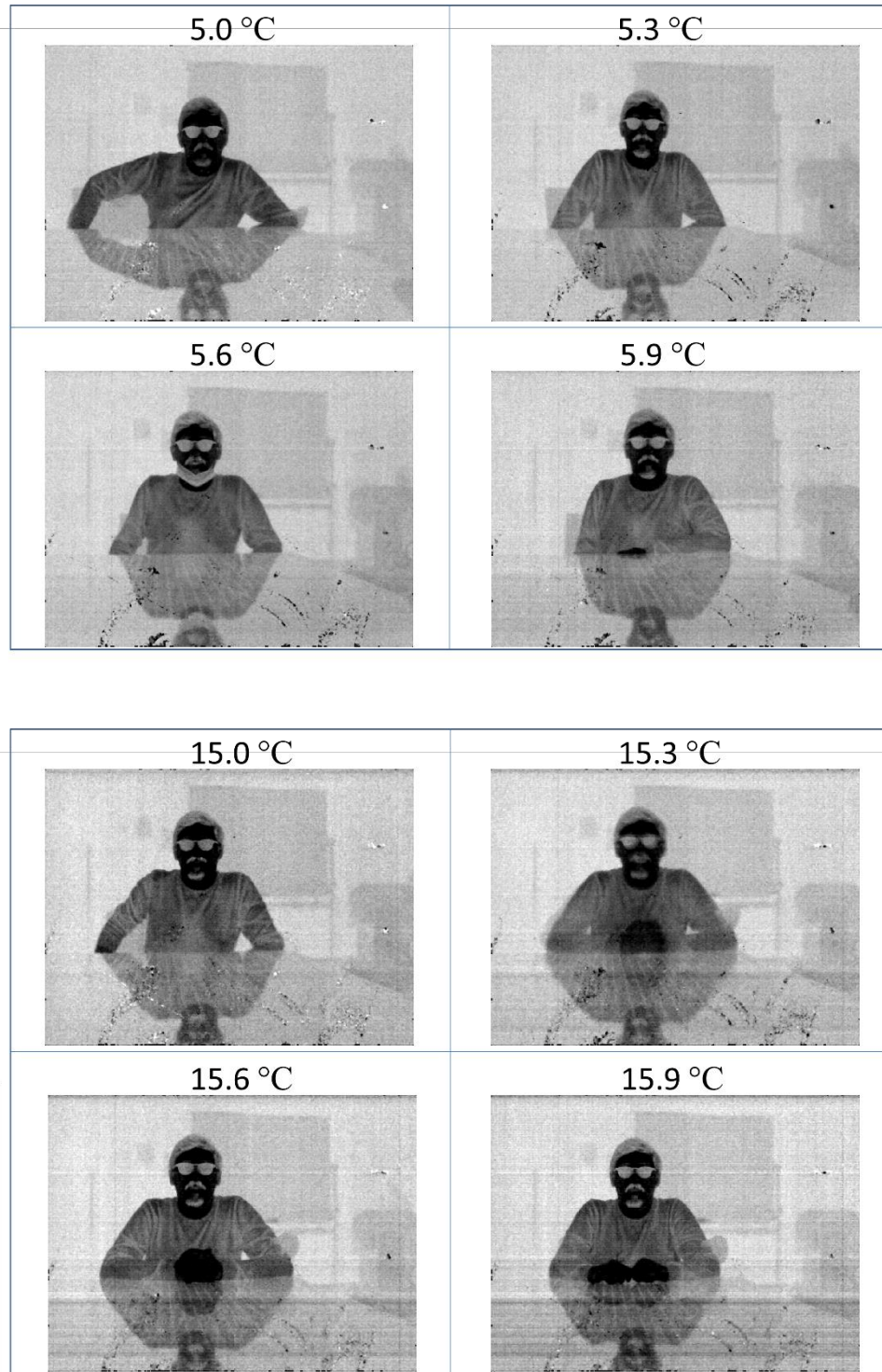
- [59] C. Liu , X. Sui, G. Gu, and Q. Chen, "Shutterless non-uniformity correction for the long-term stability of an uncooled long-wave infrared camera," *Meas. Sci. Technol.*, vol. 29, no. 2, 2018.
- [60] X. Cao, B. Zhu, S. Wang, Y. Yong, Y. Huo, and J. Huo, "Nonuniformity Correction Algorithm for TEC-less Uncooled Infrared Imaging System," *2019 IEEE 5th International Conference on Computer and Communications (ICCC)*, Chengdu, China, 2019, pp. 214-219, doi: 10.1109/ICCC47050.2019.9064432.
- [61] D. Jung, Y. Jung, T. Yoo, D. Yoon, B. Jung, T.T. Kim, and K. Baek, "A 12-bit Multi-Channel R-R DAC Using a Shared Resistor String Scheme for Area-Efficient Display Source Driver," in *IEEE Transactions on Circuits and Systems I: Regular Papers*, vol. 65, no. 11, pp. 3688-3697, Nov. 2018, doi: 10.1109/TCSI.2018.2854849.
- [62] L. Blanquart, J. Wallner, and M. Bhat, "Pausing Digital Readout of an Optical Sensor Array". United States of America Patent US 8,823,846 B2, 2 September 2014.

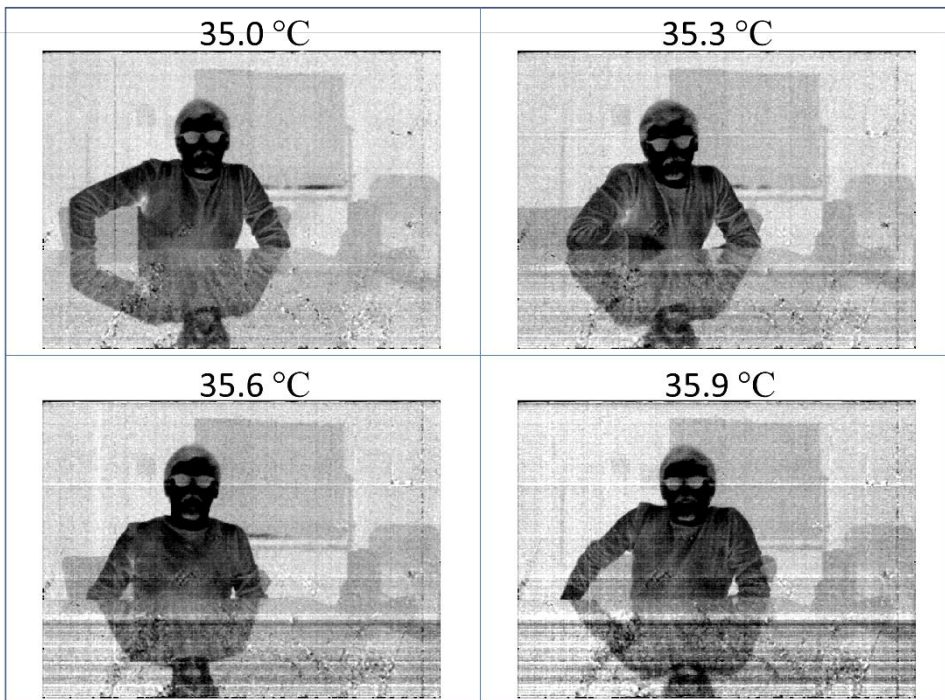
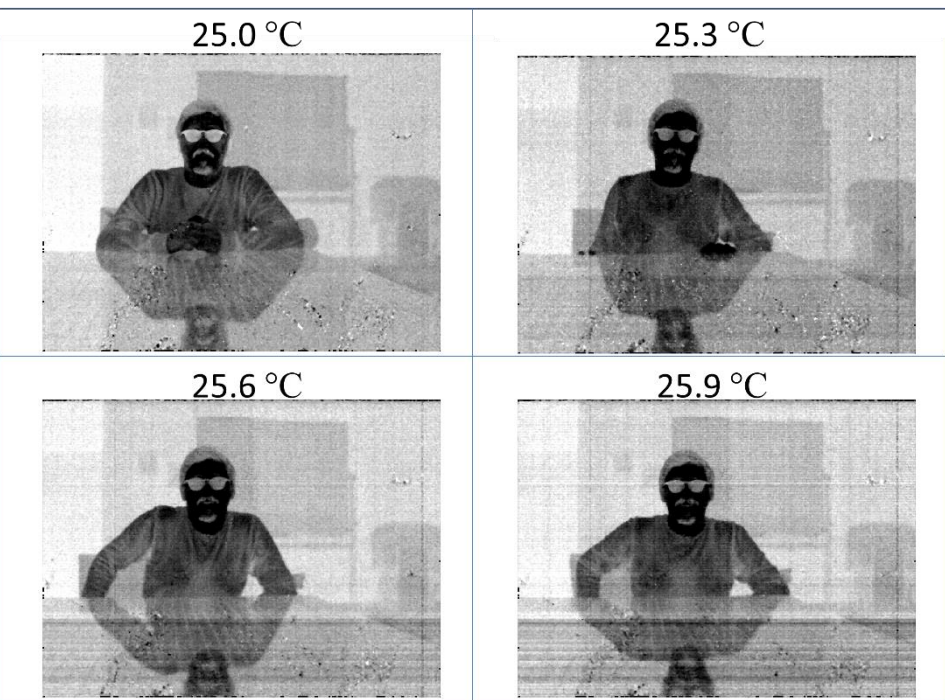
APPENDICES

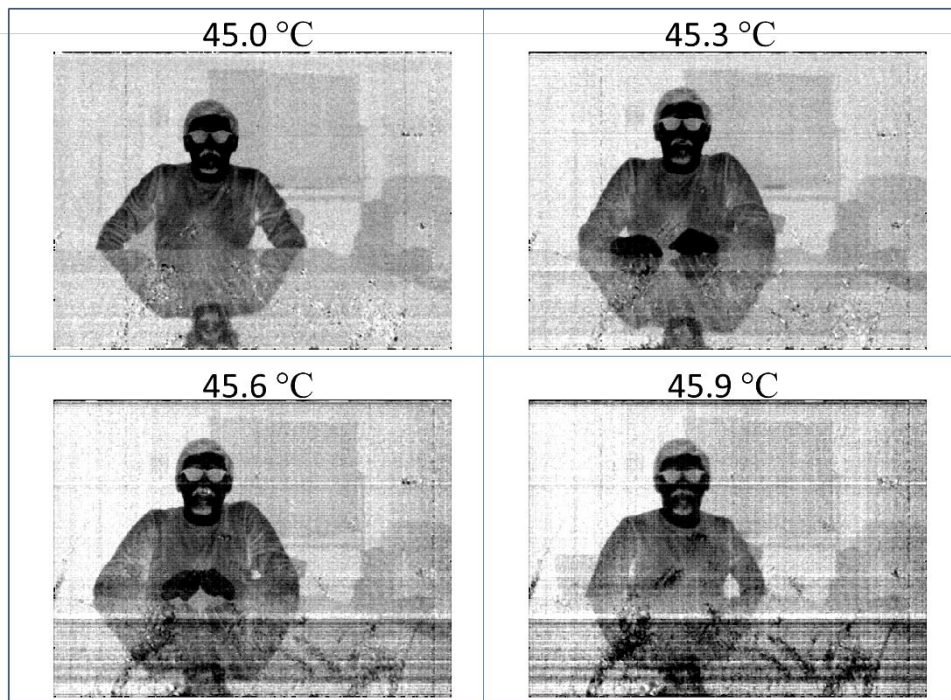
A. Thermal Images for Sample 6



B. Thermal Images for Sample 7







C. Thermal Images for Sample 8

